Understanding of the relationship between the mechanical state and the durability of PEM fuel cells

Marwa Ouerghemmi

THÈSE

Pour obtenir le grade de

DOCTEUR DE L'UNIVERSITÉ GRENOBLE ALPES

École doctorale : I-MEP2 - Ingénierie - Matériaux, Mécanique, Environnement, Energétique, Procédés, Production
Spécialité : 2MGE : Matériaux, Mécanique, Génie civil, Electrochimie
Unité de recherche : Laboratoire d'Electrochimie et de Physico-Chimie des Matériaux et des Interfaces.

Compréhension des relations entre l'état mécanique et la durabilité de piles à combustible de type PEM

Understanding of the relationship between the mechanical state and the durability of PEM fuel cells

Présentée par :

Marwa OUERGHEMMI

Direction de thèse :

Monsieur Patrice MELE — Directeur de thèse

Professeur, Université de Savoie Mont Blanc

Monsieur Christophe CARRAL — Co-encadrant de thèse

Maître de conférences, Université Savoie Mont Blanc

Rapporteurs :

Monsieur Olivier LOTTIN

Professeur, Université de Lorraine

Monsieur Yann MEYER

Professeur, Université Savoie Mont Blanc

Thèse soutenue publiquement le , devant le jury composé de :

Madame Assma El KADDOURI

Maître de conférences, Université de Lorraine

Monsieur Jean François BLACHOT

Ingénieur Chercheur, CEA Liten

Monsieur Marian CHATENET

Professeur, Université Grenoble Alpes

Table des matières

Glossary

BPP	BiPolarPlate
CCB	Catalyst Coated Backing
CCM	Catalyst Coated Membrane
CD	Cross-machine Direction
CL	Catalyst Layer
EP	End Plates
GC	Gas channel
GDL	Gas Diffusion Layer
GDM	Gas Diffusion Media
iNFS	Ionomer Nanofiber Scaffoldings
MD	Machine Direction
MEA	Membrane Electrode Assembly
MPL	Microporous Layer
PAN	polyacrylonitrile
PEM	Proton Exchange Membrane
PEMFC	Proton Exchange Membrane Fuel Cell
PFSA	Perfluorosulfonic Acid
PTFE	Polytetrafluoroethylene
SEM	Scanning Electron Microscope
TFE	tetrafluoroethylene
XCT	X-ray computed tomography

Symbols

Δth	Thickness variation
A	Cross sectional area
E	Young's modulus
F	Force
FN	Normal force
FT	Tangential force
G	Shear modulus
GPa	Gigapascal
MPa	Megapascal
P	Pressure
Ra	Roughness
RH	Relative humidity
T	Temperature
Tg	Glass transition temperature
th	Thickness
α	Thermal expansion coefficient
γ	Angular strain
ε	Elongation strain
ηact	Activation loss
ηconc	Gas concentration loss
ηohmic	Ohmic loss
μ	Friction coefficient
ν	Poisson's ratio
σ	Stress
τ	Shear stress
δ	Kronecker symbol

General introduction

The climate issue in the current context is mainly focused on the global warming due to the emission of gases by human activities. Whether it is produced or consumed, energy is largely responsible for the ecosystem's crisis.

On this basis, numerous researches are engaged to reduce the environmental impact of the production, distribution and consumption of energy, aiming towards green energy transition. The global efforts in this energy transition have recently gained a substantial amount of support from the communities of science, engineering, academia, industry, and governments in all aspects.

Studies were focused on the development of new strategies to affect positive global change by finding new resources of renewable energy to reduce the massive consumption of fossil fuels responsible for greenhouse gas emissions. The ultimate goal is to use new so-called clean energies.

One of the most promising devices, are proton exchange membrane fuel cells PEMFC. They have emerged as alternative solutions for clean energy production, providing long-term solutions to the improvement of energy efficiency, energy sustainability, and energy security and the reduction of greenhouse gases and urban pollution.

Significant environmental benefits are expected for fuel cells, particularly for energy conversion for transportation and electric power generation.

They are expected to play a significant role in increasing fuel efficiency, and decreasing dependency on traditional fossil fuels.

PEMFC is a lower temperature fuel cell (< 100°C) with a polymer electrolyte membrane. This lower temperature fuel cell is well suited for transportation, portable, and micro fuel cell applications because of the importance of fast start-up and dynamic operation. It works with hydrogen stored under pressure or in solid form, and ambient air oxygen. Apart from the asset of using non-polluting gases, PEMFC does not emit any in return. The particularity of this device consists also in its durable energy storage.

Despite the currently promising achievements and the plausible prospects of PEMFCs, there are many remaining challenges that need to be overcome before PEMFCs can successfully and economically substitute for the various traditional energy systems. One of the major drawbacks is its short life span, as well as the high cost. Therefore, many studies are oriented towards reducing its manufacturing cost, extending its life span and ameliorating its performance during the operation cycles. The majority of the conducted work revolves around the mitigation of the degradation mechanisms of the core of the fuel cell also called membrane electrode assembly MEA. The MEA is composed of a

membrane surrounded by active layers and two gas diffusion layers. The degradation of this MEA leads to the loss of the cell's performance and even to its shutdown.

The understanding of the degradation that occurs during aging has been investigated, however, most of the studies did not focus on the link between these degradation mechanisms and the mechanical state of the MEA.

In this context, the subject of this study is to provide a better understanding of the mechanical state of the MEA and more particularly, to reveal its impact on the performance and durability of the entire cell.

The followed approach is based on an experimental and numerical analyses to understand the global mechanical response of the MEA different components under the various mechanical stresses.

This manuscript is divided in 4 parts:

Chapter I presents the functioning principles of the principles of PEMFC and its different components as well as the different manufacturing processes of its core (MEA). It aims to also report the mechanical characteristics of each component, and their impact on the performance of the cell.

Chapter II presents the experimental approach developed to identify the mechanical properties of gas diffusion layers. The tests were performed in both planes (in-plane/out-of-plane) and according to the machine and transverse directions.

Chapter III is a continuity of the previous experimental work with an extension to the global MEA study. A new parameter is identified in this section in order to analyze the mechanical properties at interfaces between the MEA layers. A quantitative analysis is conducted via the friction coefficients and roughness measurements, followed by a qualitative morphological analysis.

Chapter IV is a summary of all of the previous experimental work. It presents a numerical analysis of the mechanical behavior of the membrane. The developed model offers the possibility to evaluate the stress and strain levels of the membrane under assembly load and hygrothermal operating condition. Materials properties and the properties of the interfaces on the mechanical response of the membrane, are also investigated.

Chapter I: General overview of the study

This first chapter of this study is intended to review the work in the literature to identify the PEMFC different components and its functioning principles. The aim here is to bring some understanding of their mechanical behavior under the various operating and assembly conditions. Eventually, the impact of the mechanical state on the performance of the cell is investigated.

This chapter is divided in three parts:

- The first part provides a detailed insight on the composition of the fuel cell as well as its operating principles. The role of every component is detailed, to better understand the functioning of the fuel cell.

- In the second part, a particular focus was attributed to the study of the different elements forming the MEA, core of this study. It also includes the different steps of the MEA fabrication process.

- The third part is dedicated to the mechanical phenomena characterizing the performance of the cell. First the mechanical behavior of the different MEA layers is described. Second the impact of the assembly and operating conditions on the mechanical state of each component is detailed.

This state of art highlights the importance of the mechanical state of the fuel cell on its performance during its operation, as well as its durability.

I. Overview on PEM fuel cells

Proton exchange membrane fuel cells (PEMFC) were discovered by Sir William Grove in 1839 based on the previous work of Christian Friedrich Shönbein [1]. He published a description of the working of the first fuel cell describing its operation on various reactants, including ethylene and carbon monoxide, as well as hydrogen [2]. He described the mechanisms of a singular cell, made up of hydrogen and oxygen in contact with two platinum electrodes and suggested that several of these could be combined in series to form a gas voltaic cell [3].

PEM technology served as part of NASA's Gemini project in the piloted space program of the united states in the 1960s [4].

The proton exchange membrane fuel cell (PEMFC) is a system that generates electrical power through the reverse reaction of water electrolysis [5]. The fundamental structure of a fuel cell consists of an electrolyte layer in contact with two electrodes, both coated witch catalyst layers to initiate the electrochemical reactions occurring at the anode and the cathode [6].

The operating principle of the PEMFC and the electrochemical reactions are shown on ***Figure 1***.

The equations describing the electrochemical reactions are the following:

Anode $$H_2 \rightarrow 2H^+ + 2e^- \quad (1)$$

Cathode $$2H^+ + 2e^- + \frac{1}{2}O_2 \rightarrow H_2O \quad (2)$$

Global $$H_2 + \frac{1}{2}O_2 \rightarrow H_2O + Heat \quad (3)$$

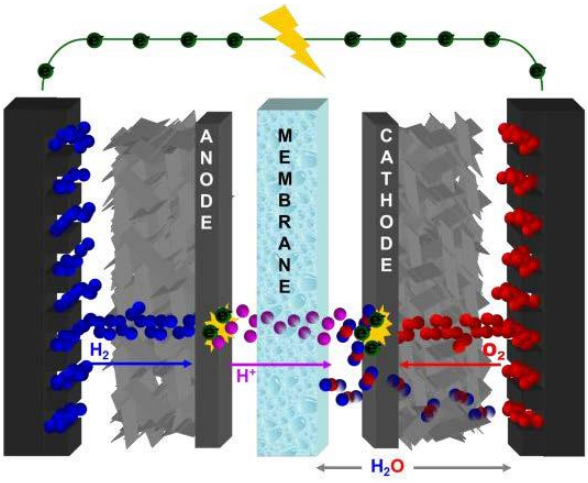

Figure 1: *Operating principle of the PEMFC fuel cell [7]*

A standard technique in fuel cell characterization is the polarization curve (***Figure 2***); it consists in measuring the variations of cell voltage as a function of the current density. It

is a diagnostic technique for the evaluation of fuel cell performance and for the operating parameters impact analysis. From a polarization curve it is possible to distinguish between kinetic, ohmic and mass transport losses [8].

The polarization curve is influenced by three types of loss:

• Activation energy of the electrochemical reactions at the electrodes, η_{act}.

• Electrical resistivity of the components and more particularly the protonic resistance of the membrane, η_{ohmic}.

• Reactant gases rate, η_{conc}.

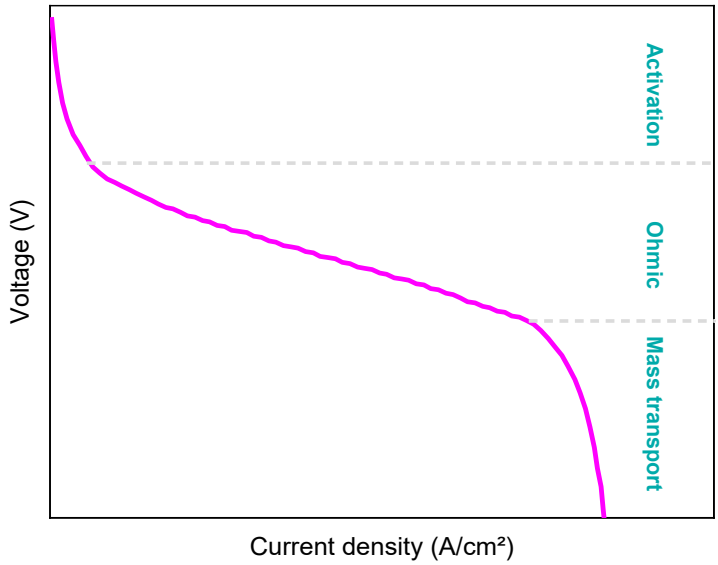

Figure 2: *Typical fuel cell polarization curve*

Fuel cells can be specified into different categories based on types of fuel used (hydrogen, carbon monoxide…), the electrolyte (liquid or solid) and the operating temperature range (going from 60°C to 210°C for low-temperature fuel cells and could reach over 650°C for high-temperature ones) [9–16]. PEMFCs are considered as a low-temperature fuel cell as its operating temperature is in the range of 60 to 120°C, using the hydrogen as a charge carrier and a solid polymer electrolyte, usually Perfluorosulfonic (PFSA) membrane.

Compared to other types of fuel cell, PEMFCs can provide higher power density for transportation systems and vehicular applications with relatively short start-up time and lower operation temperature and pressure, low weight and volume and high efficiency, [11,17–20].

At the end of 2020, more than 540 hydrogen refueling stations were in operation worldwide, an increase of more than 15% from 2019 [21]. Other application fields could include mobile and portable devices such as portable computers [22–25].

PEMFCs stack (***Figure 3***) are composed of several electrochemical cells. Each cell is an assembly of bipolar plates (BPP), surrounding the membrane electrode assembly (MEA),

which is the core of the fuel cell and place of all the electrochemical reactions. It is composed of two gas diffusion layers (GDL), a membrane and two active layers.

Redox reactions of the reactants (dihydrogen and oxygen) take place on the two electrodes; the reactants pass through the bipolar plates to the electrodes; the reactions of hydrogen produce electrons and protons which are then transported to the cathode through the membrane where they meet oxygen and produce water (***Figure 1***).

The continuous supply of reactants allows the continuous production of electric current.

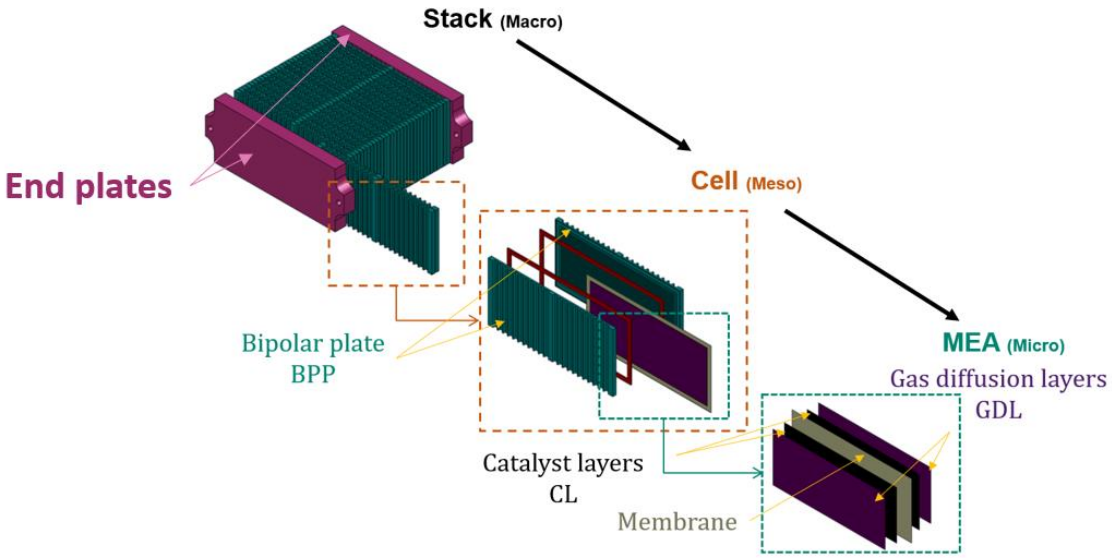

Figure 3: *PEMFC stack components (Adapted from [26]).*

Figure 3 presents the different components of a fuel cell stack. The entire stack is assembled by two end plates which principal role is to ensure sufficient and uniform pressure distribution between the different components of the fuel cell, therefore, they help reduce contact resistance and supply sufficient sealing forces for the different media flows. These effects may lead to increased stack pressure at the boundary of the bipolar plates. In addition, they have the important role of stabilizing the stack to resist external forces in real operating conditions.

The elementary electrochemical cells are composed of bipolar plates (BPPs), which are a key component of PEMFCs. Developing higher properties bipolar plates is one of the means of enhancing the mechanical durability of PEMFCs [27]. The principle roles of BPP is to ensure the uniform and efficient distribution of fuel gas and air, conduct electrical current from cell to cell, enable heat evacuation from the active area, and prevent leakage of gases and coolant which allows a seal provision between electrodes. In addition, they play an important role in supporting the mechanical loads imposed on the cell to ensure good stability and performance [28].

BPPs significantly contribute to the volume, weight and cost of PEM fuel cells; they actually account for almost 70% of the mass of the stack and 30% of the overall price of the cell stack [29].

Hence, there are vigorous efforts worldwide to find suitable materials and working on the geometry as it has an influence on the transfer of electrons and the distribution of the reactive gases on the electrodes, and therefore on the performance of the fuel cell [30–38].

Indeed, each cell of the stack receives a variable flow rate of hydrogen during the functioning cycle, which is, among others, controlled by the geometry of the bipolar plate relative to each cell. Poorly designed bipolar plates lead to variable gas distribution through the fuel cell, which leads to temperature gradients in the cell and, thus, localized hot spots in the electrolyte and unstable current density which can lead to poor water management and compromise stack performance [39].

BPPs materials include non-porous graphite, coated metallic sheets, polymer and carbon-based composites [40]. Graphite is the most used due to its ability to resist to corrosion and its high surface electrical conductivity in the PEM fuel cell environment. Metallic BPPs have also been used for their mechanical strength but they are more exposed to corrosion problems, which causes an increase of the electrical resistance and a decrease of its efficiency [41,42]. Those materials undergo different shaping processes in order to obtain optimal geometries for the operation of the PEMFCs, especially the flow field part of BPPs where the reactant gases and water are transported. Geometric parameters like channel length or flow direction must be considered during the design of bipolar plate as they have impact on functional properties such as mass transport, heat transfer or electrical conductivity [43].

II. Focus on the fuel cell core

The membrane electrode assembly is considered as the core and heart of a PEMFC, place of all the electrochemical reactions and energy generation. As described above, it is mainly composed of five layers: two gas diffusion layers on top of two electrodes surrounding the membrane. These different layers will be described below:

1. Gas diffusion media

The transport layer also called gas diffusion media (GDM) is a porous layer, which principle roles are [44]:

- Pathway for reactant transport: reactant gas access from BPP flow-field channels to catalyst layers.
- Water management: passage making for water removal from catalyst layer area to flow-field channels.
- Thermal conductivity: heat evacuation from the active layers to the BPP

- Electrical conductivity: electrons transport from electrochemical reaction sites to the BPP.
- Mechanical support to the whole MEA: mechanical support provision and protection for the catalyst layer and membrane during both assembly and operation.

Structure

The main structure of GDM can be divided in two parts: the fibrous substrate also known as gas diffusion layer substrate (GDL) and the micro porous layers (MPL). It should be noted that the entire layer might be loosely referred to as GDL since the MPL is a dependent part of the GDL and is not considered as a full-fledged layer in most of the studies.

The fibrous substrate can be identified as a carbon-carbon composite, in which carbon fibers, with 6–10 μm diameter [44], are randomly dispersed in 2D to form a sheet. The thickness of the fibrous substrate is generally within the range of 150–400 μm, and the morphology is strongly porous (70% to 80%), with a majority of pore sizes in the range of 10–30 μm [44–47]. A hydrophobic treatment is applied on GDLs to avoid water adsorption. In novel GDLs a MPL is added to the fiber substrate to enhance its transport properties; as its name indicates, this layer exhibits a smaller porosity size compared to the one of the substrate, within the range of 100 to 500 nm [44].

Different types of gas diffusion layers

Different types of GDLs exist according to the fiber substrates employed. There are two main categories of porous fiber substrate, i.e. carbon papers (non-woven) and carbon cloths (woven). Among the non-woven category, straight or curved carbon fibers can be used to form GDLs in roll, sheet or felt forms (***Figure 4***).

Carbon cloths and carbon papers have different fabrication methods and hence have different structures and properties. Therefore, they exhibit different performance in different operating conditions [48].

It was shown that at high current densities, carbon cloths are better candidates than carbon papers, whereas, at low current densities the performance of carbon cloths and papers presented similar performances [49–51].

Wang *et al* [52] performed experiments as well as a numerical study to establish the structure–performance relationships of carbon cloth and carbon paper;, they concluded that carbon cloth gives better performance in high humidity and carbon paper has better performance at low humidity.

In fact, the highly tortuous structure of the carbon paper leads to severe mass transport limitation under high-humidity operations which makes the carbon cloth a better choice. However, under the dry condition, the carbon paper is found to be superior as it retains product water in the MEA and improves the membrane hydration hence its proton conductivity

Stampino *et al*. [53] reported that for current densities lower than 800 mA.cm^{-2}, carbon paper exhibits better performance at different humidity levels for air (60%, 80% and 100%). However, water management issues were observed at higher current densities.

Kowal *et al*. [54] used neutron imaging and showed that carbon cloth had more balanced water distribution, unlike carbon paper which was proved to be more prone to flooding as more water is accumulated under the ribs.

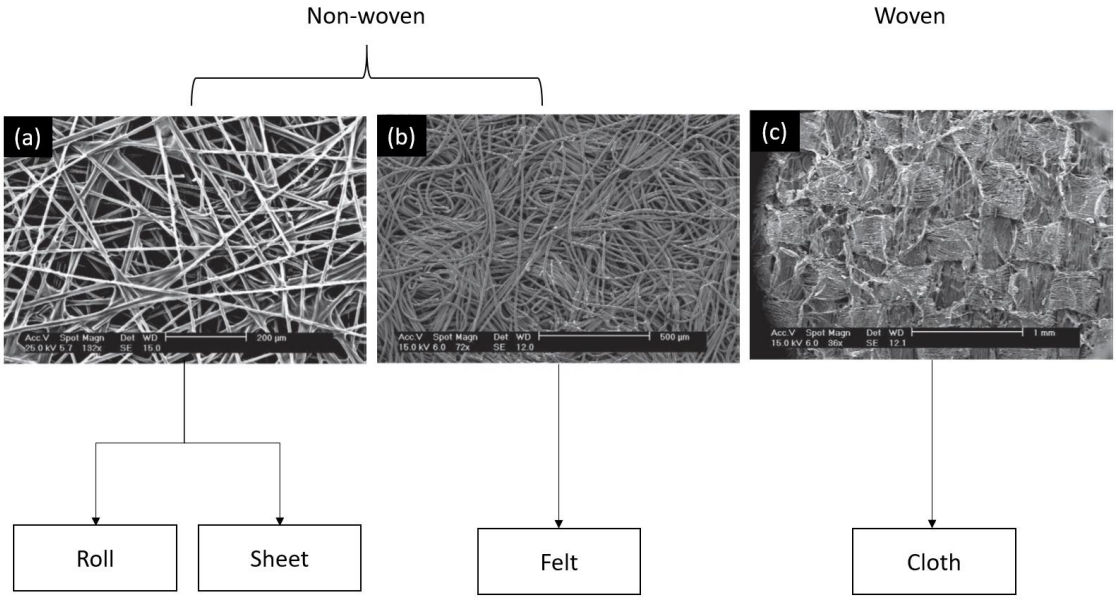

Figure 4: *GDL types classified into non-woven type(a) carbon paper (roll or sheet); (b) felt or spaghetti fibers and (c) woven type (carbon cloth) (Adapted from [47]).*

Fabrication principle of GDL

The first part consists in creating the substrate from carbon fibers, the most attractive choice for the raw material is the polyacrylonitrile (PAN) due to precursor cost, high carbon yield (50%) and final carbon-fiber properties.

During the manufacturing process, the fibers are impregnated with a thermoset resin used as a binder in the case of carbon papers and felts, but not for cloth type, where no binder is added.

Afterwards, heat treatments are applied to improve mechanical and electrical properties of carbon-fibers.

The carbon papers undergo, first, carbonization, and second, graphitization stages after the impregnation process. The carbonization step is carried out in the temperature range of 1200°C to 1350°C to obtain roll GDL (95% carbon), and an extra graphitization step above 2000°C is carried out for sheet type (99% carbon) [44].

For carbon cloths, first a carbonaceous fiber production step is applied (made from meso-phase pitch spun by melt spinning, centrifugal spinning, blow spinning, etc.); second, a fiber oxidation step and third, a cloth formation step by weaving or knitting. Note that the

carbonization happens after the carbon yarns woven. as opposed to the carbon papers [44].

For example, the manufacturing process for a Sigracet GDL paper with MPL is described in ***Figure 5***.

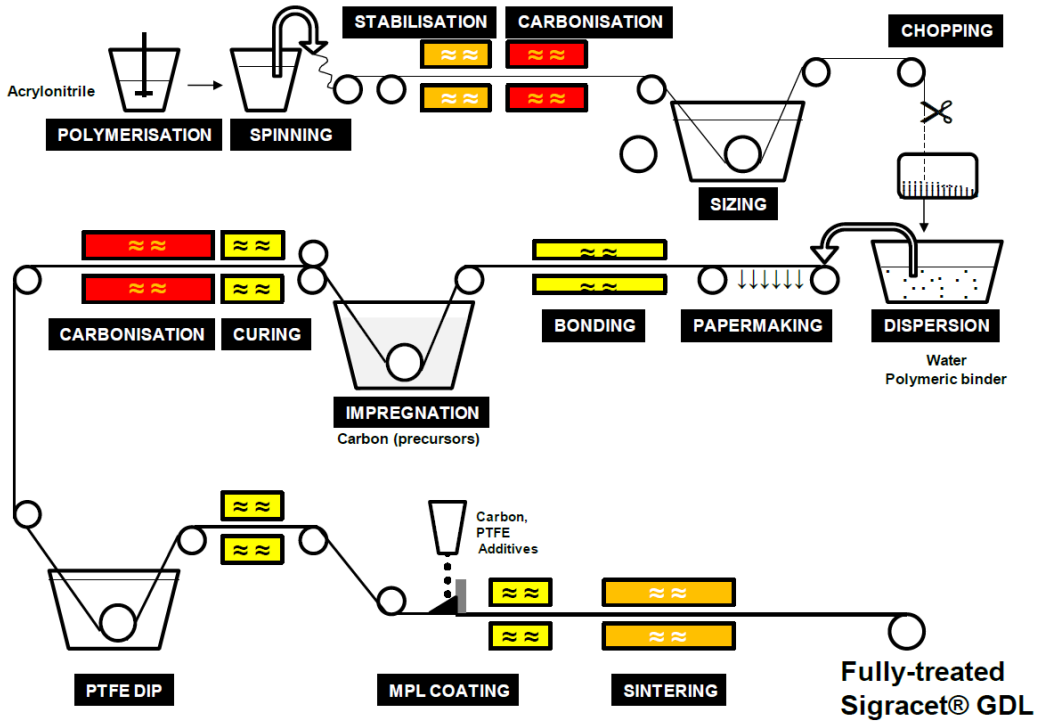

Figure 5: *Schematic of the fabrication process of Sigracet ®gas diffusion layer (GDL+MPL) (Adapted from [55]).*

Hydrophobic treatment

Water management is one of the main functions of GDL especially in the cathode side. It is crucial to ensure performance of fuel cells.

As explained before, the product water must be removed from the fuel cell, otherwise there is a risk of water accumulation which could prevent the reactants circulation; this phenomenon is often referred to as flooding. However, if the amount of water in the membrane is too low, the membrane conductivity decreases, as will the fuel cell performance [56].

Diffusion media are generally made hydrophobic in order to avoid flooding in their bulk. Moreover, the interfaces with adjacent layers are also tailored with coatings or layers to ensure efficient liquid transport into and out of the diffusion layer. The treatment is usually made with Polytetrafluoroethylene (PTFE) [44,57,58].

A wide range of PTFE contents have been used in the literature, from 5 to 30 wt.%. Most of the studies investigated the GDL optimum properties in terms of PTFE rate in MPL. The best performances were obtained for a rate around 20 wt.% PTFE [59,60].

The PTFE can be applied to the fibrous substrate in several ways. Most commonly, it could be carried out through a sequential process of impregnation; the fibers substrate is dipped into an aqueous PTFE suspension before applying the microporous layer as depicted in ***Figure 6***. Excess suspension is allowed to drip off, the remaining solvent is removed by oven drying and finally the GDL is heated above 350°C to sinter the PTFE particles and fix the PTFE to the surface. In dipping, PTFE loading is controlled by adjusting the concentration of the suspension [44]. Lifetime and properties could be improved by a multistage PTFE treatment [61].

Other than bulk treatment, PTFE can also be applied by spraying or brushing when if only one side of the fibrous substrate needs to be coated [44].

In the MPL, the PTFE is directly included in the material before it is coated on GDL.

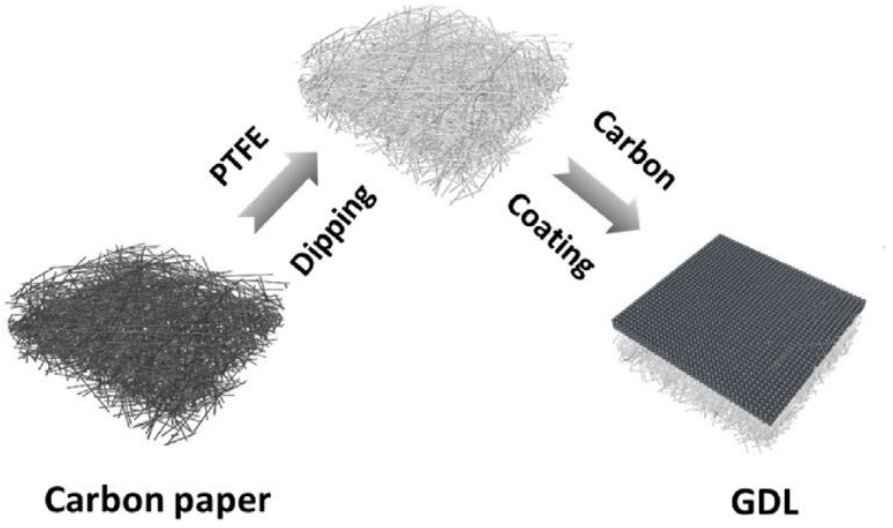

Figure 6*: Hydrophobic treatment and MPL application for carbon paper diffusion media (Adapted from [62])*

Microporous layer

A MPL is usually added to the main substrate in order to improve the electrical conductivity and water management [63] (***Figure*** *7*). It serves for porosity transition, since it is fabricated with carbon powder aggregation [64] and has, thus, smaller pores than the substrate's part, in the range of 100 to 500 nm as cited above [44].

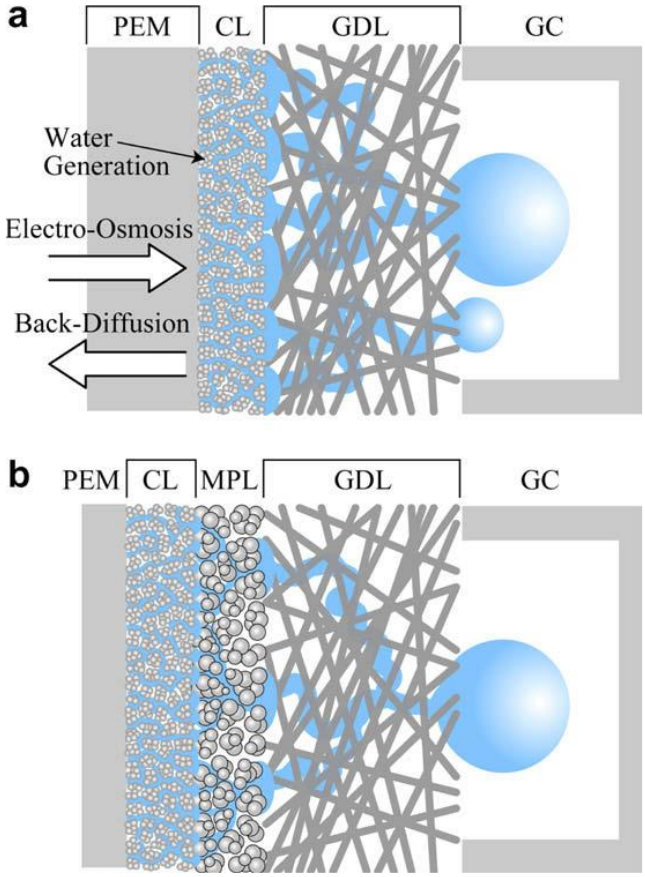

Figure 7*: Structure of cathodes (a) without and (b) with MPL [65].*

By providing effective mass transfer of liquid water in catalyst layer to GDL, the MPL helps improve water management of the entire diffusion media system. Besides, coating carbon slurry onto the carbon paper can make its surface smooth as portrayed in ***Figure 8***, in a way to make buffer layer which improves the electrical contact between CL and GDL. As a result, potential contact loss between catalyst and membrane and migration of catalyst into GDL can be prevented [44,66]. In ***Figure 8*** , a micrograph of an ELAT® microporous layer is coated on a carbon cloth substrate. No underlying fibers are visible, and, with the exception of several cracks in the layer, the coating appears smooth on the micron scale.

MPL consists of a suspension of carbon powder, PTFE and ethanol with subsequent drying [62]. The microstructure and surface hydrophobicity of the MPL could be designed by modulating the amounts of carbon powder and PTFE in the coating suspensions [62].

Several techniques could be followed to apply MPL; the doctor blade method is common. Others including screen printing, spraying, or rod coating can be also used. The carbon paste parameters, such as the solvent choice and solid concentration, must be tailored to provide a coating of desired thickness and substrate penetration with the given application technique [44].

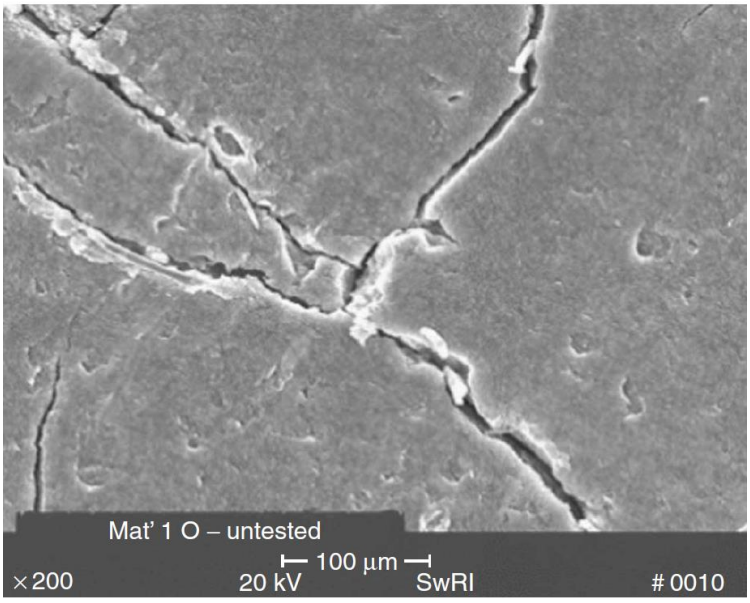

Figure 8: *SEM (top view) of microporous layer produced on top of carbon paper substrate, not visible because it is hidden by the approximately 50µm thick MPL [44].*

2. Membrane

The membrane plays an essential role in the operation of the fuel cell, in particular for transfer of protons generated at the anode by hydrogen oxidation to the cathode, where they take part in oxygen reduction.

According to the operating principle of a membrane, hydrogen is oxidized to protons, while electrons are transported in the external circuit; protons migrate through the ionomer membrane to the cathode where they participate in the reduction of oxygen. According to this principle, the membrane material must have the following properties:

- The lowest possible proton transfer versus high ionic conductivity to reduce ohmic losses.
- The highest electronic resistance to avoid any risk of electrical short risk.
- The lowest permeability for better efficiency but also for safety reasons: no permeation of hydrogen to the cathode and no permeation of oxygen to the anode, otherwise, the two reactive gases in presence will combine to form water on the catalyst, but without producing electricity.
- Sufficient chemical, mechanical and thermal stability properties under the operating conditions of the cell.

The commonly used material for membranes for PEMFC is Perfluorosulfonic acid polymers (PFSA). Due to electrochemical stability requirements, perfluorinated materials have been identified as the best candidates for satisfying the needs of the system. They have excellent proton conductivity and thermomechanical stability. They consist of a PTFE backbone composed of pendant perfluorinated chains terminated by a sulfonic group ($-SO_3^-H^+$) to ensure the protons transport. They are extruded into sheets of required thickness which is usually between 10 and 250µm [67–69]. The traditional

extrusion-casting process was developed for thick films, generally above 125 μm, but in recent decades, several research studies have evolved the process to obtain the thinnest possible membranes to decrease ionic resistance and reduce their cost, without compromising their thermomechanical stability and performance [70–73].

Water management is an important role of the membrane to ensure ionic conductivity. The water content of the membrane is characterized by the ratio of moles of water per mole of sulfonic acid sites; this parameter is called λ. A threefold increase in the ion conductivity of the membrane is observed when λ goes from 0 to 6 [74]. In fact, it can absorb 50% by water mass and swell which has a direct impact on its physical properties.

Nafion™ ionomers are the most commonly commercialized, as well as Gore-Select®, Aciplex® and Flemion®. The chemical structures of the different membranes are presented in ***Figure 9*** [75]. Even though several alternate polymer membranes, including nonfluorinated type, have been developed, Nafion membranes are still considered the benchmark material. They are developed and produced by the E. I. DuPont Company. These materials are generated by copolymerization of a perfluorinated vinyl ether comonomer with tetrafluoroethylene (TFE).

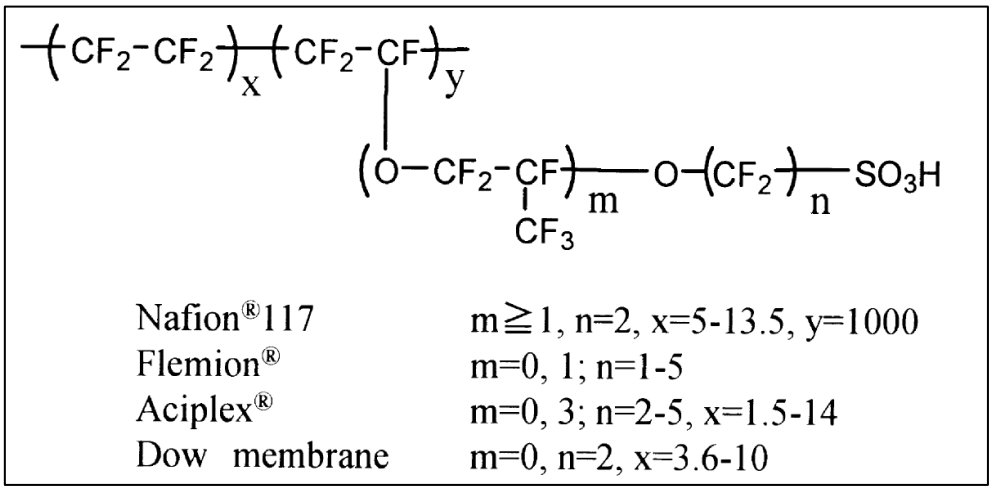

Figure 9: Chemical structures of perfluorinated polymer electrolyte membranes [75].

Membrane reinforcement

In order to develop thinner and stronger electrolyte membranes capable of withstanding more severe operating conditions and offering lower resistance to proton transport, reinforced composite membranes were developed. As shown in ***Figure 10***, the PTFE reinforcement layer is inserted in the middle and surrounded by the two Nafion™ layers.

It was shown that membrane reinforcement can increase the mechanical strength and may allow the use of thinner membranes and lower equivalent weight ionomers, resulting in overall lower resistance to proton conductivity. Reinforced PFSA membrane also has higher mechanical strength and lower in-plane swelling than the unreinforced membrane. This results in lower stresses and less plastic deformation in the reinforced membrane during fuel cell operation, which should result in higher fuel cell durability [76,77].

To produce this reinforced membranes, different ways are employed. For example, porous polytetrafluoroethylene can be impregnated with PFSA solution, in order to make thin cation transporting membranes [78]. In addition, PTFE-reinforced woven membranes were developed by DuPont, referred to as Nafion™ 324 and 417 membranes, the relatively coarse weave of the woven PTFE reinforcements results in membranes that are much too thick for high fuel cell performance [77].

Fuel cells containing these reinforced membranes have been shown to have longer lifetimes than those with homogeneous PFSA membranes highlighting that the dimensional stability of the membrane in the plane is an important factor in improving durability [79].

Tests of Gore-Select® membranes, described as new micro-reinforced polymer electrolyte, have shown improved tear strength, greater dimensional stability, high proton conductance, improved water distribution in operating fuel cells and increased durability [80–85].

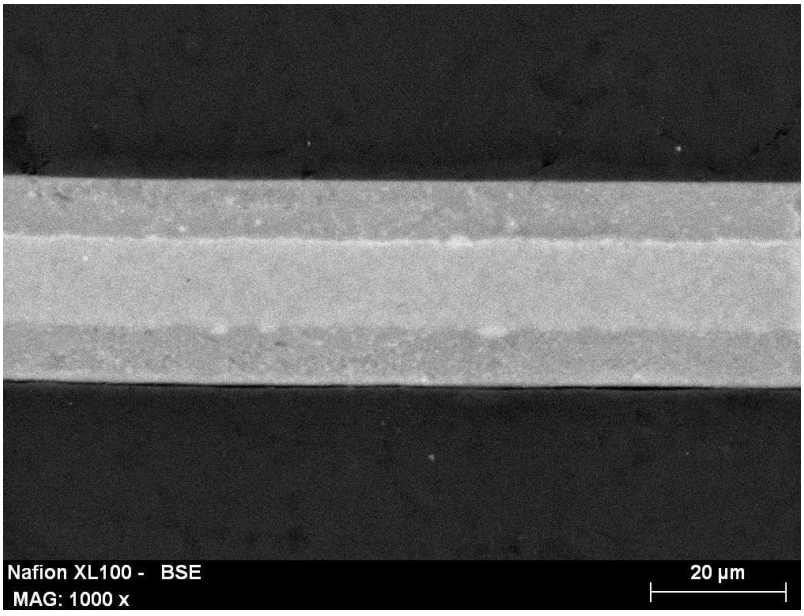

***Figure 10**: SEM image of a PFSA-reinforced XL100 membrane (Adapted from [86]).*

3. Catalyst layers

Catalyst layer is located between the gas diffusion media and the membrane. It is a multiscale composite composed of an ionomer, a carbon support, a noble-metal-based catalyst (here Pt) and void regions which forms the triple points where the electrochemical reactions take place (***Figure 11***).

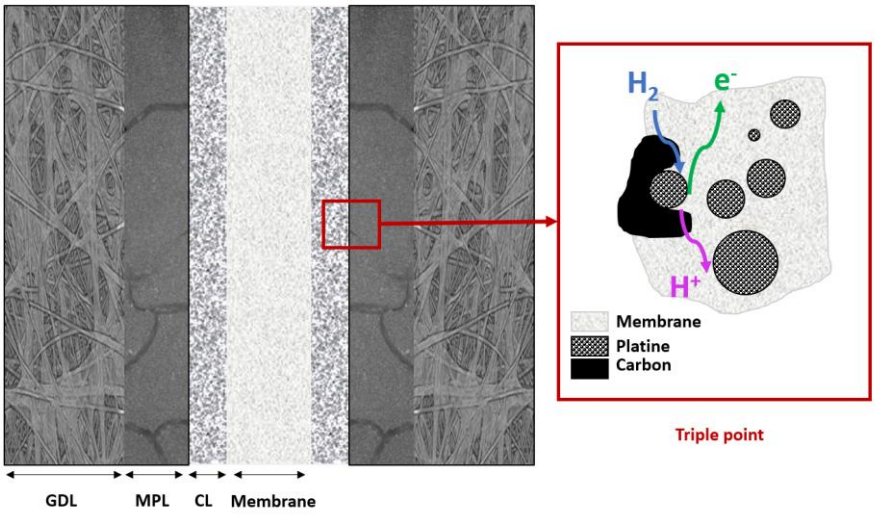

Figure 11: *Schematic representation of reactants and electron transport in a catalyst layer of a PEMFC (triple point).*

The ionomer material is used for proton conduction, and the carbon support is applied for electron conduction. The catalyst used is generally platinum; the nanometer length size for the platinum particles provide theoretical surface areas of over 100 m^2/g and fuel cell active areas of 25-40 m^2/g [74]. Finally, void regions in the membrane provide sufficient mass transport channels for reactants and products. Therefore, an effective three-phase interface design is necessary to improve cell performance [88,89].

The specific properties of catalyst layers are hydrophilicity, and thickness, and the appropriate ratio between ionomer and supported catalyst. They are cast from a solution containing ionomer as a binder to obtain a thin film.

4. Fabrication process of MEA

The fabrication process of MEAs follows 2 major steps. First, the catalyst layer is deposited either on the membrane (CCM) or on the GDL (CCB). Afterwards, the 5 layers (GDLs, CLs and the membrane) are assembled by a hot-pressing process (***Figure 12***).

CL deposition

The CCB process was once privileged for industrial reasons as it guaranteed higher production rate, however it has several limitations. For example, a large portion of catalyst may soak into the GDL and be wasted when the catalyst layer is hot pressed onto the membrane [90]. Moreover, the erratic thickness of a typical catalyst layer, combined with variations in the impregnation depth of the recast ionomer, result in areas where the catalyst layer is not fully impregnated and areas where the ionomeric additive could extend further into the electrode than the catalyst layer. As a result, an unnecessary transport barrier is introduced to the diffusion of gas through the backing. Not

surprisingly, it is difficult to match the impregnation depth exactly with the depth of the catalyst layer in an electrode of this construction [91].

The CCM process is the conventional method approved nowadays as it has many advantages. Good contact between the catalyst layer and the electrolyte membrane is ensured, which allows for a higher active area by extending the triple point and thus better performances [92,93]. It is also possible, via this method, to effectively reduce the catalyst content without compromising the cell performance. It was shown that a decrease in the usual Pt loading in the catalyst layer from 0.4 to ca. 0.1 mg Pt cm^{-2}, does not result in any serious loss of the fuel cell performance [93].

Different methods can be followed to deposit the CL in the CCM process. Either the catalyst dispersion is deposited directly onto the membrane or the dispersion is first deposited on a decal substrate and then transferred to the membrane, with or without an ionomer interlayer. Depending on the properties required, different routes and methods can be used. ***Table 1*** reports the majority of published studies on this subject based on the review of Strong *et al.* [94].

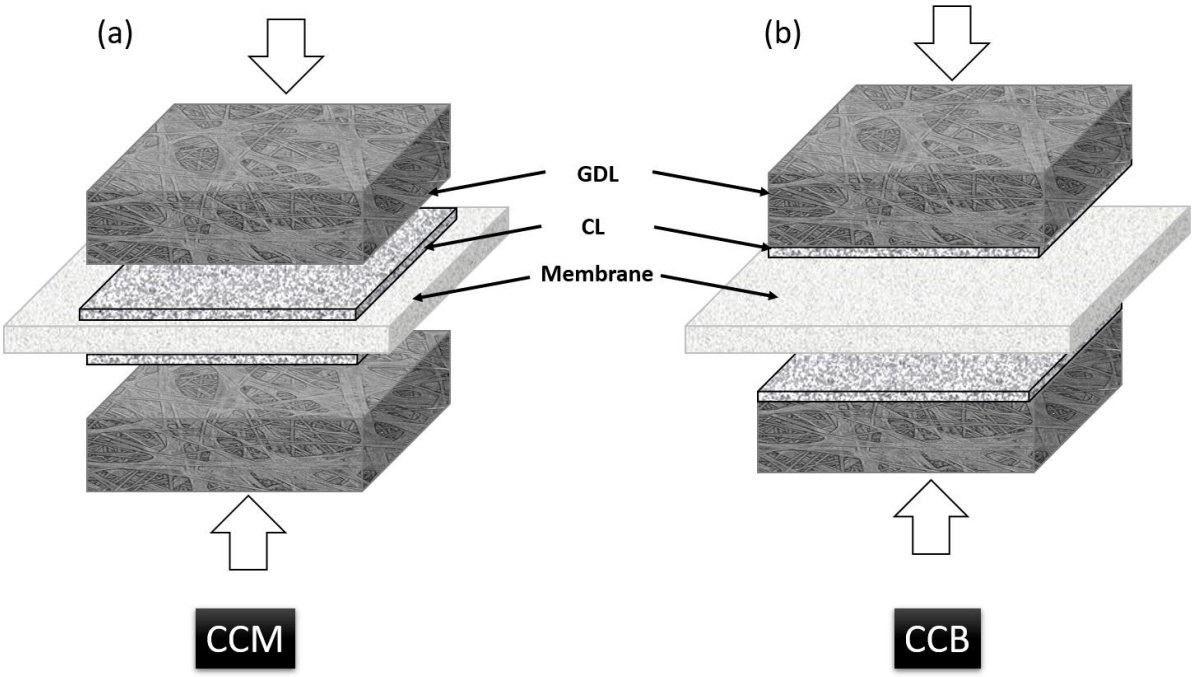

Figure 12*: Assembly processes (a) CCM (Catalyst Coated Membrane) and (b) CCB (Catalyst Coated Backup for MEAs).*

***Table 1**: Main methods for catalyst layer deposition [94].*

Method	Process	Pt loading (mg/cm^2)	Reference
Powder-based methods	Teflon bonded CL	4	[95]
	Brush coating	4	[96–100]
	Screen printing	N/A	[101,102]
	Dry powder	N/A	[103–105]
	Doctor blade	N/A	[106,107]
	Inkjet printing	0.021-0.5	[108–110]
Vapor-based methods	Plasma sputtering	0.001-0.08	[111–113]
Electrical processes	Pulsed electrodeposition	0.025	[114–116]
	Electrospray	0.01-0.3	[117–119]
	Electrospinning	0.877×10^{-3}-0.1	[120–122]
Nanostructured catalyst layers	Nanostructured CL	N/A	[123,124]

Other methods are being developed and optimized to improve the transfer efficiency of the CLs to the membrane and the power density of the cell. The other objective is to reduce the cost of these CLs and to substitute platinum by introducing nanofibers. iNFS-CLs were fabricated by performing multiple cycles between the electrospinning of Nafion™ nanofibers and the electrospray of a catalyst ink, until reaching the desired Platinum loading rate. Higher performances were thus obtained and the ionomer densities near the catalyst surfaces were reduced leading finally to ultimately suppressing catalyst poisonings by anionic groups from the ionomer [125].

5 layers assembly

The 5 layers (GDL, CL and membrane) are then assembled in a hot-pressing step as depicted in ***Figure 13***. One way to promote good contact within the triple point region, gathering point of electron conductors, proton conductors and reactants and where all the electrochemical reactions take place, is through hot-pressing process, which reduces the electrical potential drop and contact resistance in the cell [30,126–129]. During this phase, compressive stresses between 1 and 10 MPa are applied, at temperatures between 80 and 160°C for 1 to 5 minutes [126,127,130].

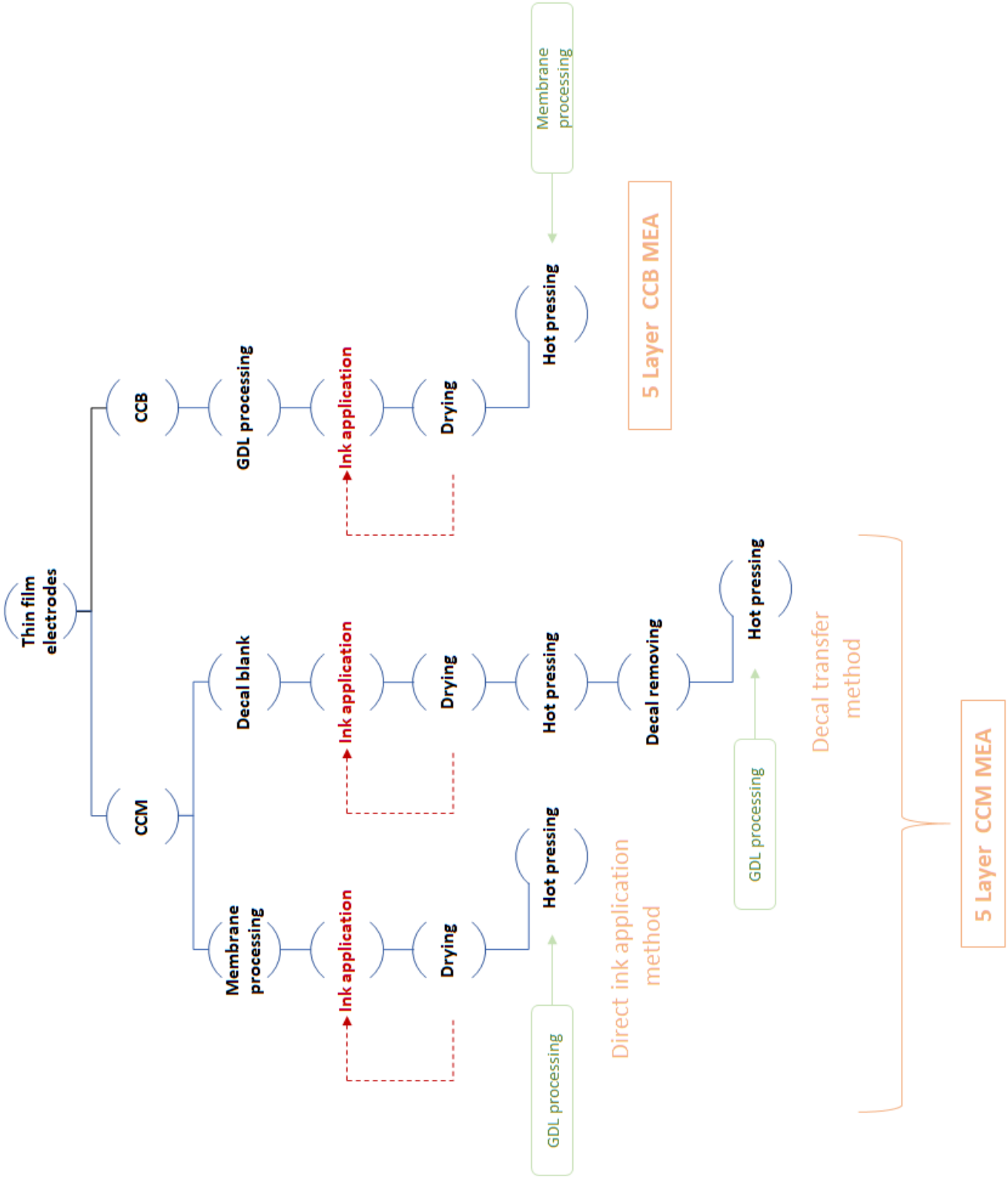

Figure 13: *CL deposition and assembly methods for MEAs (Adapted from [131]).*

The hot-pressing process is important to conform the surfaces to maintain a good contact and reduce contact resistance between the layers; different parameters should be controlled to optimize the assembly procedure. For this purpose, a variety of combinations between the parameters can be used.

Figure 14 shows cross-sectional XCT views of the MEA before and after the bonding process, wherein the post bonded MEA shows improved interfacial contact; the study also shows that the lamination procedure leads to the CCM creep into the GDL voids [132].

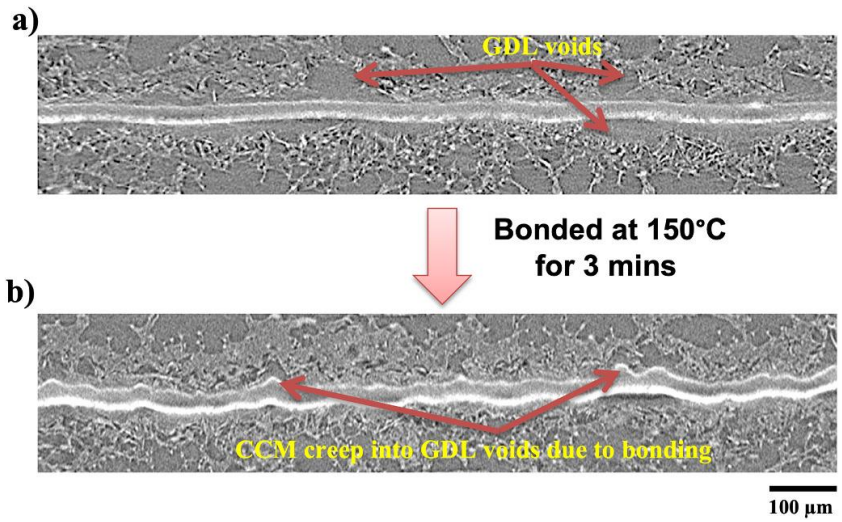

Figure 14: *Cross sectional XCT views of the MEA (a) before and (b) after hot-pressing [132]*

III. Mechanical phenomena influencing the PEMFC's performance and durability

The performance of the cell is linked, among other parameters, to the mechanical behavior of each of its components and the quality of its interfaces, under the various assembly mode as well as the operating conditions. The understanding of the mechanical behavior of the components of the cell allows the prediction of the different strains and stresses that might occur after several operating cycles, thus increasing its durability.

1. MEA mechanical behavior

The combined action of the MEA manufacturing process firstly and the stack assembly phase and operating conditions imposed secondly results in uneven mechanical solicitations between components and at the various interfaces. Therefore, understanding how each component and the different interfaces reacts under these stresses is crucial not only to prevent the damage of the fuel cell but also to extend its lifetime while ensuring good performances.

This part of the study aims to describe the mechanical behavior of each component of the fuel cell core as well as the mechanical properties at its interfaces; and the different characterization methods reported in the literature will also be specified.

2. Mechanical behavior of the different components

Gas diffusion layer

Experimental characterization of GDL

The GDL is an orthotropic material (***Figure 15***) [133]. In material science and solid mechanics, orthotropic materials have mechanical properties which differ along three mutually orthogonal axes, where each axis has double rotational symmetry.

Figure 15 shows a GDL with its different axes of symmetry, in the plane with the machine (MD) and orthogonal (CD) directions, x and y respectively, and out of the plane, described by the z axis.

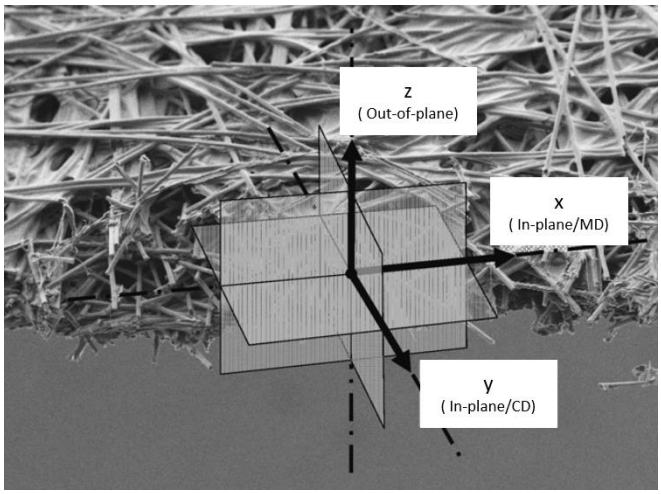

Figure 15*: SEM cross-section and fiber structure of TGP-H-060 with virtual (macroscopic) symmetry planes (Adapted from [133]).*

GDL is characterized by a high anisotropy of its properties due to its particular structure of unidirectional fibers dispersed in the plane and high porosity; therefore, many tests are needed to determine the stiffness matrix of GDL in its different directions.

In plane properties can be determined via tensile tests, *i.e*. in plane modulus, tensile strength, tensile strength at break, yield strength and elongation at break [134–139].

Taber stiffness tester is also used to characterize GDLs; in particular, it has been shown that the Taber bending stiffness value in the machine direction (MD) is higher than that in the cross-machine (CM) direction and that the degree of anisotropy of felt GDLs is more pronounced than that of the paper GDL [140]. The ratios of MD/CD bending stiffness for two felt GDL references are equal to 46.1 and 5.1 compared to 1.36 and 1.37 for paper ones. Moreover, it was shown that carbon cloths are mechanically less stiff than carbon papers by a factor of about 2 [44].

Poornesh *et al*. [141,142] also used Taber stiffness method to measure the in-plane elastic properties. They found that in plane moduli are between 1 GPa and 5 GPa in the machine direction and 0.9 GPa and 2 GPa in the cross-machine direction for all roll GDLs and are lower than 0.02 GPa for cloth type in both directions.

Kleemann *et al*. [133] measured in-plane elastic moduli of GDLs using a 3-point bending test following the DIN 53121[143] and EN 13706-2 [144] standards. They showed that moduli are higher in the machine direction than in the transverse direction and that sheet GDL (TotayH060) has a higher modulus compared to roll types; the moduli being equal to 9 GPa and 5 GPa in the machine and cross directions respectively, as opposed to the roll GDLs where both moduli are lower than 2 GPa for the three references. They also used the short-beam bending method to determine the shear modulus. The out-of-plane shear modulus is equal to 20 MPa and 17 MPa respectively in the machine and cross machine directions for the TorayH060 GDL, while for roll references, it is between 6 MPa and 13 MPa in the machine direction and between 5 MPa and 10 MPa in the cross-machine direction. They finally showed that the out-of-plane Poisson coefficient of these different GDL is close to zero.

Chen *et al*. [145] performed tensile tests following the standard ASTM D638 [146] and the shear test was performed according to Lai's method [147]. Tension moduli were found equal to 0.72 GPa and 0.42 GPa respectively in the longitudinal and transverse directions. The in-plane and out of plane shear moduli for the GDL reference JNT-30-A1 was found equal to 1 MPa and 0.5 MPa respectively

Another commonly used test for GDL is compression, as it is representative of the stresses applied in the fuel cell. The GDL undergoes compressive stresses due to clamping pressure and hygrothermal stresses which affects its transport functions and performance. Therefore, it is crucial to understand its behavior under compression. The behavior of a GDL under compression is, generally determined by placing the sample between two flat plates and measuring the strain as a function of the compression force. The procedure can be repeated several times for the same sample to observe the variations of the mechanical behavior under cyclic compression.

Due to the high porosity of the GDL, it exhibits an original behavior in compression characterized by a non-linearity between stress and strain, making it difficult to predict its state with increasing strain (or stress) [44,133,145,148–153].

As shown by Radhakrishnan *et al*. [154], the stress strain curve of carbon paper under compression (***Figure 16***) shows two distinct plateaus; the first (AB) corresponds, according to these authors, to the air gap reduction under compression between the stack of samples and the second (CD) is relative to the closure of pores caused by further increase in the load. The transition between the two plateaus occurs gradually, as presented by region (BC) due the wide pore size distribution of GDLs.

Afterwards, under further compression the final region (DE) depicted in an increasing curve, corresponds to the densification stage.

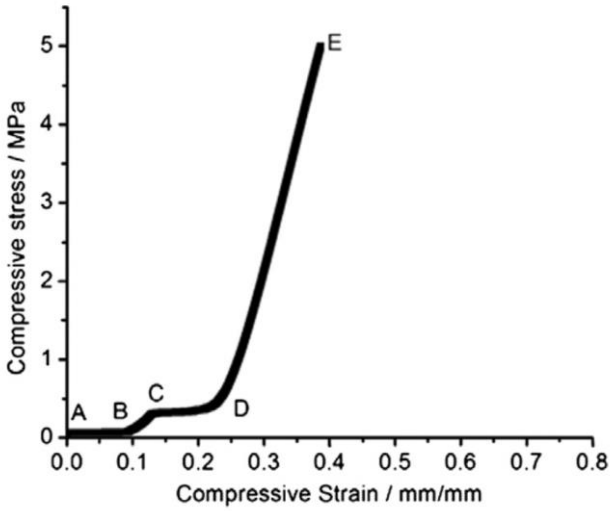

Figure 16: *Compressive stress strain curve for GDL reference Toray (TGP-H-120) (Adapted from [154]).*

Nitta *et al.* [155] have studied the behavior of GDL under inhomogeneous compression caused by the channel/rib structure of flow-field plate, by applying different compression forces. The stress-strain curves presented three distinctive regions; the first of 0-0.2 MPa related to the smoothing of the GDL surface, where the strain increases. The second region, from 0.2 to 3.5 MPa, is related to the crushing of the hydrophobic pores and the third one corresponding to the crushing of the hydrophilic pores and it ranges from 3.5 MPa to 5.5 MPa.

Another study by Ismail *et al.* [156] investigated the compressibility of a number of GDLs; they showed that the stiffness is enhanced with the PTFE content and in presence of MPL. Under a stress range of 1MPa to 3.2MPa, the average Young's modulus in compression increased from 11 MPa to 15 MPa when the PTFE content was increased from 5wt.% to 30wt.% and in the presence of MPL, the modulus reached 18MPa.

It has also been shown that the initial thicknesses decreased when the load is removed [157]. For example, after a cycle of compression with a maximum value of 2.5 MPa, the initial thickness of GDL is reduced by 32% after unloading, showing the presence of residual deformation [153].

Escribano *et al*. [149] measured the thickness variation of several types of GDLs under a range of stress from 0 to 10 MPa. They found that the thickness of GDLs decreases sharply after the first compression and that the carbon cloth has the highest compressibility. Contrarily, the carbon felt is less compressive and shows stable behavior after the first test. Moreover, the samples with PTFE coating were found to be less compressive than those without coating, a result confirmed by the study of Sadeghifar *et al*. [158].

Mishra *et al.* [148] also measured the compressive modulus of different types of GDLs. Values of the compressive modulus are obtained by the compression stress strain plot into three to four regions such that in each region the curve exhibits a linear trend and is characterized by a constant E_c. the latter is determined as the slope of the best fit straight line that passes through each of the specified regions. Values of Ec are reported in ***Table***

2. As depicted in the table, the paper-based GDLs present three linear regions in contrast to cloth-based ones that have four regions.

Table 2: *Compressive modulus as a function of the pressure range for different GDL references [148].*

GDL	Pressure range (MPa)	E_c (MPa)
GDL-10BA	0.00 – 0.15	1.71
	0.15 – 1.12	4.59
	1.12 – 3.00	6.16
GDL-10BB	0.00 – 0.16	1.81
	0.16 – 0.52	5.11
	0.52 – 3.00	8.57
B-3/2050	0.00 – 0.11	1.32
	0.11 – 0.57	6.27
	0.57 – 3.00	13.72
B-2/120	0.00 – 0.11	1.75
	0.11 – 1.11	6.29
	1.11 – 3.00	8.58
B-1/D	0.00 – 0.23	0.95
	0.23 – 0.57	3.31
	0.75 – 1.53	7.56
	1.53 – 3.00	16.90

Modelling the nonlinear mechanical behavior of GDL in compression

Given the difficulty of handling these very thin materials and their heterogeneous structure, many studies have focused on predicting the non-linear behavior of GDLs under monotonic or cyclic loading. different approaches have been used, whether based on discrete fiber models, analytical or polynomial laws [159], 2 or 3-D finite element calculations incorporating or not the tooth/channel structure present in the bipolar plates [160,161], the difficulty in the latter case lies in the detailed description of the heterogeneous microstructure of the GDL and its various components or constituents. On the other hand, their interest lies in predicting the intrusion of the GDL into the channel as a function of the loading rate, which has a major impact on the performance of the fuel cell [147,162,163].

Early models assumed a linear isotropy of GDL in compression. For example, it was used to analyze the rate of intrusion of GDL into the flow channel [162], to predict the contact resistance at the interface between the BPP and GDL [164,165], to study the distribution of contact pressure [166–168] or to study its influence on the deformation of the membrane [160,161].

More recently, the orthotropic behavior of GDL has been integrated in the model developed by Garcia-Salaberri *et al.* [169]; it produces a much more detailed relationship between mechanical properties and the resulting physical changes such as intrusion of the GDL into the flow channel and contact pressure. These authors have shown that the linear isotropic models widely reported in the literature tend to overestimate the porosity

and the intrusion of the GDL in the channel region, and may lead to inaccurate predictions in terms of interfacial contact pressure distributions.

Kleemann *et al.* [133] also considered an orthotropic material in their prediction of the mechanical and electrical behaviors of GDL. The combined action of assembly and hygrothermal loading was then predicted using a model incorporating orthotropic behavior, and revealed their influence on the intrusion of the GDL into the channel and on the stress distribution [170].

Firat *et al*. [171] used finite element approach to analyze the fuel cell stack design from a mechanical point of view, they analyzed a fuel cell stack with an active area of $50cm^2$. They employed the nonlinear orthotropic material to model the GDL's behavior, but they only used the through-plane elastic modulus and not the through-plane shear modulus of GDL.

Yi *et al*. [172] used a numerical model to estimate elastic properties of a unidirectional GDL. They used a micromechanical model for porous material and assumed carbon paper is macroscopically homogeneous and transversely isotropic. Values are presented in ***Table 3***.

To validate their results, they performed uniaxial tensile and compression tests. The experimental values for the in plane elastic modulus (in both longitudinal and transverse directions), the out-of-plane modulus, the shear moduli in both planes and the in-plane Poisson's ratio are presented in ***Table 3***. Directions are chosen following ***Figure 15***.

It should be noted that the shear moduli are determined via the classical relation as a function of the Young's modulus and the Poisson's ratio.

For the tensile test, bonded resistance strain gauges were used to measure the longitudinal and transverse strains in order to estimate the in-plane Poisson's ratio.

They confirmed the non-linearity of the GDL's behavior under compression and found that in-plane tensile modulus is much higher than out-of-plane compression modulus. The deviation between the experimental and the estimated numerical of the different elastic moduli was less than 18%.

Table 3: *Numerical and experimental results of the elastic properties of carbon paper GDL (Adapted from [172]).*

Property	$\mathbf{E_x}$	$\mathbf{E_y}$	$\mathbf{E_z}$	$\mathbf{G_{xy}}$	$\mathbf{G_{yz}}$	$\mathbf{v_{xy}}$
Unit	MPa	MPa	MPa	MPa	MPa	N/A
Numerical value	3630	3630	8.79	1350	8.55	N/A
Experimental value	3950	3790	7.47	1540	N/A	0.28

A recent study by Leng *et al.* [173] compares the impact of using an isotropic or orthotropic model on the GDL properties and thus on the transport functions in the

PEMFC, it was found that the orthotropic model and the parameters utilized are more effective in analyzing the deformation of GDL compared to the isotropic one.

Mechanical properties of Proton exchange membrane

The mechanical properties of the membrane have been the subject of a large number of studies. In this paragraph we will describe the main ones and the associated tests to obtain them. As for any other material, the tensile behavior is the most common way to determine the different elastic constants, such as Young's modulus, yield strength or strength and strain at break. In addition, as the membrane is sensitive to relative humidity, these properties have been measured at different degrees of hydration [83,174–177]. PFSA membranes are viscoelastic materials; their response to stress is time-dependent. In the end, the overall response of a PFSA membrane to mechanical loading can be separated in three different regions: (i) elastic and recoverable deformation, followed by (ii) yield limit, associated to the onset of nonlinearity, (iii) post-yield or strain-hardening regime, that happens after further stretching at higher strains, and finally (iv) breaking [178–180].

Kawano *et al.* [175] determined the tensile mechanical properties of Nafion™ membranes in acid form at different water contents (λ) and temperatures by Dynamic Mechanical Analysis tests. In particular, they observed that the elastic modulus decreased from 2 MPa to 0.95 MPa, when the membrane was soaked in water for 24h. It also changes from 2.10 MPa to 0.02 MPa when the temperature is increased from 27°C to 180°C. Tang *et al.* [174] investigated the mechanical properties of PFSA membranes using tensile tests performed under different relative humidities and temperatures in a custom-designed environmental chamber. Young's modulus, yield strength, tensile stress, and tensile strain were measured for 16 combinations of temperature and relative humidity, with temperature ranging from 25°C to 85°C and humidity from 30% to 90%. The results of this study (***Figure 17***) show decreases in Young's modulus in the machine direction (a) and in the transverse direction (b) with temperature and relative humidity. These authors also showed that the yield stress of the PFSA membrane decreased with increases in relative humidity and temperature, while the failure stress only decreased with increasing temperature.

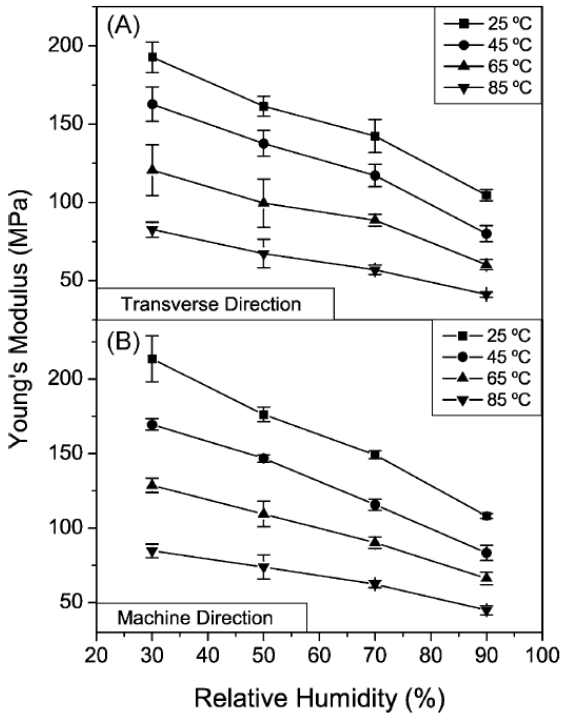

Figure 17*: Variations of the Young's modulus as a function of relative humidity % at different temperatures (A) in transverse direction and (B) in the machine direction [174].*

Satterfield *et al*. [181] also performed tensile tests on Nafion™ membranes under a temperature range of 20°C to 120°C, the water content was modified by preconditioning the samples in controlled-humidity environments and determined by weighing the sample before and after testing. They determined the Young's modulus and the so-called by the authors "plastic modulus"; the latter corresponding to the change in stress with strain above the yield point, which is a measure of the strain hardening of the material ***Figure 18***.

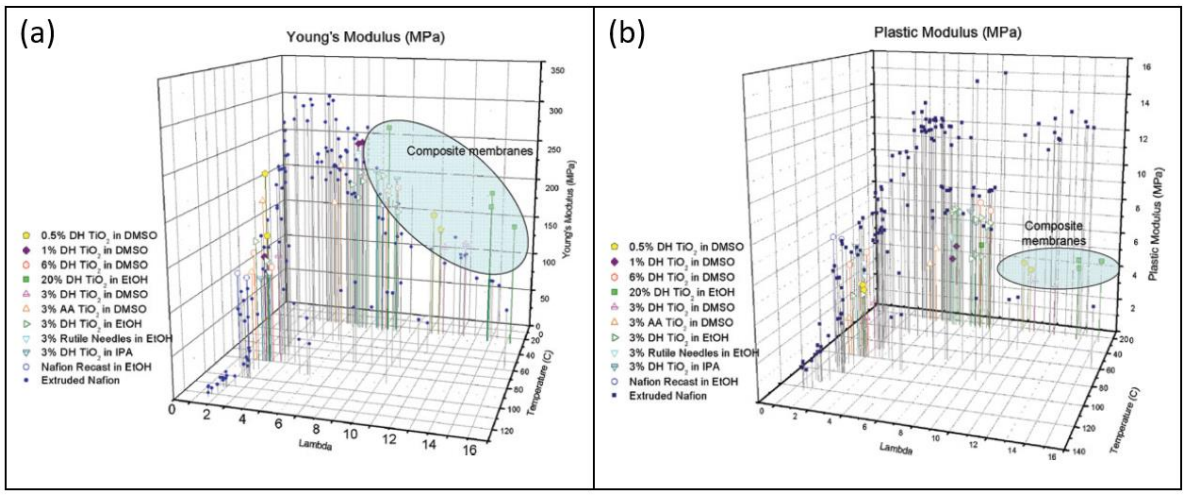

Figure 18*: (a) Elastic modulus and (b) plastic modulus, of Nafion and Nafion/Titania composite membranes, under different temperature and water content (lambda) values [181].*

These authors confirm the decrease of elastic modulus from 300 MPa to 100 MPa when the temperature increases up to 80°C and then drops to about 10 MPa above 100°C temperature being relative to the glass transition temperature $T_{g.}$ of the membrane. At 25°C, the elastic modulus decreased from 300 MPa to 50 MPa when the water content in the membrane increases.

The same trend is observed by the authors for the "plastic modulus", decreasing from 8 to 2 MPa between 25 and 110°C but seems insensitive to the variation of water content. The creep tests carried out by the authors showed that its intensity increases with the increase of the temperature and the decrease of the water content.

Other studies investigating the time-dependent viscoelastic response of PFSA membranes under different temperatures and humidities confirmed these results [177,182,183].

Solasi *et al*. [176] developed an elastoplastic model to predict the experimental results for the strain-rate dependence and the stress-relaxation behavior of the membrane. In particular, they showed using the elasto-plastic model, based on the nonlinear experimental curves as well as the hygrothermal expansion coefficients of Nafion™ [64] that hydration has a greater effect than temperature in the development of mechanical stresses in the membrane, which can be critical when forming a non-uniform hydration profile or a pinhole through the membrane.

A finite element model was used by Tang *et al.* [174] to study the influence of hygro-thermal stresses on the membrane assuming linear elastic behavior of the membrane. They studied the impact of the cell clamping method, considering either a fixed load or displacement and under aligned or alternating gas channels; these different configurations were furthermore studied for three membrane thickness (25µm, 50µm and 100µm). They then showed that the in-plane stress σ_{xx} is the dominant stress in the membrane compared to the out-of-plane stress σ_{zz} and the shear stress σ_{xz} (Figure XX). The alignment of the gas channels has a significant impact on the magnitude and distribution of stress; aligned gas channels produce lower hygrothermal stresses than alternating channels. They pointed out that fixed displacement fuel cell stacks generate

higher stresses in the membrane than fixed loading stacks. The influence of membrane thickness did not show a significant impact.

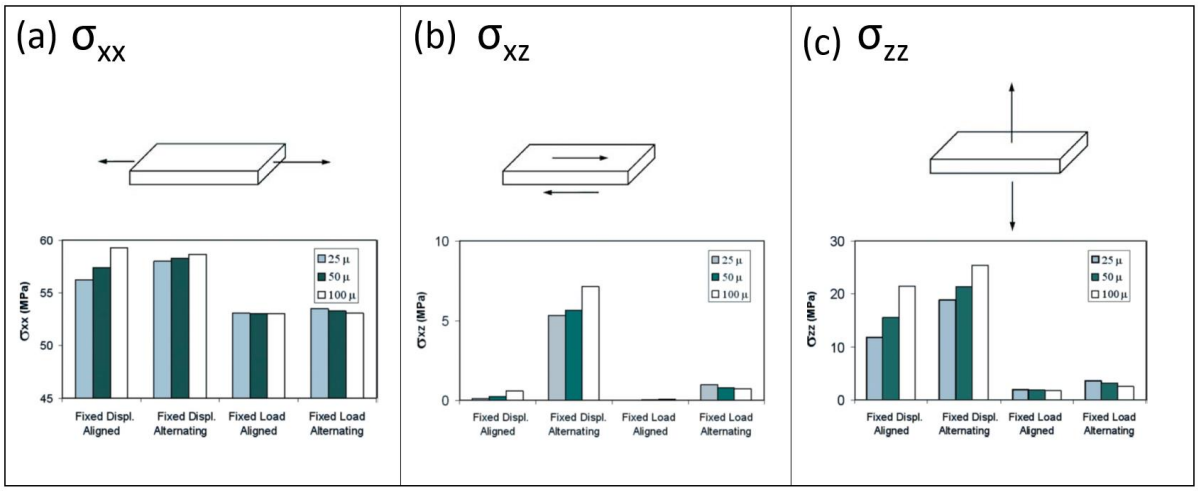

Figure 19: *The maximum (a) in-plane stress (b) shear stress and (c) out-of-plane stress of the membrane under fixed displacement and fixed load clamping conditions, for the aligned and alternating gas channels and for the three different in thickness membranes (Adapted from* [174]).

Khattra *et al.* [68] studied the mechanical response of the membrane under solicitations (thermal, hydric, ...) using experimental measurements and numerical modeling. They proposed a viscoelastic-plastic constitutive model and performed uniaxial tensile and stress relaxation tests. They concluded that the in-plane residual stresses can be significantly reduced by introducing an e-PTFE reinforcing layer.

More recently, Kusoglu *et al.* [160,161] proposed a generalized model of a single cell integrating the mechanical behavior of the membrane under the same loading and unloading conditions as in a stack, i.e., under different loading and unloading conditions in water and temperature (***Figure 20***). The evolution of the stresses during an operating cycle is determined using a 2D finite element model comprising the five layers described above assembled according to the two clamping methods studied by Kusoglu *et al.* [161] then showed that compressive plastic deformation occurs in the plane of the membrane during hygrothermal loading, which are the cause of residual tensile stresses in the membrane after unloading. These stresses are considered a critical factor favoring future mechanical failures of the membrane. Such a model appears to us at this stage of the study to be the most complete and we will come back in chapter 4 on its possibilities of evolution.

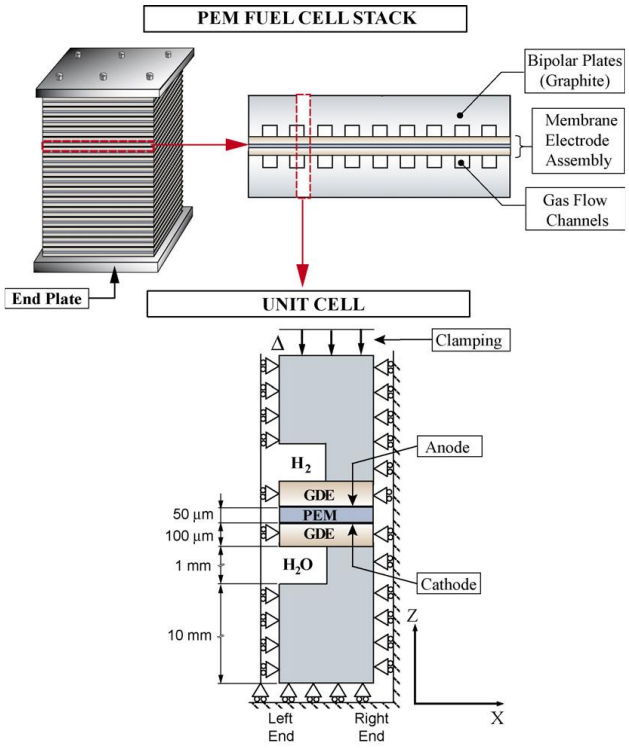

Figure 20: *The geometry of the unit cell used in the simulations of Kusoglu et al. [161]*

3. Influence of the interfaces on the mechanical behavior of the MEA

After having described the main studies relating to the mechanical behavior of the various components of the cell, it seems important to us at this stage to analyze the influence of the interfaces between the 5 layers on the global mechanical behavior of the cell core or MEA (***Figure 21***).

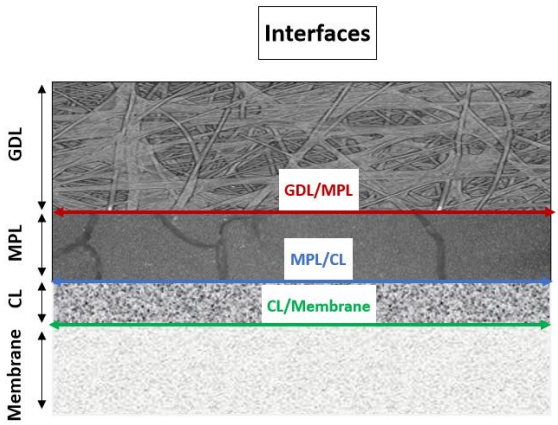

Figure 21: *MEA layers and interfaces*

Among the various published studies, we can cite the work of Jia *et al.* [184] who performed fracture tests using Double Cantilever Beam (DCB) method to study the separation of a membrane (CCM) with its catalytic layer (CL) under ambient conditions.

They observed cohesive fracture of the CL for all tests, which proves that there is a stronger adhesion at the CL/membrane interface than in the catalytic layer, previously deposited in a CCM process. Similar results were reported by Byun *et al.* [185], based on the optimized SAICAS (Surface And Interfacial Cutting Analysis System) method performed on CL also deposited by the TLC method. According to these authors, the adhesive strength at the cathode-membrane interface was about eight times higher than the average cohesive strength in the bulk regions of the cathode due, according to the authors, to the high degree of intermolecular diffusion of the ionomer binders at the interface.

The influence of ionomer content in the catalytic layer was studied by Ma *et al.* [186] on different substrates (Nafion 117, polyester film and solid graphite composite); the results showed that if the ionomer content was less than 20 wt%, the catalyst adhered poorly to the Nafion™ membrane compared to other substrates.

In the case of a CCB deposit, De Moor *et al.* [187] have shown, from tensile tests on MEAs, that the force required to shear the membrane/electrode interface decreases with ageing time; one of the causes mentioned by the authors to explain this phenomenon is the plastic deformation accumulated at the membrane/electrode interface, *i.e.* a fatigue stress due to the multiple hygrothermal cycles undergone by this assembly

Finally, we can mention the original study by Uchiyama *et al.* [188] who measured the static friction coefficient between a membrane (CCM) and a GDL (25BC). They measured, using the ball-on-flat method (***Figure 22***), a static friction coefficient between the CCM and the GDL ranging from 0.25 to 0.85 when the contact pressure increases from 0.15 to 0.60 MPa. This study, particularly interesting in its approach, may however raise questions about the dependence of the friction coefficient on the applied normal force.

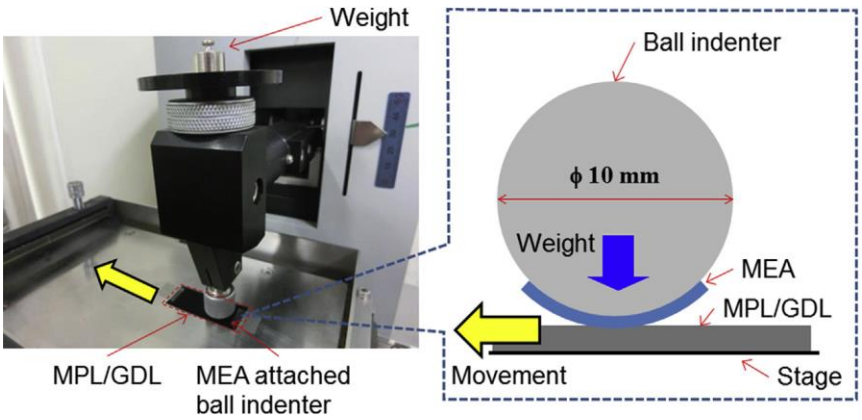

Figure 22: *Friction test machine and schematic diagram of MEA and GDL used by Uchiyama et al. [188].*

It should be noted that few theoretical studies have been carried out to describe this subject, mainly due to the small number of experimental results available in the literature, linked to the complexity of carrying out tests and measuring properties at the interfaces of thin films.

However, we can mention the work of Tang *el al.* [174] and Al-Baghdadi *et al.* [189] who showed that the heterogeneous distribution of stresses in the different components could induce localized bending, which can contribute to delamination between the membrane and the GDL. This delamination phenomenon could have a negative impact on water management due to the presence of gaps between the different layers of the MEA impairing the transport functions. In the study by Bajpai *et al.* [190], a two-dimensional, non-isothermal and anisotropic numerical model was proposed to investigate the effect of the real morphology between the MPL and CL on the fuel cell performance. The model shows a decrease in performance if an interfacial layer is considered. Indeed, the inclusion of an interface layer causes water infiltration between the layers and a decrease in conductivity. This result was confirmed by Zenyuk *et al.* [191] via the development of a deterministic elastic contact mechanics model applied to the interfaces of compressed microporous and catalytic layers in polymer electrolyte fuel cells (PEMFC).

The failure mechanisms for laminated MEAs may occur under excessive mechanical solicitations or after numerous cycles of operation. Therefore, to maintain the durability of the cell it is crucial to understand and thus prevent the formation of the defects that might alter the different layers forming the MEA as well as the interfacial cohesion between them.

IV. Influence of the stack assembly and operating conditions on MEA mechanical state

After focusing on the behavior of the different layers of the MEA in the previous section, we will report the results from the literature related to the influence of the assembly conditions on the mechanical behavior of the fuel cell core and in particular on the GDL, the proton exchange membrane or the MEA interfaces.

1. Gas diffusion media

The gas diffusion layer is subjected to numerous mechanical stresses during the manufacturing process related to the assembly of the MEA, the stacking of the different cells in the stack and then during the operation of the fuel cell. The deformations undergone by the gas diffusion layer then have a direct impact on the transport functions, including mass transfer and electron migration. Even if the cell is assembled with an optimal compression force during installation, the GDL will undergo multiple mechanical stresses related to variations in external hydrothermal conditions [192].

The external compression force has a huge impact on the morphology of the GDL [193–195]; indeed, cyclic compression causes significant and irreversible changes in its microstructure, leading, for example, to a decrease in the average pore size and distribution of nearly 70% under a compression stress of 10 MPa [196]. This significant decrease in porosity inhibits gas flow and blocks water evacuation [150,163,197–200].

Such mechanical stresses affect the structure of the GDL and change its physical properties, accelerating its degradation process until it breaks down over time [201]. Other GDL degradation mechanisms have been observed during battery operation, such as phenomena related to oxidation [202,203] or to the decomposition of PTFE [204].

The modification of the GDL porous structure induced by mechanical constraints leads to a reduction of its electronic conductivity and hydrophobicity. Chemical oxidation of the GDL accentuates this loss of properties and can lead to an alteration of the water balance in the MEA limiting the mass transport of reactants, further reducing the performance of the MEA and the durability of the fuel cell [205,56,202,203].

2. Proton exchange membrane and its catalyst layers

A part from the constraints resulting from the assembly, the mechanical behavior of the membrane is highly dependent on the hygrothermal conditions. The design of the system that ensures good contact among the various fuel-cell layers causes the membrane to either compress or be constrained by other layers on top [206], the membrane is constrained in compression due to swelling when humidity increase, it becomes, however, tensile after shrinkage when humidity decrease. The alternating compressive/tensile stresses induce degradation and the ultimate failure of the membrane, which would be exacerbated by inherent defects in the membrane or the inadequate assembly of fuel cell stack [207,208]. In fact, Solasi *et al.* [176] considered this change in relative humidity as equivalent to mechanical load, and is believed to be a major driving force for mechanical failure.

It should be mentioned that pinholes formation can be the cause of hydrogen crossover [209] and could be at the origin of flooded areas causing further loss of apparent catalytic activity [209–212].

However, even in the absence of electrochemical effects, the fatigue failure was found to be one of the main causes for the mechanical degradation of MEA since the cyclic stresses may also lead to the creation of small holes in the areas that are under high stress concentration [213].

Another effect of hygrothermal loading leading to the alteration of the membrane's mechanical properties, is that, if humidity is too high, it could lead to flooding phenomena causing increased mass transport losses, however it should be noted that if the humidity is too low, the membrane will dry out, leading to increased ohmic losses [214].

The other parameter to consider is the pressure distribution which also has an impact on the mechanical state of the membrane [166,215]. It has been shown that if the stress distribution in the membrane is not uniform, due to a difference in stiffness between the surrounding layers of the membrane [216], the creation of localized stress zones would further stress the membrane and lead to its failure, the mechanical failure of the membrane usually starts as a random and local imperfection that propagates to a catastrophic failure [217].

Furthermore, compression leads to a reduction of the membrane's thickness affecting conductivity, proton resistance and water sorption [76,160,161]. Weber *et al.* [206] assimilate this phenomenon as a constrained sponge which causes loss of water.

The CL is also affected from the external clamping compression. A CL compression analysis model was established by Malekian et al [218] to simulate the impact of compression on CL characteristics. The pore size distribution (PSD) and porosity of the CL were found to be the two main indicators to describe the microstructure of the CL, the results show that the change in pore size is a function of compression and is related to the initial porosity, pore size distribution, and material properties of the CL.

To sum up, the hygrothermal environment together with the assembly conditions of the fuel cell are one of the reasons of PEMFC performance alteration due to the loss of the conductivity properties of proton exchange membrane, degradation of catalyst layers and the damage of the gas diffusion layers.

3. MEA interfaces

When investigating the degradation mechanisms at MEA interfaces, the most common mentioned phenomenon, is delamination between the layers preceded or followed by cracks propagation.

For example, Guilminot *et al.* [219] reported the formation of cracks at aged cathode/membrane interfaces. They showed that delamination between the CL and the PEM occurred more easily with variations in relative humidity and temperatures.

Yan *et al*. [220] also observed delamination of the CL from the PEM when the cell cathode temperature is below −5°C during cold start studies. Similarly, during frequent freeze/thaw cycles, a shear force induced by the phase transition between liquid and solid water causes interfacial delamination of its layers.

Singh *et al.* [221,222] have studied the fracture propagation phenomenon in CCMs under a range of hydrothermal stresses from 23 to 70°C and 50 to 90%. They found that the CCM crack propagation is accompanied with local interfacial delamination and severe electrode cracking, which leads to the loss of local reinforcement and thus the membrane fracture [223–225]. Consequently, the active surface is reduced and the degradation of the fuel cell is expected [217,226]. In fact, the detachment that occurs between the MEA layers might cause a very weak structure [132,224,227,228], and increase ohmic losses and contact resistance compromising the performances of the cell.

Some studies focused on the mitigation methods to reduce the mechanical impact leading to the degradation of MEA interfaces. For example, Lim *et al.* [216] investigated the impact of the mechanical load induced by the diffusion medium between the interfaces on the performance and durability of the fuel cell. They found that the stiffest GDL (78.4 g.cm, bending stiffness) showed the best freeze/thaw durability; the current density was equal to 600 $mA.cm^{-2}$ compared to 200 $mA.cm^{-2}$ for the least stiff one. In fact, the stiffer GDL can

press more uniformly the active area of the MEA, which helps minimize the membrane deformations caused by the cyclic expansion and contraction under operating conditions.

V. Discussion and subject of study

The PEMFC is subjected to different range of mechanical stresses induced by its assembly process and operating conditions, which have a direct impact on its performance and durability. The state of the art has shown that its response is different from a layer to another in the whole stack, and in particular in the core of the cell where all electrochemical reactions take place.

Throughout this chapter, the work reported shows the difficulty of understanding the relationship between the variations of mechanical stresses induced by the operation of the battery and their consequences in terms of structural modifications of the different layers of the core or the alteration of the interfaces between them.

First, the characteristics and properties of the different layers of the cell core and their fabrication and assembly process have been described more detailed section was devoted to the GDL because of its key role in the reactant diffusion, water management, thermal and electronic conductivity but also due to the lack of information reported in the literature when it comes to its orthotropic mechanical behavior. The nature of the GDL, consisting mainly of dispersed or woven carbon or graphite fibers, makes its characterization complicated; its anisotropic mechanical behavior requires a series of mechanical characterizations in the plane of the fibers and out of plane. The different manufacturing process of the MEA were also detailed starting with the catalyst layer deposition on the membrane or the GDL to the 5-layer assembly processes. By going through all the manufacturing steps of a fuel cell, it is obvious that it undergoes multiple mechanical stresses from the manufacturing of each component to the assembly of the core or the entire stack, source of potential degradation mechanisms at the scale of the layers or interfaces between them.

- **GDL:** the GDL undergoes significant microstructural variations under compression, notably a decrease in its porosity. In fact, it has been in fact shown that pore size is reduced by almost 70% under a compressive stress of 10 MPa [196], which would disrupt its transport functions and cause a decrease in its conductivity and hydrophobicity. Difficulties in transport reactants as well as water management were then observed.

- **PEM:** the membrane expands and retracts when exposed to hydration cycles. the change in hydration is considered equivalent to mechanical load and is believed to be a major driving force for mechanical failure [176]. Several studies confirmed that the hygrothermal loading causes the increase of the swelling of the membrane and to stiffness decrease [160,161,174,175,183,229].
  Multiple degradation mechanisms in the PEM could also occur due to perforations, cracks, tears or pinholes which can result from initial membrane defects or incorrect manufacturing processes of the membrane electrode assembly (MEA) or stacks, can lead to early failure of the assembly [56]. It is crucial to understand

their origins because the lifetime of the PEMFC is directly related to their occurrence.

- **MEA interfaces:** the stresses induced by the assembly process or operating condition can cause a disconnection between the different MEA layers. In many cases, a detachment between the MEA layers followed by crack propagation leading to fracture and causing a very weak structure, hence, understanding the resulting microstructure change and the interfaces mechanical properties has the potential to serve as an indicator for PEMFC life prediction and performances In fact, defects such as pinholes or tears can lead to rapid cell failure. It is thus crucial to maintain a good contact between the MEA layers to prevent the mechanical breach of its interfaces.

In summary, this state of the art highlights the importance of knowing in real time the mechanical state of the fuel cell to optimize its performance and durability. The correlation between the mechanical state, structural changes and properties in the different layers of the MEA or its interfaces is not established today, due to the lack of information or data and the complexity of the multiscale subject. For this reason, in the next chapters, we will try to provide information on:

a) the real mechanical behavior of different types of GDL, via a series of in-plane and out of plane mechanical tests (***Figure 23a***);
b) the MEA interfacial mechanical properties, and in particular on the interface created during the MEA assembly (CL/MPL) through a new friction method (***Figure 23b***);
c) the impact of material and interfaces properties on the mechanical response of PEM under hygro-thermal loading via the development of a numerical model (***Figure 23c***).

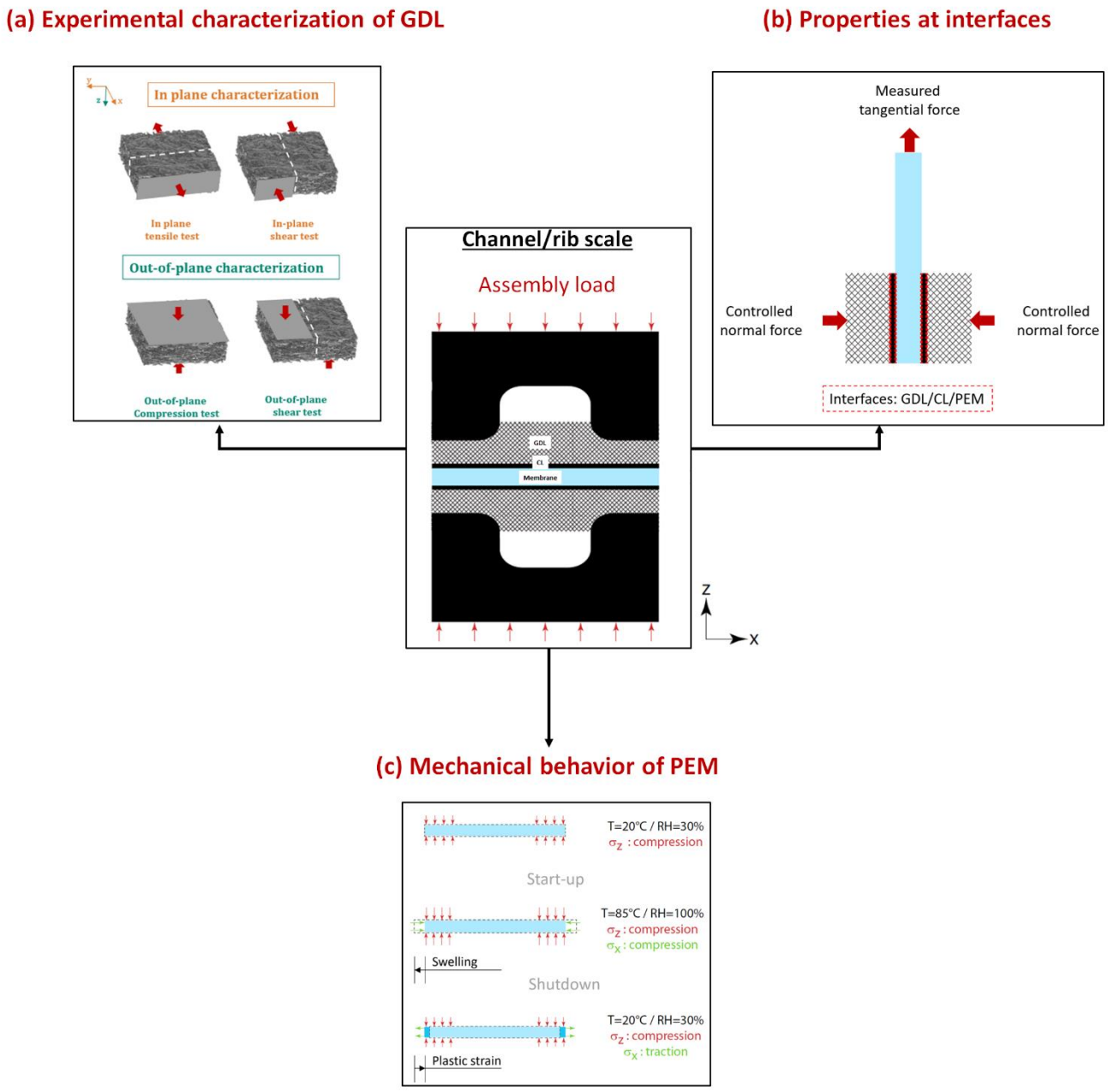

***Figure 23**: Summary diagram of the different works carried out during this doctoral study (a) experimental characterization of GDL; (b) study of the properties at MEA interfaces and (c) numerical analysis of the mechanical behavior of PEM.*

References

[1] Grove WR. The correlation of physical forces. Longmans, Green; 1874.
[2] Grove WR. XXIV. On voltaic series and the combination of gases by platinum. vol. 14, The London, Edinburgh, and Dublin Philosophical Magazine and Journal of Science; 1839, p. 127–30.
[3] F.R.S., W. G. E. M. LXXII. On a gaseous voltaic battery. vol. 21, The London, Edinburgh, and Dublin Philosophical Magazine and Journal of Science, Taylor & Francis,; 1842, p. 417–20.
[4] Space applications of hydrogen and fuel cells. National Aeronautics and Space Administration n.d. https://www.nasa.gov/topics/technology/hydrogen/hydrogen_2009.html.
[5] Spiegel C. Designing and building fuel cells. vol. 87. Citeseer; 2007.
[6] Larminie J, Dicks A. Fuel cell systems explained. 2nd ed. Chichester, West Sussex: J. Wiley; 2003.
[7] AMEDURI MB. Mise en évidence de la dégradation du liant ionomère des électrodes de pile à combustible. Université Lorraine, 2014.
[8] Wang H, Yuan X-Z, Li H. PEM fuel cell diagnostic tools. vol. 2. CRC press; 2011.
[9] Hart D. Sustainable energy conversion: fuel cells — the competitive option? 2000:5.
[10] Chalk SG, Miller JF, Wagner FW. Challenges for fuel cells in transport applications 2000:12.
[11] Carrette L, Friedrich KA, Stimming U. Fuel cells-fundamentals and applications. Fuel Cells 2001;1.
[12] Coors WG. Protonic ceramic fuel cells for high-efficiency operation with methane. Journal of Power Sources 2003;118:150–6. https://doi.org/10.1016/S0378-7753(03)00072-7.
[13] Yu X, Pickup PG. Recent advances in direct formic acid fuel cells (DFAFC). Journal of Power Sources 2008;182:124–32.
[14] Bagotsky VS. Fuel cells: problems and solutions. vol. 56. John Wiley & Sons; 2012.
[15] Kamarudin MZF, Kamarudin SK, Masdar MS, Daud WRW. Review: Direct ethanol fuel cells. International Journal of Hydrogen Energy 2013;38:9438–53. https://doi.org/10.1016/j.ijhydene.2012.07.059.
[16] Alaswad A, Palumbo A, Dassisti M, Abdelkareem MA, Olabi A-G. Fuel Cell Technologies, Applications, and State of the Art. A Reference Guide. Encyclopedia of Smart Materials, Elsevier; 2022, p. 315–33. https://doi.org/10.1016/B978-0-12-815732-9.00033-4.
[17] Dufour AU. Fuel cells – a new contributor to stationary power. Journal of Power Sources 1998:7.
[18] Wan Z, Chang H, Shu S, Wang Y, Tang H. A Review on Cold Start of Proton Exchange Membrane Fuel Cells. Energies 2014;7:3179–203. https://doi.org/10.3390/en7053179.
[19] Baxter J, Bian Z, Chen G, Danielson D, Dresselhaus MS, Fedorov AG, et al. Nanoscale design to enable the revolution in renewable energy. Energy Environ Sci 2009;2:559. https://doi.org/10.1039/b821698c.
[20] Blomen LJ, Mugerwa MN. Fuel cell systems. Springer Science & Business Media; 2013.
[21] Hydrogen - Analysis - International Energy Agency n.d. https://www.iea.org/reports/hydrogen.
[22] Dyer CK. Fuel cells for portable applications. Journal of Power Sources 2002:4.

[23] Tüber K, Zobel M, Schmidt H, Hebling C. A polymer electrolyte membrane fuel cell system for powering portable computers. Journal of Power Sources 2003;122:1–8. https://doi.org/10.1016/S0378-7753(03)00428-2.
[24] Wee J-H. Applications of proton exchange membrane fuel cell systems. Renewable and Sustainable Energy Reviews 2007;11:1720–38. https://doi.org/10.1016/j.rser.2006.01.005.
[25] Peighambardoust SJ, Rowshanzamir S, Amjadi M. Review of the proton exchange membranes for fuel cell applications. International Journal of Hydrogen Energy 2010;35:9349–84. https://doi.org/10.1016/j.ijhydene.2010.05.017.
[26] Carral C. Compréhension des relations entre l'état mécanique et le fonctionnement d'une pile à combustible de type PEMFC à l'aide d'une approche duale expérimentale et prédictive. PhD thesis, Université de Grenoble, 2014. n.d.
[27] Hermann A, Chaudhuri T, Spagnol P. Bipolar plates for PEM fuel cells: A review. International Journal of Hydrogen Energy 2005;30:1297–302. https://doi.org/10.1016/j.ijhydene.2005.04.016.
[28] Seguela MR, Lottin MO, Loubet MJ-L. Thèse soutenue publiquement le 8 décembre 2014, devant le jury composé de : n.d.:153.
[29] Li X, Sabir I. Review of bipolar plates in PEM fuel cells: Flow-field designs. International Journal of Hydrogen Energy 2005;30:359–71. https://doi.org/10.1016/j.ijhydene.2004.09.019.
[30] Mehta V, Cooper JS. Review and analysis of PEM fuel cell design and manufacturing. Journal of Power Sources 2003:22.
[31] Kuan H-C, Ma C-CM, Chen KH, Chen S-M. Preparation, electrical, mechanical and thermal properties of composite bipolar plate for a fuel cell. Journal of Power Sources 2004;134:7–17. https://doi.org/10.1016/j.jpowsour.2004.02.024.
[32] Yan X, Hou M, Zhang H, Jing F, Ming P, Yi B. Performance of PEMFC stack using expanded graphite bipolar plates. Journal of Power Sources 2006;160:252–7. https://doi.org/10.1016/j.jpowsour.2006.01.022.
[33] Tawfik H, Hung Y, Mahajan D. Metal bipolar plates for PEM fuel cell—A review. Journal of Power Sources 2007;163:755–67. https://doi.org/10.1016/j.jpowsour.2006.09.088.
[34] Wang H, Turner JA. Reviewing Metallic PEMFC Bipolar Plates. Fuel Cells 2010;10:510–9. https://doi.org/10.1002/fuce.200900187.
[35] Turan C. Contact resistance characteristics of coated metallic bipolar plates for PEM fuel cells e investigations on the effect of manufacturing. I n t e r n a t i o n a l j o u r n a l o f h y d r o g e n e n e r g y n.d.:18.
[36] Lee SH, Pukha VE, Vinogradov VE, Kakati N, Jee SH, Cho SB, et al. Nanocomposite-carbon coated at low-temperature: A new coating material for metallic bipolar plates of polymer electrolyte membrane fuel cells. I n t e r n a t i o n a l j o u r n a l o f h y d r o g e n e n e r g y n.d.:11.
[37] Madadi F, Rezaeian A, Edris H, Zhiani M. Improving performance in PEMFC by applying different coatings to metallic bipolar plates. Materials Chemistry and Physics 2019;238:121911. https://doi.org/10.1016/j.matchemphys.2019.121911.
[38] Xu Z, Qiu D, Yi P, Peng L, Lai X. Towards mass applications: A review on the challenges and developments in metallic bipolar plates for PEMFC. Progress in Natural Science: Materials International 2020;30:815–24. https://doi.org/10.1016/j.pnsc.2020.10.015.

[39] Hontanon E, Escudero MJ, Bautista C, Garcıa-Ybarra PL, Daza L. Optimisation of flow-field in polymer electrolyte membrane fuel cells using computational fluid dynamics techniques 2000:6.
[40] Cunningham BD, Huang J, Baird DG. Development of bipolar plates for fuel cells from graphite filled wet-lay material and a thermoplastic laminate skin layer. Journal of Power Sources 2007;165:764–73. https://doi.org/10.1016/j.jpowsour.2006.12.035.
[41] Pozio A, Silva RF, De Francesco M, Giorgi L. Nafion degradation in PEFCs from end plate iron contamination. Electrochimica Acta 2003;48:1543–9. https://doi.org/10.1016/S0013-4686(03)00026-4.
[42] Antunes RA, Oliveira MCL, Ett G, Ett V. Corrosion of metal bipolar plates for PEM fuel cells: A review. International Journal of Hydrogen Energy 2010;35:3632–47. https://doi.org/10.1016/j.ijhydene.2010.01.059.
[43] Wilberforce T, El Hassan Z, Ogungbemi E, Ijaodola O, Khatib FN, Durrant A, et al. A comprehensive study of the effect of bipolar plate (BP) geometry design on the performance of proton exchange membrane (PEM) fuel cells. Renewable and Sustainable Energy Reviews 2019;111:236–60. https://doi.org/10.1016/j.rser.2019.04.081.
[44] Mathias M, Roth J, Fleming J, Lehnert W. Diffusion media materials and characterisation. Handbook of Fuel Cells—Fundamentals, Technology and Applications 2003;3:517–37.
[45] Li H, Tang Y, Wang Z, Shi Z, Wu S, Song D, et al. A review of water flooding issues in the proton exchange membrane fuel cell. Journal of Power Sources 2008;178:103–17.
[46] Rofaiel A, Ellis JS, Challa PR, Bazylak A. Heterogeneous through-plane distributions of polytetrafluoroethylene in polymer electrolyte membrane fuel cell gas diffusion layers. Journal of Power Sources 2012;201:219–25. https://doi.org/10.1016/j.jpowsour.2011.11.005.
[47] El-kharouf A, Pollet BG. Gas Diffusion Media and their Degradation. Polymer Electrolyte Fuel Cell Degradation, Elsevier; 2012, p. 215–47. https://doi.org/10.1016/B978-0-12-386936-4.10004-1.
[48] Omrani R, Shabani B. Review of gas diffusion layer for proton exchange membrane-based technologies with a focus on unitised regenerative fuel cells. International Journal of Hydrogen Energy 2019;44:3834–60. https://doi.org/10.1016/j.ijhydene.2018.12.120.
[49] Ralph TR, Hards GA, Keating JE, Campbell SA, Wilkinson DP, Davis M, et al. Low Cost Electrodes for Proton Exchange Membrane Fuel Cells: Performance in Single Cells and Ballard Stacks. The Electrochemical Society 1997;144:3845–57. https://doi.org/10.1149/1.1838101.
[50] Frey Th, Linardi M. Effects of membrane electrode assembly preparation on the polymer electrolyte membrane fuel cell performance. Electrochimica Acta 2004;50:99–105. https://doi.org/10.1016/j.electacta.2004.07.017.
[51] Sasabe T, Deevanhxay P, Tsushima S, Hirai S. Investigation on the effect of microstructure of proton exchange membrane fuel cell porous layers on liquid water behavior by soft X-ray radiography. Journal of Power Sources 2011;196:8197–206. https://doi.org/10.1016/j.jpowsour.2011.05.045.
[52] Wang Y, Wang C-Y, Chen KS. Elucidating differences between carbon paper and carbon cloth in polymer electrolyte fuel cells. Electrochimica Acta 2007;52:3965–75. https://doi.org/10.1016/j.electacta.2006.11.012.

[53] Stampino PG, Omati L, Dotelli G. Electrical Performance of PEM Fuel Cells With Different Gas Diffusion Layers. Journal of Fuel Cell Science and Technology 2011;8:041005. https://doi.org/10.1115/1.4003630.
[54] Kowal JJ, Turhan A, Heller K, Brenizer J, Mench MM. Liquid Water Storage, Distribution, and Removal from Diffusion Media in PEFCS. J Electrochem Soc 2006;153:A1971. https://doi.org/10.1149/1.2258049.
[55] Schweiss R, Meiser C, Damjanovic T, Galbiati I, Haak N. SIGRACET® Gas Diffusion Layers for PEM Fuel Cells, Electrolyzers and Batteries n.d.:10.
[56] Zhang J, Zhang H, Wu J, Zhang J. Fuel Cell Degradation and Failure Analysis. Pem Fuel Cell Testing and Diagnosis, Elsevier; 2013, p. 283–335. https://doi.org/10.1016/B978-0-444-53688-4.00011-5.
[57] Lin G, Van Nguyen T. Effect of thickness and hydrophobic polymer content of the gas diffusion layer on electrode flooding level in a PEMFC. Journal of the Electrochemical Society 2005;152:A1942.
[58] Park G-G, Sohn Y-J, Yang T-H, Yoon Y-G, Lee W-Y, Kim C-S. Effect of PTFE contents in the gas diffusion media on the performance of PEMFC. Journal of Power Sources 2004;131:182–7.
[59] Chun JH, Park KT, Jo DH, Kim SG, Kim SH. Numerical modeling and experimental study of the influence of GDL properties on performance in a PEMFC. International Journal of Hydrogen Energy 2011;36:1837–45.
[60] Velayutham G, Kaushik J, Rajalakshmi N, Dhathathreyan K. Effect of PTFE content in gas diffusion media and microlayer on the performance of PEMFC tested under ambient pressure. Fuel Cells 2007;7:314–8.
[61] Kumar RJF, Radhakrishnan V, Haridoss P. Enhanced mechanical and electrochemical durability of multistage PTFE treated gas diffusion layers for proton exchange membrane fuel cells. International Journal of Hydrogen Energy 2012;37:10830–5.
[62] Jia J, Liu X, Liu F, Yin H, Ding Y. Designing independent water transport channels to improve water flooding in ultra-thin nanoporous film cathodes for PEMFCs. International Journal of Hydrogen Energy 2022;47:21261–72. https://doi.org/10.1016/j.ijhydene.2022.04.243.
[63] Blanco M, Wilkinson DP. Investigation of the effect of microporous layers on water management in a proton exchange membrane fuel cell using novel diagnostic methods. International Journal of Hydrogen Energy 2014;39:16390–404. https://doi.org/10.1016/j.ijhydene.2014.07.147.
[64] Morgan JM, Datta R. Understanding the gas diffusion layer in proton exchange membrane fuel cells. I. How its structural characteristics affect diffusion and performance. Journal of Power Sources 2014;251:269–78.
[65] Nam JH, Lee K-J, Hwang G-S, Kim C-J, Kaviany M. Microporous layer for water morphology control in PEMFC. International Journal of Heat and Mass Transfer 2009;52:2779–91. https://doi.org/10.1016/j.ijheatmasstransfer.2009.01.002.
[66] Zhang J, Wang B, Jin J, Yang S, Li G. A review of the microporous layer in proton exchange membrane fuel cells: Materials and structural designs based on water transport mechanism. Renewable and Sustainable Energy Reviews 2022;156:111998.
[67] Mauritz KA, Moore RB. State of Understanding of Nafion. Chem Rev 2004;104:4535–86. https://doi.org/10.1021/cr0207123.

[68] Khattra NS, Lu Z, Karlsson AM, Santare MH, Busby FC, Schmiedel T. Time-dependent mechanical response of a composite PFSA membrane. Journal of Power Sources 2013;228:256–69. https://doi.org/10.1016/j.jpowsour.2012.11.116.
[69] DuPont, Product Information: Nafion PFSA Membranes N-112, NE-1135, N-115, N-117, NE-1110 Perfluorosulfonic Acid Polymer, NAE101, 2004. n.d.
[70] Smith RA, Square K, Withers MS. (54) COEXTRUDED MULTLAYER CATION EXCHANGE MEMBRANES n.d.:7.
[71] Prelschl C. Hedrich, Mariabrunn; Alfred Hahn, Oer-ErkenschWick, all of (DE) n.d.:7.
[72] Santalone J. Primary Examiner—Stephen J. Kalafut (74) Attorney, Agent, or Firm—KaloW & Springut LLP; n.d.:10.
[73] Curtin DE, Lousenberg RD, Henry TJ, Tangeman PC, Tisack ME. Advanced materials for improved PEMFC performance and life. Journal of Power Sources 2004;131:41–8. https://doi.org/10.1016/j.jpowsour.2004.01.023.
[74] Morris DR, Sun X. Water-sorption and transport properties of Nafion 117 H. J Appl Polym Sci 1993;50:1445–52. https://doi.org/10.1002/app.1993.070500816.
[75] Rikukawa M, Sanui K. Proton-conducting polymer electrolyte membranes based on hydrocarbon polymers. Prog Polym Sci 2000:40.
[76] Tang Y, Kusoglu A, Karlsson AM, Santare MH, Cleghorn S, Johnson WB. Mechanical properties of a reinforced composite polymer electrolyte membrane and its simulated performance in PEM fuel cells. Journal of Power Sources 2008;175:817–25. https://doi.org/10.1016/j.jpowsour.2007.09.093.
[77] Kolde JA, Bahar B, Wilson MS, Zawodzinski TA, Gottesfeld S. Advanced composite polymer electrolyte fuel cell membranes. ECS Proceedings Volumes 1995;1995:193.
[78] Penner RM, Martin CR. Ion Transporting Composite Membranes. I. Nafion Impregnated Gore-Tex. TEXAS A AND M UNIV COLLEGE STATION DEPT OF CHEMISTRY; 1985.
[79] Gottesfeld S, Halpert G, Landgrebe AR, Electrochemical Society, Electrochemical Society, Electrochemical Society, editors. Proceedings of the First International Symposium on Proton Conducting Membrane Fuel Cells I. Pennington, NJ: Electrochemical Society; 1995.
[80] Liu W, Ruth K, Rusch G. Membrane durability in PEM fuel cells. Journal of New Materials for Electrochemical Systems 2001;4.
[81] Costamagna P, Srinivasan S. Quantum jumps in the PEMFC science and technology from the 1960s to the year 2000: Part II. Engineering, technology development and application aspects. Journal of Power Sources 2001;102:253–69.
[82] Vielstich W, Lamm A, Gasteiger H. Handbook of fuel cells. Fundamentals, technology, applications 2003.
[83] Liu D, Case S. Durability study of proton exchange membrane fuel cells under dynamic testing conditions with cyclic current profile. Journal of Power Sources 2006;162:521–31.
[84] Collier A, Wang H, Yuan XZ, Zhang J, Wilkinson DP. Degradation of polymer electrolyte membranes. International Journal of Hydrogen Energy 2006;31:1838–54.
[85] Ralph TR, Barnwell DE, Bouwman PJ, Hodgkinson AJ, Petch MI, Pollington M. Reinforced membrane durability in proton exchange membrane fuel cell stacks for automotive applications. Journal of The Electrochemical Society 2008;155:B411.
[86] Moukheiber E, Bas C, Flandin L. Understanding the formation of pinholes in PFSA membranes with the essential work of fracture (EWF). International Journal of

Hydrogen Energy 2014;39:2717–23. https://doi.org/10.1016/j.ijhydene.2013.03.031.
[87] Borup R, Meyers J, Pivovar B, Kim YS, Mukundan R, Garland N, et al. Scientific Aspects of Polymer Electrolyte Fuel Cell Durability and Degradation. Chem Rev 2007;107:3904–51. https://doi.org/10.1021/cr050182l.
[88] Dao DV, Adilbish G, Le TD, Lee I-H, Yu Y-T. Triple phase boundary and power density enhancement in PEMFCs of a Pt/C electrode with double catalyst layers. RSC Adv 2019;9:15635–41. https://doi.org/10.1039/C9RA01741K.
[89] Fouzaï I, Gentil S, Bassetto VC, Silva WO, Maher R, Girault HH. Catalytic layer-membrane electrode assembly methods for optimum triple phase boundaries and fuel cell performances. J Mater Chem A 2021;9:11096–123. https://doi.org/10.1039/D0TA07470E.
[90] Gasteiger HA, Panels JE, Yan SG. Dependence of PEM fuel cell performance on catalyst loading. Journal of Power Sources 2004;127:162–71. https://doi.org/10.1016/j.jpowsour.2003.09.013.
[91] Wilson MS, Gottesfeld S. High Performance Catalyzed Membranes of Ultra-low Pt Loadings for Polymer Electrolyte Fuel Cells. J Electrochem Soc 1992;139:L28–30. https://doi.org/10.1149/1.2069277.
[92] Cheng X, Yi B, Han M, Zhang J, Qiao Y, Yu J. Investigation of platinum utilization and morphology in catalyst layer of polymer electrolyte fuel cells 1999:7.
[93] Passos RR, Paganin VA, Ticianelli EA. Studies of the performance of PEM fuel cell cathodes with the catalyst layer directly applied on Nafion membranes. Electrochimica Acta 2006;51:5239–45. https://doi.org/10.1016/j.electacta.2006.01.044.
[94] Strong A, Thornberry C, Beattie S, Chen R, Coles SR. Depositing Catalyst Layers in Polymer Electrolyte Membrane Fuel Cells: A Review. Journal of Fuel Cell Science and Technology 2015;12:064001. https://doi.org/10.1115/1.4031961.
[95] Srinivasan S, Ticianelli EA, Derouin CR, Redondo A. Advances in solid polymer electrolyte fuel cell technology with low platinum loading electrodes. Journal of Power Sources 1988;22:359–75. https://doi.org/10.1016/0378-7753(88)80030-2.
[96] Hsu C. An innovative process for PEMFC electrodes using the expansion of Nafion film. Journal of Power Sources 2003;115:268–73. https://doi.org/10.1016/S0378-7753(03)00005-3.
[97] Song SQ, Liang ZX, Zhou WJ, Sun GQ, Xin Q, Stergiopoulos V, et al. Direct methanol fuel cells: The effect of electrode fabrication procedure on MEAs structural properties and cell performance. Journal of Power Sources 2005;145:495–501. https://doi.org/10.1016/j.jpowsour.2005.02.069.
[98] Zhang J, Yin G, Wang Z, Shao Y. Effects of MEA preparation on the performance of a direct methanol fuel cell. Journal of Power Sources 2006;160:1035–40. https://doi.org/10.1016/j.jpowsour.2006.02.059.
[99] Tang H, Wang S, Pan M, Jiang SP, Ruan Y. Performance of direct methanol fuel cells prepared by hot-pressed MEA and catalyst-coated membrane (CCM). Electrochimica Acta 2007;52:3714–8. https://doi.org/10.1016/j.electacta.2006.10.053.
[100] Cho JH, Kim JM, Prabhuram J, Hwang SY, Ahn DJ, Ha HY, et al. Fabrication and evaluation of membrane electrode assemblies by low-temperature decal methods for direct methanol fuel cells. Journal of Power Sources 2009;187:378–86. https://doi.org/10.1016/j.jpowsour.2008.10.111.

[101] Rajalakshmi N, Dhathathreyan KS. Catalyst layer in PEMFC electrodes—Fabrication, characterisation and analysis. Chemical Engineering Journal 2007;129:31–40.
[102] Ihm JW, Ryu H, Bae JS, Choo WK, Choi DK. High performance of electrode with low Pt loading prepared by simplified direct screen printing process in PEM fuel cells. Journal of Materials Science 2004;39:4647–9.
[103] Bevers D, Wagner N, Von Bradke M. Innovative production procedure for low cost PEFC electrodes and electrode/membrane structures. International Journal of Hydrogen Energy 1998;23:57–63.
[104] Gülzow E, Schulze M, Wagner N, Kaz T, Reissner R, Steinhilber G, et al. Dry layer preparation and characterisation of polymer electrolyte fuel cell components. Journal of Power Sources 2000;86:352–62.
[105] Gülzow E, Kaz T. New results of PEFC electrodes produced by the DLR dry preparation technique. Journal of Power Sources 2002;106:122–5.
[106] Saab AP, Garzon FH, Zawodzinski TA. Determination of ionic and electronic resistivities in carbon/polyelectrolyte fuel-cell composite electrodes. Journal of The Electrochemical Society 2002;149:A1541.
[107] Bender G, Zawodzinski TA, Saab AP. Fabrication of high precision PEFC membrane electrode assemblies. Journal of Power Sources 2003;124:114–7.
[108] Saha MS, Paul D, Malevich D, Peppley B, Karan K. Preparation of ultra-thin catalyst layers by piezo-electric printer for PEMFCs applications. ECS Transactions 2009;25:2049.
[109] Yazdanpour M, Esmaeilifar A, Rowshanzamir S. Effects of hot pressing conditions on the performance of Nafion membranes coated by ink-jet printing of Pt/MWCNTs electrocatalyst for PEMFCs. International Journal of Hydrogen Energy 2012;37:11290–8.
[110] Malevich D, Saha MS, Halliop E, Peppley BA, Pharoah JG, Karan K. Performance characteristics of PEFCs with patterned electrodes prepared by piezo-electric printing. Ecs Transactions 2013;50:423.
[111] Haug AT, White RE, Weidner JW, Huang W, Shi S, Stoner T, et al. Increasing proton exchange membrane fuel cell catalyst effectiveness through sputter deposition. Journal of the Electrochemical Society 2002;149:A280.
[112] Brault P, Caillard A, Thomann AL, Mathias J, Charles C, Boswell RW, et al. Plasma sputtering deposition of platinum into porous fuel cell electrodes. Journal of Physics D: Applied Physics 2004;37:3419.
[113] Huang K-L, Lai Y-C, Tsai C-H. Effects of sputtering parameters on the performance of electrodes fabricated for proton exchange membrane fuel cells. Journal of Power Sources 2006;156:224–31.
[114] Cunningham N, Irissou E, Lefevre M, Denis M-C, Guay D, Dodelet J-P. PEMFC anode with very low Pt loadings using pulsed laser deposition. Electrochemical and Solid-State Letters 2003;6:A125.
[115] Kim H, Popov BN. Development of novel method for preparation of PEMFC electrodes. Electrochemical and Solid-State Letters 2004;7:A71.
[116] Martín AJ, Chaparro AM, Gallardo B, Folgado MA, Daza L. Characterization and single cell testing of Pt/C electrodes prepared by electrodeposition. Journal of Power Sources 2009;192:14–20.
[117] Baturina OA, Wnek GE. Characterization of proton exchange membrane fuel cells with catalyst layers obtained by electrospraying. Electrochemical and Solid-State Letters 2005;8:A267.

[118] Chaparro AM, Benítez R, Gubler L, Scherer GG, Daza L. Study of membrane electrode assemblies for PEMFC, with cathodes prepared by the electrospray method. Journal of Power Sources 2007;169:77–84.
[119] Martin S, Martinez-Vazquez B, Garcia-Ybarra PL, Castillo JL. Peak utilization of catalyst with ultra-low Pt loaded PEM fuel cell electrodes prepared by the electrospray method. Journal of Power Sources 2013;229:179–84.
[120] Zhang W, Brodt MW, Pintauro PN. Nanofiber cathodes for low and high humidity hydrogen fuel cell operation. ECS Transactions 2011;41:891.
[121] Zhang W, Pintauro PN. High-performance nanofiber fuel cell electrodes. ChemSusChem 2011;4:1753–7.
[122] Sightler JJ, McPherson E, Rigdon WA, Huang X. Application of Electrospinning Technique in the Fabrication of Catalyst Layer of Membrane Electrode Assemblies. ECS Transactions 2013;50:1445.
[123] Kannan AM, Veedu VP, Munukutla L, Ghasemi-Nejhad MN. Nanostructured gas diffusion and catalyst layers for proton exchange membrane fuel cells. Electrochemical and Solid-State Letters 2006;10:B47.
[124] Chen J, Lim B, Lee EP, Xia Y. Shape-controlled synthesis of platinum nanocrystals for catalytic and electrocatalytic applications. Nano Today 2009;4:81–95.
[125] Yoshino S, Shinohara A, Kodama K, Morimoto Y. Fabrication of catalyst layer with ionomer nanofiber scaffolding for polymer electrolyte fuel cells. Journal of Power Sources 2020;476:228584. https://doi.org/10.1016/j.jpowsour.2020.228584.
[126] Therdthianwong A, Manomayidthikarn P, Therdthianwong S. Investigation of membrane electrode assembly (MEA) hot-pressing parameters for proton exchange membrane fuel cell 2007:11.
[127] Okur O, İyigün Karadağ Ç, Boyacı San FG, Okumuş E, Behmenyar G. Optimization of parameters for hot-pressing manufacture of membrane electrode assembly for PEM (polymer electrolyte membrane fuel cells) fuel cell. Energy 2013;57:574–80. https://doi.org/10.1016/j.energy.2013.05.001.
[128] Wei Z, Wang S, Yi B, Liu J, Chen L, Zhou W, et al. Influence of electrode structure on the performance of a direct methanol fuel cell. Journal of Power Sources 2002;106:364–9. https://doi.org/10.1016/S0378-7753(01)01023-0.
[129] Kong CS, Kim D-Y, Lee H-K, Shul Y-G, Lee T-H. In¯uence of pore-size distribution of diffusion layer on mass-transport problems of proton exchange membrane fuel cells. Journal of Power Sources 2002:7.
[130] Najafi Roudbari M, Ojani R, Raoof JB. Investigation of hot pressing parameters for manufacture of catalyst-coated membrane electrode (CCME) for polymer electrolyte membrane fuel cells by response surface method. Energy 2017;140:794–803. https://doi.org/10.1016/j.energy.2017.08.049.
[131] Koraishy B, Meyers JP, Wood KL. Manufacturing of membrane electrode assemblies for fuel cells n.d.:13.
[132] Ramani D, Khattra NS, Singh Y, Orfino FP, Dutta M, Kjeang E. Mitigation of mechanical membrane degradation in fuel cells – Part 2: Bonded membrane electrode assembly. Journal of Power Sources 2021;512:230431. https://doi.org/10.1016/j.jpowsour.2021.230431.
[133] Kleemann J, Finsterwalder F, Tillmetz W. Characterisation of mechanical behaviour and coupled electrical properties of polymer electrolyte membrane fuel cell gas diffusion layers. Journal of Power Sources 2009;190:92–102. https://doi.org/10.1016/j.jpowsour.2008.09.026.
[134] FuelCellsEtc. n.d. https://fuelcellsetc.com/.

[135] D1184-98, Standard Test Method for Flexural Strength of Adhesive Bonded Laminated Assemblies, ASTM International, West Conshohocken, PA, 2004. n.d.
[136] Mathur RB, Maheshwari PH, Dhami TL, Sharma RK, Sharma CP. Processing of carbon composite paper as electrode for fuel cell. Journal of Power Sources 2006;161:790–8. https://doi.org/10.1016/j.jpowsour.2006.05.053.
[137] Mathur RB, Maheshwari PH, Dhami TL, Tandon RP. Characteristics of the carbon paper heat-treated to different temperatures and its influence on the performance of PEM fuel cell. Electrochimica Acta 2007;52:4809–17. https://doi.org/10.1016/j.electacta.2007.01.041.
[138] CeTech - Carbon Paper: Sheet type, 2007. n.d. http://www.ce-tech.com.tw/english/GDL-03.html.
[139] Arvay A, Yli-Rantala E, Liu C-H, Peng X-H, Koski P, Cindrella L, et al. Characterization techniques for gas diffusion layers for proton exchange membrane fuel cells – A review. Journal of Power Sources 2012;213:317–37. https://doi.org/10.1016/j.jpowsour.2012.04.026.
[140] Han K, Hong BK, Kim SH, Ahn BK, Lim TW. Influence of anisotropic bending stiffness of gas diffusion layers on the electrochemical performances of polymer electrolyte membrane fuel cells. International Journal of Hydrogen Energy 2010;35:12317–28. https://doi.org/10.1016/j.ijhydene.2010.08.061.
[141] Poornesh K, Cho C, Rego A. Anisotropic distribution of elastic constants in fuel cell gas diffusion layers: Experimental validation. Energy and Power 2015;5:40–5.
[142] Poornesh K, Vaz N, Rego A. Anisotropic Distribution of Elastic Constants in Fuel Cell Gas Diffusion Layers: Theoretical Assessment 2015;5:34–9. https://doi.org/10.5923/c.ep.201501.07.
[143] DIN 53121, Prüfung von Papier, Karton und Pappe - Bestimmung der Biegesteifigkeit nach der Balkenmethode, Deutsches Institut für Normung, Berlin, 1987. n.d.
[144] EN 13706-2, Reinforced plastics composites – Specification for Pultruded Profiles – Part 2:Methods of Test and General Requirements, European Committee for Standardization, Bruxels, 2002. n.d.
[145] Chen Y, Jiang C, Cho C. An experimental investigation of three-dimensional mechanical characteristics of gas diffusion layers in proton electrolyte membrane fuel cells. J Solid State Electrochem 2019;23:2021–30. https://doi.org/10.1007/s10008-019-04273-x.
[146] ASTM D638 (2010) Standard test method for tensile properties of plastics. ASTM International, West Conshohocken. https://doi.org/ 10.1520/D0638-10 n.d.
[147] Lai Y-H, Rapaport PA, Ji C, Kumar V. Channel intrusion of gas diffusion media and the effect on fuel cell performance. Journal of Power Sources 2008;184:120–8. https://doi.org/10.1016/j.jpowsour.2007.12.065.
[148] Mishra V, Yang F, Pitchumani R. Measurement and prediction of electrical contact resistance between gas diffusion layers and bipolar plate for applications to PEM fuel cells 2004.
[149] Escribano S, Blachot J-F, Ethève J, Morin A, Mosdale R. Characterization of PEMFCs gas diffusion layers properties. Journal of Power Sources 2006;156:8–13. https://doi.org/10.1016/j.jpowsour.2005.08.013.
[150] Radhakrishnan V, Haridoss P. Effect of cyclic compression on structure and properties of a Gas Diffusion Layer used in PEM fuel cells. International Journal of Hydrogen Energy 2010;35:11107–18. https://doi.org/10.1016/j.ijhydene.2010.07.009.

[151] Gigos PA, Faydi Y, Meyer Y. Mechanical characterization and analytical modeling of gas diffusion layers under cyclic compression. International Journal of Hydrogen Energy 2015;40:5958–65.
[152] El Oualid S, Lachat R, Candusso D, Meyer Y. Characterization process to measure the electrical contact resistance of Gas Diffusion Layers under mechanical static compressive loads. International Journal of Hydrogen Energy 2017;42:23920–31.
[153] Mason TJ, Millichamp J, Neville TP, El-kharouf A, Pollet BG, Brett DJL. Effect of clamping pressure on ohmic resistance and compression of gas diffusion layers for polymer electrolyte fuel cells. Journal of Power Sources 2012;219:52–9. https://doi.org/10.1016/j.jpowsour.2012.07.021.
[154] Radhakrishnan V, Haridoss P. Differences in structure and property of carbon paper and carbon cloth diffusion media and their impact on proton exchange membrane fuel cell flow field design. Materials & Design 2011;32:861–8. https://doi.org/10.1016/j.matdes.2010.07.009.
[155] Nitta I, Hottinen T, Himanen O, Mikkola M. Inhomogeneous compression of PEMFC gas diffusion layer Part I. Experimental. Journal of Power Sources 2007:11.
[156] Ismail MS, Hassanpour A, Ingham DB, Ma L, Pourkashanian M. On the Compressibility of Gas Diffusion Layers in Proton Exchange Membrane Fuel Cells. Fuel Cells 2012;12:391–7. https://doi.org/10.1002/fuce.201100054.
[157] Koorata PK, Bhat SD. Compressive cyclic response of PEM fuel cell gas diffusion media. International Journal of Hydrogen Energy 2021;46:5570–9. https://doi.org/10.1016/j.ijhydene.2020.11.023.
[158] Sadeghifar H, Djilali N, Bahrami M. Effect of Polytetrafluoroethylene (PTFE) and micro porous layer (MPL) on thermal conductivity of fuel cell gas diffusion layers: Modeling and experiments. Journal of Power Sources 2014;248:632–41. https://doi.org/10.1016/j.jpowsour.2013.09.136.
[159] Lee T, Yang C. A parametric study on the deformation of gas diffusion layer in PEM fuel cell. J Mech Sci Technol 2020;34:259–68. https://doi.org/10.1007/s12206-019-1227-8.
[160] Kusoglu A, Karlsson AM, Santare MH, Cleghorn S, Johnson WB. Mechanical response of fuel cell membranes subjected to a hygro-thermal cycle. Journal of Power Sources 2006;161:987–96. https://doi.org/10.1016/j.jpowsour.2006.05.020.
[161] Kusoglu A, Karlsson AM, Santare MH, Cleghorn S, Johnson WB. Mechanical behavior of fuel cell membranes under humidity cycles and effect of swelling anisotropy on the fatigue stresses. Journal of Power Sources 2007;170:345–58. https://doi.org/10.1016/j.jpowsour.2007.03.063.
[162] Kandlikar SG, Lu Z, Lin TY, Cooke D, Daino M. Uneven gas diffusion layer intrusion in gas channel arrays of proton exchange membrane fuel cell and its effects on flow distribution. Journal of Power Sources 2009;194:328–37. https://doi.org/10.1016/j.jpowsour.2009.05.019.
[163] Taymaz I, Benli M. Numerical study of assembly pressure effect on the performance of proton exchange membrane fuel cell. Energy 2010;35:2134–40. https://doi.org/10.1016/j.energy.2010.01.032.
[164] Zhou P, Wu CW, Ma GJ. Contact resistance prediction and structure optimization of bipolar plates. Journal of Power Sources 2006;159:1115–22. https://doi.org/10.1016/j.jpowsour.2005.12.080.
[165] Lai X, Liu D, Peng L, Ni J. A mechanical–electrical finite element method model for predicting contact resistance between bipolar plate and gas diffusion layer in PEM

fuel cells. Journal of Power Sources 2008;182:153–9. https://doi.org/10.1016/j.jpowsour.2008.03.069.
[166] Bograchev D, Gueguen M, Grandidier J-C, Martemianov S. Stress and plastic deformation of MEA in fuel cells. Journal of Power Sources 2008;180:393–401. https://doi.org/10.1016/j.jpowsour.2008.02.048.
[167] Liu D, Peng L, Lai X. Effect of dimensional error of metallic bipolar plate on the GDL pressure distribution in the PEM fuel cell. International Journal of Hydrogen Energy 2009;34:990–7. https://doi.org/10.1016/j.ijhydene.2008.10.081.
[168] Qiu D, Yi P, Peng L, Lai X. Assembly design of proton exchange membrane fuel cell stack with stamped metallic bipolar plates. International Journal of Hydrogen Energy 2015;40:11559–68. https://doi.org/10.1016/j.ijhydene.2015.03.064.
[169] García-Salaberri PA, Vera M, Zaera R. Nonlinear orthotropic model of the inhomogeneous assembly compression of PEM fuel cell gas diffusion layers. International Journal of Hydrogen Energy 2011;36:11856–70. https://doi.org/10.1016/j.ijhydene.2011.05.152.
[170] Serincan MF, Pasaogullari U. Effect of gas diffusion layer anisotropy on mechanical stresses in a polymer electrolyte membrane. Journal of Power Sources 2011;196:1314–20. https://doi.org/10.1016/j.jpowsour.2010.06.026.
[171] Firat E, Beckhaus P, Heinzel A. Finite Element Approach for the Analysis of the Fuel Cell Internal Stress Distribution n.d.:7.
[172] Yi P, Peng L, Lai X, Ni J. A Numerical Model for Predicting Gas Diffusion Layer Failure in Proton Exchange Membrane Fuel Cells. Journal of Fuel Cell Science and Technology 2011;8:011011. https://doi.org/10.1115/1.4002312.
[173] Leng Y, Yao H, Yang D, Li B, Ming P, Zhang C. The influences of gas diffusion layer material models and parameters on mechanical analysis of proton exchange membrane fuel cell. Fuel Cells 2021;21:373–89. https://doi.org/10.1002/fuce.202100068.
[174] Tang Y, Santare MH, Karlsson AM, Cleghorn S, Johnson WB. Stresses in proton exchange membranes due to hygro-thermal loading 2006. https://doi.org/10.1115/1.2173666.
[175] Kawano Y, Wang Y, Palmer RA, Aubuchon SR. Stress-strain curves of Nafion membranes in acid and salt forms. Polímeros 2002;12:96–101.
[176] Solasi R, Zou Y, Huang X, Reifsnider K, Condit D. On mechanical behavior and in-plane modeling of constrained PEM fuel cell membranes subjected to hydration and temperature cycles. Journal of Power Sources 2007;167:366–77. https://doi.org/10.1016/j.jpowsour.2007.02.025.
[177] Majsztrik PW, Bocarsly AB, Benziger JB. Viscoelastic Response of Nafion. Effects of Temperature and Hydration on Tensile Creep. Macromolecules 2008;41:9849–62. https://doi.org/10.1021/ma801811m.
[178] Kusoglu A, Santare MH, Karlsson AM. Mechanics-based model for non-affine swelling in perfluorosulfonic acid (PFSA) membranes. Polymer 2009;50:2481–91. https://doi.org/10.1016/j.polymer.2009.03.045.
[179] Kusoglu A, Tang Y, Lugo M, Karlsson AM, Santare MH, Cleghorn S, et al. Constitutive response and mechanical properties of PFSA membranes in liquid water. Journal of Power Sources 2010;195:483–92. https://doi.org/10.1016/j.jpowsour.2009.08.010.
[180] Kusoglu A, Weber AZ. New Insights into Perfluorinated Sulfonic-Acid Ionomers. Chem Rev 2017;117:987–1104. https://doi.org/10.1021/acs.chemrev.6b00159.

[181] Satterfield MB, Majsztrik PW, Ota H, Benziger JB, Bocarsly AB. Mechanical properties of Nafion and titania/Nafion composite membranes for polymer electrolyte membrane fuel cells. J Polym Sci B Polym Phys 2006;44:2327–45. https://doi.org/10.1002/polb.20857.
[182] Bauer F, Denneler S, Willert-Porada M. Influence of temperature and humidity on the mechanical properties of Nafion® 117 polymer electrolyte membrane: Mechanical Properties of Nafion® 117. J Polym Sci B Polym Phys 2005;43:786–95. https://doi.org/10.1002/polb.20367.
[183] Satterfield MB, Benziger JB. Viscoelastic properties of Nafion at elevated temperature and humidity: Stress Relaxation of Nafion. J Polym Sci B Polym Phys 2009;47:11–24. https://doi.org/10.1002/polb.21608.
[184] Jia R, Dong S, Hasegawa T, Ye J, Dauskardt RH. Contamination and moisture absorption effects on the mechanical properties of catalyst coated membranes in PEM fuel cells. International Journal of Hydrogen Energy 2012;37:6790–7. https://doi.org/10.1016/j.ijhydene.2012.01.063.
[185] Byun S, Yu J-H, Choi J, Yun S, Roh Y, Dzakpasu CB, et al. Unraveling the cohesive and interfacial adhesive strengths of electrodes for automotive fuel cells. Journal of Power Sources 2020;455:227928. https://doi.org/10.1016/j.jpowsour.2020.227928.
[186] Ma S, Solterbeck C-H, Odgaard M, Skou E. Microscopy studies on pronton exchange membrane fuel cell electrodes with different ionomer contents. Appl Phys A 2009;96:581–9. https://doi.org/10.1007/s00339-008-5050-9.
[187] De Moor G, Bas C, Lesage F, Danérol AS, Claude E, Rossinot E, et al. Understanding the degradation of MEA in PEMFC: Definition of structural markers and comparison between laboratory and on-site ageing. J Appl Polym Sci 2011;120:3501–10. https://doi.org/10.1002/app.33506.
[188] Uchiyama T, Kumei H, Yoshida T, Ishihara K. Static friction force between catalyst layer and micro porous layer and its effect on deformations of membrane electrode assemblies under swelling. Journal of Power Sources 2014;272:522–30.
[189] Al-Baghdadi MAS. A CFD study of hygro–thermal stresses distribution in PEM fuel cell during regular cell operation. Renewable Energy 2009;34:674–82.
[190] Bajpai H, Khandelwal M, Kumbur EC, Mench MM. A computational model for assessing impact of interfacial morphology on polymer electrolyte fuel cell performance. Journal of Power Sources 2010;195:4196–205. https://doi.org/10.1016/j.jpowsour.2009.12.121.
[191] Zenyuk IV. Deterministic contact mechanics model applied to electrode interfaces in polymer electrolyte fuel cells and interfacial water accumulation. Journal of Power Sources 2013:9.
[192] Sadeghi E, Djilali N, Bahrami M. Effective thermal conductivity and thermal contact resistance of gas diffusion layers in proton exchange membrane fuel cells. Part 1: Effect of compressive load. Journal of Power Sources 2011;196:246–54. https://doi.org/10.1016/j.jpowsour.2010.06.039.
[193] Irmscher P, Qui D, Janßen H, Lehnert W, Stolten D. Impact of gas diffusion layer mechanics on PEM fuel cell performance. International Journal of Hydrogen Energy 2019;44:23406–15. https://doi.org/10.1016/j.ijhydene.2019.07.047.
[194] Zhang J, Hu Y. Sealing performance and mechanical behavior of PEMFCs sealing system based on thermodynamic coupling. International Journal of Hydrogen Energy 2020;45:23480–9. https://doi.org/10.1016/j.ijhydene.2020.06.167.

[195] Shi Q, Feng C, Ming P, Tang F, Zhang C. Compressive stress and its impact on the gas diffusion layer: A review. International Journal of Hydrogen Energy 2022.
[196] Senthil Velan V, Velayutham G, Rajalakshmi N, Dhathathreyan KS. Influence of compressive stress on the pore structure of carbon cloth based gas diffusion layer investigated by capillary flow porometry. International Journal of Hydrogen Energy 2014;39:1752–9. https://doi.org/10.1016/j.ijhydene.2013.11.038.
[197] Khetabi EM, Bouziane K, Zamel N, François X, Meyer Y, Candusso D. Effects of mechanical compression on the performance of polymer electrolyte fuel cells and analysis through in-situ characterisation techniques - A review. Journal of Power Sources 2019;424:8–26. https://doi.org/10.1016/j.jpowsour.2019.03.071.
[198] Toghyani S, Moradi Nafchi F, Afshari E, Hasanpour K, Baniasadi E, Atyabi SA. Thermal and electrochemical performance analysis of a proton exchange membrane fuel cell under assembly pressure on gas diffusion layer. International Journal of Hydrogen Energy 2018;43:4534–45. https://doi.org/10.1016/j.ijhydene.2018.01.068.
[199] Zhou P, Wu CW, Ma GJ. Influence of clamping force on the performance of PEMFCs. Journal of Power Sources 2007;163:874–81. https://doi.org/10.1016/j.jpowsour.2006.09.068.
[200] Wilde PM, Mändle M, Murata M, Berg N. Structural and Physical Properties of GDL and GDL/BPP Combinations and their Influence on PEMFC Performance. Fuel Cells 2004;4:180–4. https://doi.org/10.1002/fuce.200400022.
[201] Wu J, Martin JJ, Orfino FP, Wang H, Legzdins C, Yuan X-Z, et al. In situ accelerated degradation of gas diffusion layer in proton exchange membrane fuel cell: Part I: Effect of elevated temperature and flow rate. Journal of Power Sources 2010;195:1888–94.
[202] Stevens DA, Dahn JR. Thermal degradation of the support in carbon-supported platinum electrocatalysts for PEM fuel cells. Carbon 2005;43:179–88.
[203] Cai M, Ruthkosky MS, Merzougui B, Swathirajan S, Balogh MP, Oh SH. Investigation of thermal and electrochemical degradation of fuel cell catalysts. Journal of Power Sources 2006;160:977–86.
[204] Schulze M, Christenn C. XPS investigation of the PTFE induced hydrophobic properties of electrodes for low temperature fuel cells. Applied Surface Science 2005;252:148–53.
[205] Lee C, Mérida W. Gas diffusion layer durability under steady-state and freezing conditions. Journal of Power Sources 2007;164:141–53. https://doi.org/10.1016/j.jpowsour.2006.09.092.
[206] Weber AZ, Newman J. A theoretical study of membrane constraint in polymer-electrolyte fuel cells. AIChE J 2004;50:3215–26. https://doi.org/10.1002/aic.10230.
[207] Lai YH, Dillard DA. Mechanical durability characterization and modeling of ionomeric membranes. Handbook of Fuel Cells 2010.
[208] Qiu D, Peng L, Liang P, Yi P, Lai X. Mechanical degradation of proton exchange membrane along the MEA frame in proton exchange membrane fuel cells. Energy 2018;165:210–22. https://doi.org/10.1016/j.energy.2018.09.136.
[209] Kim S, Ahn BK, Mench MM. Physical degradation of membrane electrode assemblies undergoing freeze/thaw cycling: Diffusion media effects. Journal of Power Sources 2008;179:140–6. https://doi.org/10.1016/j.jpowsour.2007.12.114.
[210] Hiramitsu Y, Mitsuzawa N, Okada K, Hori M. Effects of ionomer content and oxygen permeation of the catalyst layer on proton exchange membrane fuel cell cold

start-up. Journal of Power Sources 2010;195:1038–45. https://doi.org/10.1016/j.jpowsour.2009.08.016.
[211] Alavijeh AS, Khorasany RMH, Nunn Z, Habisch A, Lauritzen M, Rogers E, et al. Microstructural and Mechanical Characterization of Catalyst Coated Membranes Subjected to In Situ Hygrothermal Fatigue. J Electrochem Soc 2015;162:F1461–9. https://doi.org/10.1149/2.0471514jes.
[212] Li L, Wang S, Yue L, Wang G. Cold-start icing characteristics of proton-exchange membrane fuel cells. International Journal of Hydrogen Energy 2019;44:12033–42. https://doi.org/10.1016/j.ijhydene.2019.03.115.
[213] Yan X, Hou M, Sun L, Cheng H, Hong Y, Liang D, et al. The study on transient characteristic of proton exchange membrane fuel cell stack during dynamic loading. Journal of Power Sources 2007;163:966–70. https://doi.org/10.1016/j.jpowsour.2006.09.075.
[214] Hinds G. G. Hinds, Performance and Durability of PEM Fuel Cells: A Review, Dr. M.G. Gee, Knowledge Leader, NPL Report DEPC-MPE 002, 2004. n.d.
[215] de la Cruz J, Cano U, Romero T. Simulation and in situ measurement of stress distribution in a polymer electrolyte membrane fuel cell stack. Journal of Power Sources 2016;329:273–80. https://doi.org/10.1016/j.jpowsour.2016.08.073.
[216] Lim S-J, Park G-G, Park J-S, Sohn Y-J, Yim S-D, Yang T-H, et al. Investigation of freeze/thaw durability in polymer electrolyte fuel cells. International Journal of Hydrogen Energy 2010;35:13111–7. https://doi.org/10.1016/j.ijhydene.2010.04.079.
[217] Huang X, Solasi R, Zou Y, Feshler M, Reifsnider K, Condit D, et al. Mechanical endurance of polymer electrolyte membrane and PEM fuel cell durability. J Polym Sci B Polym Phys 2006;44:2346–57. https://doi.org/10.1002/polb.20863.
[218] Malekian A, Salari S, Tam M, Djilali N, Bahrami M. Compressive behaviour of thin catalyst layers. Part II - Model development and validation. International Journal of Hydrogen Energy 2019;44:18461–71. https://doi.org/10.1016/j.ijhydene.2019.04.135.
[219] Guilminot E, Corcella A, Chatenet M, Maillard F. Comparing the thin-film rotating disk electrode and the ultramicroelectrode with cavity techniques to study carbon-supported platinum for proton exchange membrane fuel cell applications. Journal of Electroanalytical Chemistry 2007;599:111–20. https://doi.org/10.1016/j.jelechem.2006.09.022.
[220] Yan Q, Toghiani H, Lee Y-W, Liang K, Causey H. Effect of sub-freezing temperatures on a PEM fuel cell performance, startup and fuel cell components. Journal of Power Sources 2006;160:1242–50. https://doi.org/10.1016/j.jpowsour.2006.02.075.
[221] Singh Y, Khorasany RMH, Sadeghi Alavijeh A, Kjeang E, Wang GG, Rajapakse RKND. Ex situ measurement and modelling of crack propagation in fuel cell membranes under mechanical fatigue loading. International Journal of Hydrogen Energy 2017;42:19257–71. https://doi.org/10.1016/j.ijhydene.2017.06.151.
[222] Singh Y, Khorasany RMH, Kim WHJ, Alavijeh AS, Kjeang E, Rajapakse RKND, et al. Ex situ characterization and modelling of fatigue crack propagation in catalyst coated membrane composites for fuel cell applications. International Journal of Hydrogen Energy 2019;44:12057–72. https://doi.org/10.1016/j.ijhydene.2019.03.108.

[223] Kai Y, Kitayama Y, Omiya M, Uchiyama T, Kato M. Crack Formation in Membrane Electrode Assembly Under Static and Cyclic Loadings. Journal of Fuel Cell Science and Technology 2013;10:021007. https://doi.org/10.1115/1.4023878.
[224] Kundu S, Fowler MW, Simon LC, Grot S. Morphological features (defects) in fuel cell membrane electrode assemblies. Journal of Power Sources 2006;157:650–6. https://doi.org/10.1016/j.jpowsour.2005.12.027.
[225] Tavassoli A, Lim C, Kolodziej J, Lauritzen M, Knights S, Wang G, et al. An experimental study on local thinning and pinhole formation phenomena in PEM fuel cell membranes. ECS Meeting Abstracts, IOP Publishing; 2014, p. 1091.
[226] de Bruijn FA, Dam VAT, Janssen GJM. Review: Durability and Degradation Issues of PEM Fuel Cell Components. Fuel Cells 2008;8:3–22. https://doi.org/10.1002/fuce.200700053.
[227] Tsushima S, Hirai S. An overview of cracks and interfacial voids in membrane electrode assemblies in polymer electrolyte fuel cells. JTST 2015;10:JTST0002–JTST0002. https://doi.org/10.1299/jtst.2015jtst0002.
[228] Uzundurukan A, Bilgili M, Devrim Y. Examination of compression effects on PEMFC performance by numerical and experimental analyses. International Journal of Hydrogen Energy 2020;45:35085–96. https://doi.org/10.1016/j.ijhydene.2020.04.275.
[229] Lu Z, Lugo M, Santare MH, Karlsson AM, Busby FC, Walsh P. An experimental investigation of strain rate, temperature and humidity effects on the mechanical behavior of a perfluorosulfonic acid membrane. Journal of Power Sources 2012;214:130–6. https://doi.org/10.1016/j.jpowsour.2012.04.094.

Chapter II: Determination of the orthotropic mechanical elastic properties of gas diffusion layers[1]

The previous literature review has obviously highlighted the lack of experimental data on the mechanical behavior of the gas diffusion layer. The majority of the mechanical studies focused on characterizing in-plane properties or non-linear response under compression. The aim of this chapter is to provide a complete analysis of the mechanical properties of gas diffusion layers in the different directions. A series of experimental tests (tensile, shear and compression) were conducted to allow the determination of the orthotropic behavior by identifying the in-plane and out-of-plane properties according to the machine direction and the transverse direction.

The experimental campaign was performed on a panoply of GDL types (roll and sheet), distinguished by different areal weight, hydrophobic treatment and manufacturing process.

The obtained database of properties could eventually be implemented in a numerical study in the following chapter and provide key information on the impact of the GDL behavior on the performance of the cell.

[1] Partially reproduced from M. Ouerghemmi, C. Carral, P. Mele.
Submitted to *International Journal of Hydrogen Energy*

Determination of the orthotropic mechanical elastic properties of gas diffusion layers

Marwa Ouerghemmi, *Christophe* Carral, and *Patrice* Mele

Univ. Grenoble Alpes, Univ. Savoie Mont Blanc, CNRS, Grenoble INP, LEPMI, Grenoble, 38000, France

I. Abstract:

One of the most important components of proton exchange membrane fuel cell is the gas diffusion layer (GDL), owing to its key role in the reactant diffusion, water management, thermal and electron conductivity. The GDL must, therefore, have an optimal stiffness to ensure these transport functions during the operation of the system. The understanding of its mechanical behavior is essential and will be the subject of this article. The development of a series of in-plane and out-of-plane mechanical characterizations has provided a comprehensive analysis of the orthotropic mechanical properties of GDLs. This study brings additional understanding into the origin of the differences in mechanical behavior of different GDLs and allowed the creation of a database of the orthotropic mechanical properties of the main commercialized references.

Keywords: Proton exchange membrane fuel cell, gas diffusion layer, mechanical characterization, orthotropic non-linear behavior, Poisson's ratio

II. Introduction:

Proton exchange membrane fuel cells (PEMFC) are subjected to different range of stresses induced by its assembly process and its operating conditions, which have a direct impact on its performances and durability [1–4]. Different studies have confirmed that the fuel cell's performance improve with the increase of the gas diffusion layer's compression ratio, because it reduces its thickness and the interfacial resistance between layers leading to better electrochemical performances. However, too high clamping pressure can restrict gas and water transport within the cells and damages individual components of the fuel cell core, leading to a decrease in the system's performance [5–10]. Therefore, there is an optimum clamping pressure for the PEMFC, but the value of which varies according to its operation. In general, the optimum compressive stress is between 1 and 1.5 MPa [11,12]. Various numerical studies have shown that the operating conditions, involving changes in temperature and humidity, can cause values below or above this level as well as a non-uniform stress [13–15]. A study by Carral *et al*. [16,17] showed that increasing the number of cells in a stack will improve the pressure uniformity, leading to a decrease of 20% of the interfacial contact resistance. Moreover, a non-uniform compression can promote delamination between the membrane electrode assembly (MEA) different layers and the creation of defects such as pinholes and cracks in the

membrane [18,19], since the response to the mechanical stress is different from one layer to another in the stack [16,20]. The influence of the stresses intensities on the MEA different layers were investigated in the review of Dafalla *et al*. [21], and showed that the stresses generated by the clamping process and the operating conditions induces serious damages or even degradations of the cell's components.

It should be pointed out that the GDL is one of the most important components in the cell, as it governs the gas and electron transport, as well as water and heat management from the active layers to the bipolar plates channels. An excessive decrease in the porosity inhibits the gas circulation and blocks the water evacuation [22–27]. The compression force has a huge impact on its morphology [22–24]. The cyclic compression causes significant and irreversible changes in the GDL's microstructure. The average pore size and distribution are reduced by almost 70% under compressive stress up to almost 10 MPa [25]. It is therefore important that the GDL presents an optimal mechanical rigidity to ensure these transport functions, during the many hydrothermal cycles, and have sufficient mechanical resistance to hold the MEA and resist intrusion of the bipolar plates ribs.

The microstructure of gas diffusion layers makes their characterization challenging. It is a fibrous porous material mainly made of PolyAcryloNitril-based carbon fibers. The porosity is typically estimated around 70% to 80% [28] and the thicknesses of commercially available GDLs are typically in the range of 150–400 μm [29]. Gas diffusion layers can be grouped into two main categories: woven, also known as cloth, and non-woven. The latter is made of whether spun laced carbon fibers, also known as spaghetti fibers, to produce felt, or straight carbon fibers that are chopped. A papermaking process is applied, including a carbonization or graphitization step, to obtain a substrate composed of virtually only carbon fibers. A hydrophobic treatment and a micro-porous layer (MPL) are generally added as a final step to the fibers to improve the fuel cell operation. The final product can be supplied in roll form (manufacturing process with a carbonization step) or sheet form (manufacturing process with a graphitization step). As cited above, GDLs undergo a hydrophobic treatment, such as adding polytetrafluoroethylene (PTFE) for better efficiency. Indeed, extensive research have shown that PTFE improves the water transport, notably when a cell operates under flooding. This phenomenon takes place if the water accumulates in a region needed for reactant supply, leading to significant reactant and gas transport limitations [28]. However excessive PTFE loading could lead to a high flooding level in the catalyst layer [30]. Most of the studies reported in the literature in this topic [31–33] investigated the GDL optimum properties in terms of PTFE content in the MPL. The best performances were obtained for a PTFE content between 15 and 20 wt.% [31,32]. Kumar *et al*. [33] studied the impact of multistage PTFE treatment on the GDL properties; they confirmed that GDL subjected to multistage PTFE treatment can have an increased lifetime compared to a GDL treated with PTFE in a single stage.

It was also found that using a GDL with MPL enhances the PEMFC performances [34]. Morgan *et al*. [35] showed that applying multiple MPL to the GDL allows a gradual change in pore structure which enhances water management. Multiple studies on the MPL materials and structure were collected in a recent review by Zhang *et al*. [36], who mentioned that one of the two major roles of MPL is reducing the size of the water droplets and liquid saturation level at the catalyst layer/MPL interface due to its small pore size, which improves the catalytic activity and durability.

Most of the mechanical studies of the GDL were focusing on characterizing (i) its in-plane properties, often assuming it as an isotropic linear material, or (ii) only its non-linear behavior under compression. In our knowledge, only a few studies [37–39] studied the mechanical properties of GDLs in different directions of loading. Kleemann *et al*. [37] developed different measurement methods to determine the in-plane moduli as well as the out-of-plane shear modulus and Poisson's ratio. In-plane moduli were determined using a 3-point bending test following the DIN 53121[40] and EN 13706-2 [41] standards. The through plane Poisson's ratio was determined via a compression test of a stack of 5 GDL-samples. This test was set up to quantify the change in the sample diameter as well as the thickness variation. Both displacements were measured using an optical microscope. The out-of-plane Poisson's ratio was found to be close to zero. As for the through-plane shear modulus, an indirect technique was developed by the same authors [37], with the short-beam bending method and numerical simulations. Poornesh *et al*. [38,42] conducted a theoretical and experimental analysis to investigate the anisotropic behavior of GDLs. They measured the in-plane elastic moduli using Taber stiffness and the through-plane shear modulus with the short-beam bending test inspired by the method developed by Kleemann *et al*. [37]. Chen *et al*. [39] also developed measurement methods to determine the different material orthotropic properties. A tensile test was performed following the standard ASTM D638 [43] and the shear test was performed according to Lai's method [44]. As for the compression test, it was performed on separate samples under a pressure up to 5 MPa, which was inspired by their previous work [45].

The identification of the mechanical properties of GDL requires the development of robust characterization methods, subject of this study. A series of tests have been implemented to allow the mechanical characterization of GDLs in all the specific directions: in-plane, along the machine (MD) and transverse (CD) directions, and out- of-plane. These tests allow the determination of the tensile moduli E_x, E_y, in-plane shear moduli G_{xy}, G_{yx}, out-of-plane compression modulus E_z and shear moduli G_{xz} , G_{yz} , and finally in-plane Poisson's ratios v_{xy}, v_{yx}. This study should provide a complete analysis of the orthotropic properties of the GDL. A large spectrum of GDL commercial references was considered in this experimental study to analyze the effects of the type of GDL (roll or sheet), areal weight, hydrophobic treatment, manufacturing process, and micro porous layer, on the different mechanical properties.

III. Experimental details

1. Materials

A range of the most commercialized references of GDL has been characterized, from different manufacturers, with various PTFE contents, and exhibiting or not a MPL (***Table 1***). For each reference, a GDL sheet of about 60x60 cm^2 was the source of the samples; that implies that the dispersion of properties within a batch or between different batches is not taken into account in this experimental study. For the SGL references, the suffix AA corresponds to GDLs composed of fibers only, BB and BC corresponds to GDLs with hydrophobic treatment and MPL. To illustrate the different GDLs employed, X-ray tomography observations of some references have been made and are shown in ***Figure 1***.

Table 1: *List of studied GDLs samples and main characteristics.*

GDL type	Manufacturer	Reference	Thickness (µm) @0.01MPa	Bulk density @0.01MPa ($g.cm^{-3}$)	Areal weight ($g.m^{-2}$)	PTFE (%)	MPL
Roll	AvCarb	EP40	209±2	0.17	36±1	0	No
	SGL Carbon	28AA	180±6	0.26	47±2	0	No
	SGL Carbon	29AA	184±4	0.18	34±1	0	No
	SGL Carbon	36AA	236±1	0.24	57±1	0	No
	SGL Carbon	38AA	283±4	0.27	75±1	0	No
	SGL Carbon	39AA	265±12	0.20	52±4	0	No
Roll+PTFE	SGL Carbon	28AA-09	180±2	0.29	52±1	9.2	No
	SGL Carbon	28AA-18	177±3	0.32	57±1	17.9	No
	SGL Carbon	28AA-29	184±3	0.34	63±1	28.8	No
Roll+PTFE+MPL	SGL Carbon	22BB	227±3	0.30	67±1	15.0	Yes
	SGL Carbon	36BB	287±3	0.36	103±1	13.2	Yes
	SGL Carbon	28BC	257±3	0.41	105±1	12.8	Yes
	SGL Carbon	39BC	334±3	0.34	112±1	15.0	Yes
Sheet	Spectracarb	2050A	262±8	0.34	88±1	0.4	No
	Toray	H060	213±4	0.40	85±1	9.7	No
	Toray	H090	304±3	0.44	133±2	N.A.	No

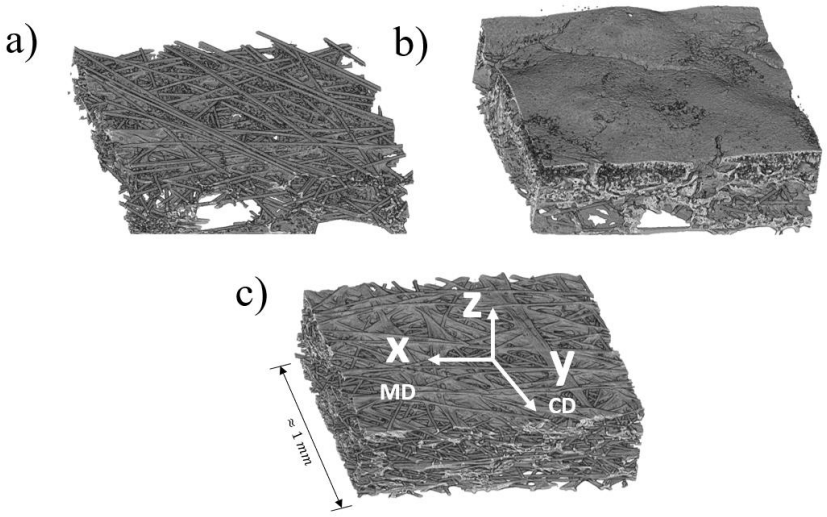

Figure 1 *Tomographic images of (a) a roll GDL (39AA), (b) a roll GDL with PTFE and MPL (39BC) and (c) a sheet GDL (H090).*

2. Experimental characterizations

A schematic representation describing the different in-plane and out-of-plane tests performed in this study are presented in ***Figure 2***. The representative experimental curves and the method of extraction of the different moduli are detailed in ***Figure 3***. All of the tests have been performed on a minimum of 5 samples.

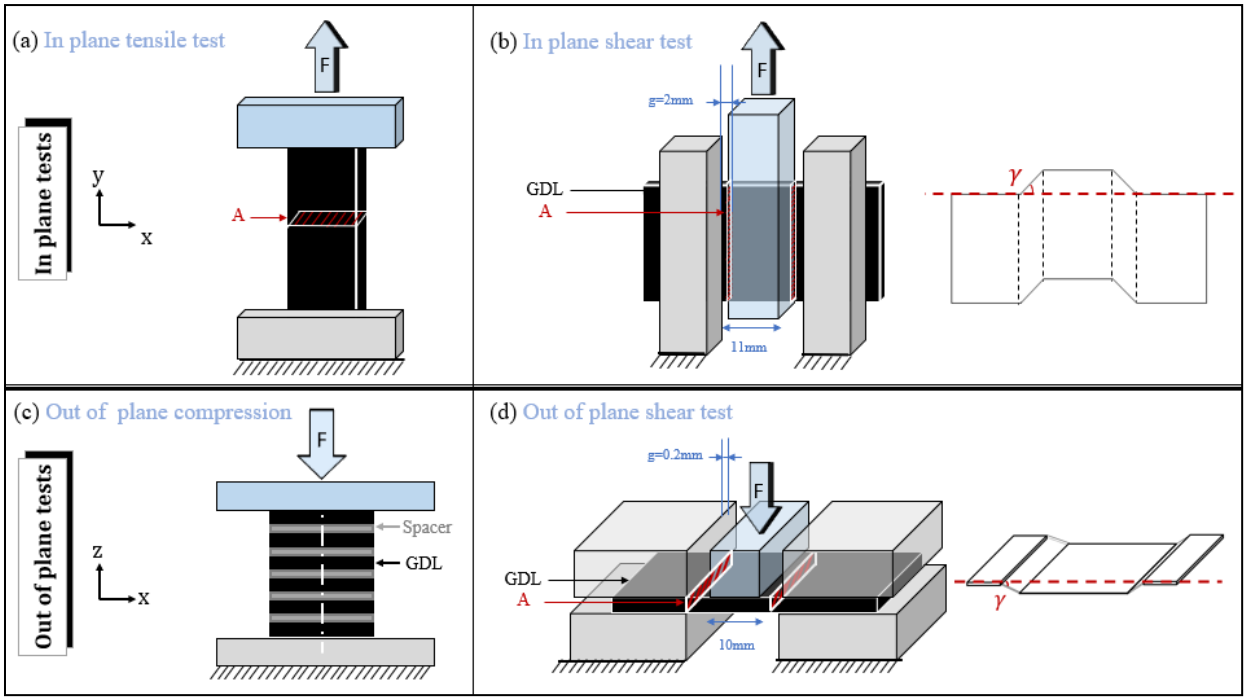

Figure 2: *Schematic representation of the different tests performed on GDLs.*

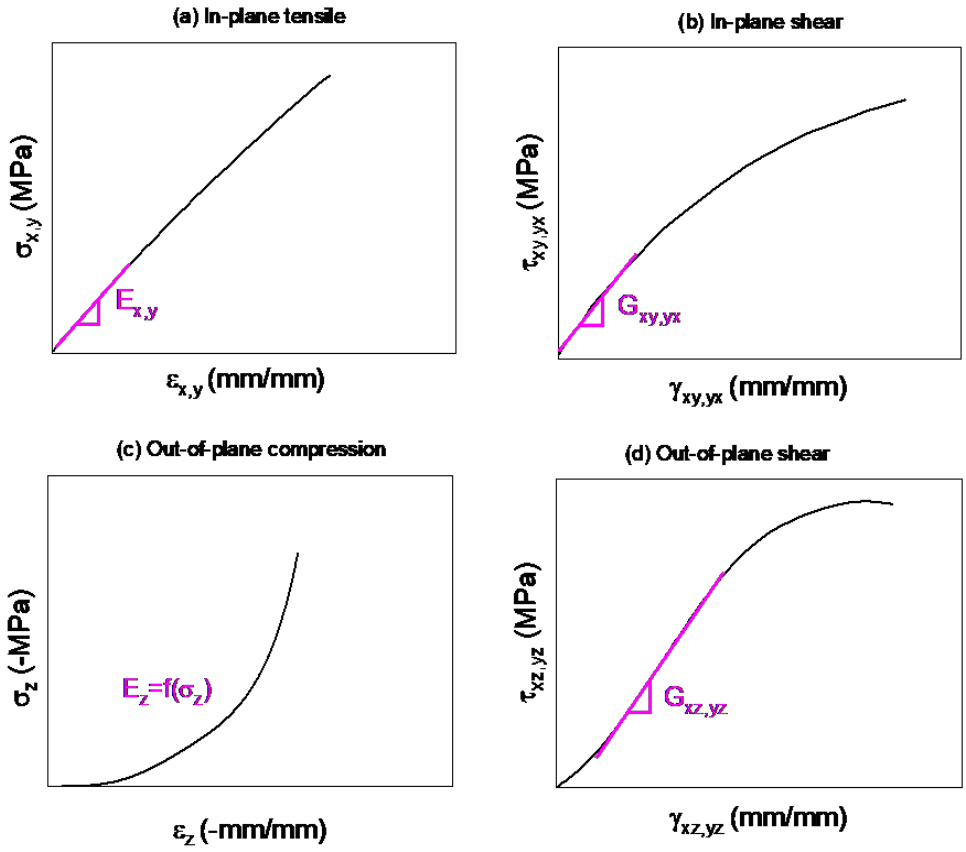

Figure 3: *Representative curves of the different tests and moduli extraction methods. (a) In-plane tensile curve, (b) in-plane shear curve, (c) out-of-plane compression curve and (d) out-of-plane shear curve.*

i. In-plane tensile test

The in-plane tensile tests were carried out on a Metravib-Acoem VA4000 machine with a 140N force sensor, the displacement speed was 1 $mm.min^{-1}$.

A study on the optimization of the sample dimensions was carried out during the implementation of the experimental protocol based on the ISO 1924 [46]. This analysis was used to verify the good repeatability of the results. The chosen dimensions for the tensile specimen were 5mm of width and 40mm for the gauged length.

The nominal strains ($\varepsilon_{x,y}$) and stress ($\sigma_{x,y}$) were calculated with the following equations:

$$\sigma_{x,y} = \frac{F}{A} \quad (1)$$

$$\varepsilon_{x,y} = \frac{\Delta l}{l_0} \quad (2)$$

where F is the tensile force, A is the cross-sectional area, Δl is the change in length and l_0 is the initial length.

ii. In-plane shear test

The in-plane shear tests were performed on the same machine as the tensile tests with a specific device (***Figure 2b***). Samples were rectangular with dimensions of 30mm×15mm. In-plane shear stress ($\tau_{xy,yx}$) and strain ($\gamma_{xy,yx}$) were calculated as follows:

$$\tau_{xy,yx} = \frac{F}{2A} \quad (3)$$

$$\gamma_{xy,yx} = \frac{d}{g} \quad (4)$$

where F is the shear force, A is the cross-sectional area, d is the vertical displacement, and g is the air gap between the jigs.

iii. Out-of-plane shear test

Out-of-plane shear tests were performed on the same machine as the tensile tests and the in-plane shear tests with a specific out-of-plane shear device (***Figure 2d***). The out-of-plane shear test is based on the method described in reference [44]. Samples were rectangular with dimensions of 30mm×25mm. Out-of-plane shear stress in the machine direction ($\tau_{xz,xz}$) and strains ($\gamma_{xz,yz}$) were calculated with the following formulae:

$$\tau_{xz,yz} = \frac{F}{2A} \quad (5)$$

$$\gamma_{xz,yz} = \frac{d}{g} \quad (6)$$

The air gap between jigs is equal to 0.2mm, it was optimized in order to have the smallest gap and thus to get closer to a pure shear loading.

iv. Out-of-plane compression test

The out-of-plane compression tests were carried on an Instron 8872 machine, equipped with a 5kN force sensor. The displacement was measured with a clip-on extensometer installed on the compression plates. Tests were carried out on a stack of 6 GDLs of 16 mm diameter, with aluminum spacers of 100 µm thickness (***Figure 2c***). These spacers were used to separate the samples and prevent the interpenetration of carbon fibers [20].

Only the loading part of the compression of the stack was analyzed with a stress ranging from 0.01MPa up to 20MPa; 0.01MPa being the contact pressure at which the stack thickness was measured. Compressive stress and strain were calculated as follows:

$$\sigma_z = \frac{F}{A} \quad (7)$$

$$\varepsilon_z = \frac{\Delta th}{th_0} \quad (8)$$

where F is the compressive force, A is the specimen area, Δth is the variation in thickness and th_0 is the initial thickness.

v. In-plane Poisson's ratio

As noted above, the out-of-plane Poisson's ratio is expected to be equal to 0, due to the crushing of the porosity during the compression of the GDL, and as measured by Kleemann *et al*. [37]. This work then focuses on the measurement of the in-plane Poisson's ratio. Tensile tests were carried out on a Shimadzu AGS-X equipped with a video extensometer to measure the longitudinal and transverse displacements in order to estimate the Poisson's ratio. A force sensor of 100 N and displacement speed equals to 1 $mm.min^{-1}$ were employed. The samples were cut in both MD and CD directions and had a rectangular shape with a width equals to 30 mm, greater than that of the tensile tests in order to increase the amplitude of the transverse displacement for the determination of the Poisson's ratio. Tensile tests were performed cyclically: 2 cycles per specimen. The longitudinal and transverse strains were determined from the changes in the displacements in the x and y directions via the locations of marker points during the test given by the extensometer. The displacements were normalized by the initial length values between marks to obtain the strains. Two Poisson's ratio have been estimated, ν_{xy} and ν_{yx}, corresponding to a direction of loading in x and y directions, respectively, and are calculated as follows [47]:

$$\nu_{xy} = -\frac{\varepsilon_y}{\varepsilon_x} \quad (9)$$

$$\nu_{yx} = -\frac{\varepsilon_x}{\varepsilon_y} \quad (10)$$

For GDLs with MPL, tests were carried out with the measurements of the transverse displacement on both sides, in order to analyze the possible influence of this layer.

IV. Results

1. Tensile and shear tests

All tested GDLs exhibit a linear behavior under in-plane tensile or shear tests. Moduli can be then determined for each solicitation and are shown for the different GDL references in ***Figures 4, 5*** and ***6***. All dispersions of results correspond to the range of the experimental measurements on the samples. Although the experimental work was

performed on a wide variety of GDL references, the magnitudes of the moduli found for the different GDLs are in accordance with those published in the literature [37,38].

Sheet GDLs exhibit higher tensile moduli (5-10 GPa) compared to rolls (2-5 GPa). The higher stiffness of sheets is due to the graphitization step that is performed on this type of GDLs. This thermal treatment changes the fiber structure resulting in higher tensile modulus [28].

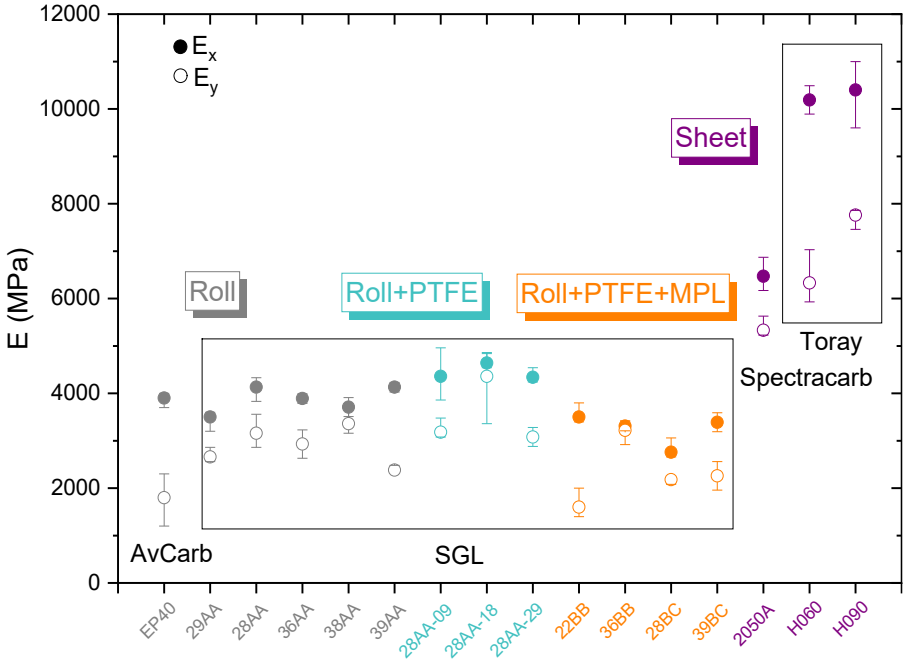

Figure 4: *In-plane tensile moduli for the different GDL references.*

An in-plane anisotropy of the tensile properties (***Figure 4***) can be observed for all samples, characterized by the difference between moduli in both directions. This result is related to the non-uniform fiber orientation distribution [38], induced by a non-uniform dispersion of the fibers during the paper making and amplified by the calendering performed during the manufacturing process [28]. Observing the SGL references, the results show that the anisotropy varies significantly even for the same supplier, with ratios E_x/E_y in the range of 1:1 to 5:1. Anisotropic ratios do not exceed 5:1 for the other references from other manufacturers. It is important to note that higher dispersion of measurements, and higher anisotropic ratios E_x/E_y, could be expected on a whole GDL batch production and between different batches, the measurements presented here being made on a relatively small sample (cf. section materials).

Observing the references 28AA with PTFE, a slight increase of E_x (+12%) is observed from the sample without PTFE and the sample with 18w% PTFE. However, the value of E_x decreases for the sample with 29wt%. Overall, there is no strong influence of the PTFE content on the in-plane tensile properties.

According to the measurements shown for the rolls, adding a MPL leads to a decrease of the moduli in both directions. It could be due to the fact that adding this new layer to the

fibers substrate increases the thickness of the whole component without providing any mechanical stiffness. This hypothesis could be expected since the MPL is composed mainly of carbon or graphite particles [28], which cannot provide significant tensile mechanical properties.

The in-plane shear moduli are in the range of 100 to 300 MPa (***Figure 5***), one order of magnitude below the tensile properties. As for isotropic material, a decrease of the shear modulus compared to the tensile one can be expected. The values of G_{xy} and G_{yx} are similar; the differences being within the range of the measurement dispersion, meaning that there is no clear anisotropy induced by the in-plane fiber orientation on this parameter. In contrast to the tensile properties, the in-plane shear properties are only moderately higher for sheets compared to rolls. As for the tensile properties, PTFE and MPL do not induce a significant change of the in-plane shear properties.

The out-of-plane shear moduli are in the range of 1 to 5 MPa (***Figure 6***), well below the in-plane properties, due to the fact that the fibers are almost exclusively dispersed in 2D in the xy plane. The same observations can be made on this property as for the in-plane shear, i.e. a slight increase of the stiffness for the sheet type compared to rolls and no significant influence of PTFE and MPL. An anisotropy can be observed between G_{xz} and G_{yz} for the sheet type but is less clear for rolls.

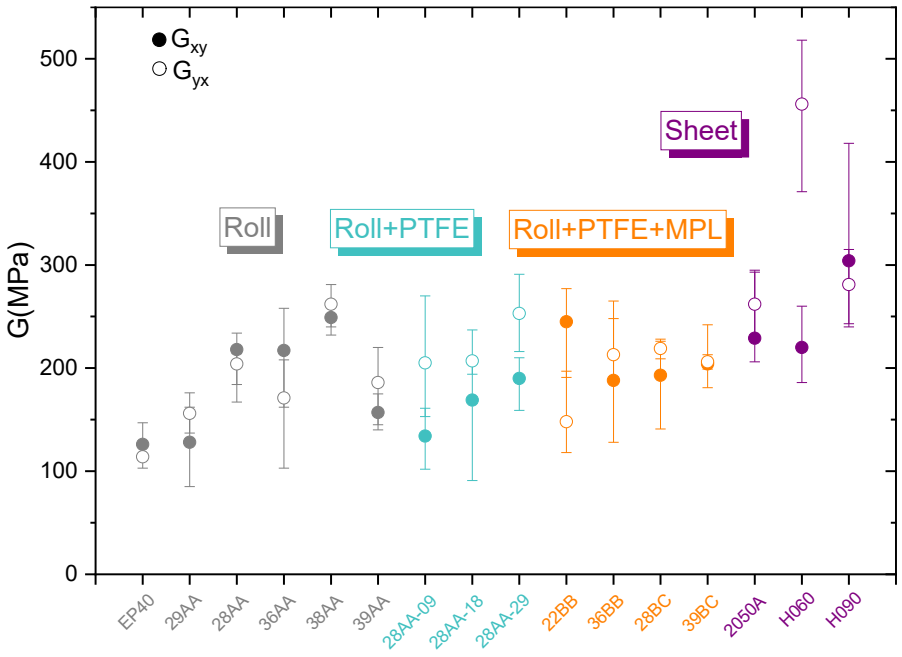

Figure 5: *In-plane shear moduli for the different GDL references.*

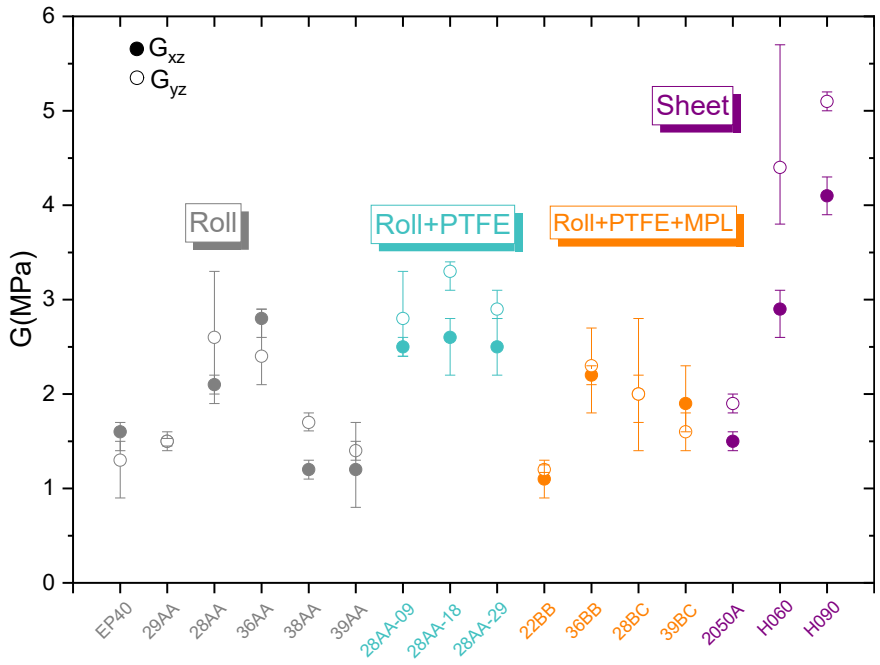

Figure 6: *Out-of-plane shear moduli for the different GDL references.*

2. Poisson's ratios

The evolution of the transverse strain as a function of the longitudinal strain of a roll GDL (SGL 22 BB) on the fibers side and on the MPL side are shown in ***Figure 7a*** and ***Figure 7b***, respectively. We can observe small variations of the transverse strain of the GDL on the fibers side while they are almost equal to zero on the MPL side. The values of the Poisson's ratio estimated from these measurements are then collected in Table 2. On the fibers side of the 22BB, Poisson's ratio values are 0.19 and 0.35 for ν_{xy} and ν_{yx} respectively.

The experimental measurements show a Poisson's ratio close to 0 for the MPL side and also for sheets, the transverse displacement variations being within the resolution limit of the video extensometer. It is important to note that even with increasing the width of the sample up to 30 mm, the transverse displacement measured were lower than 1 µm, due to the brittleness of the GDL associated to its relatively high tensile stiffness.

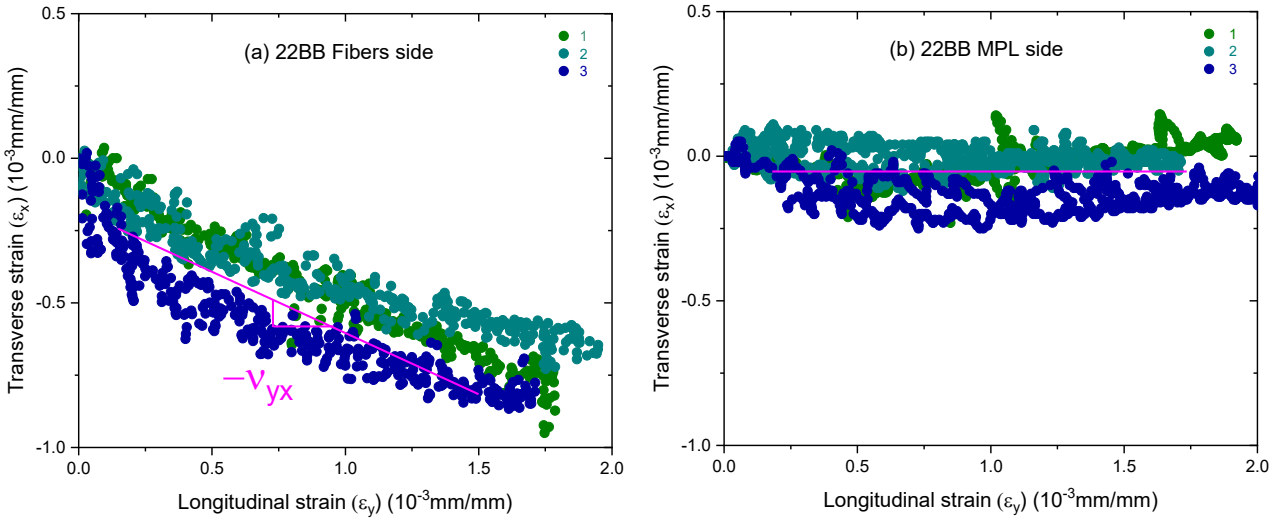

Figure 7*: Evolutions of the transverse strain with the longitudinal strain, (a) on the fibers side and (b) on the MPL side for 3 samples of the reference SGL 22BB, for a tensile load in y direction (measurement of ν_{yx}).*

Table 2: *Values of measured in-plane Poisson's ratio for 2 GDL types (roll/sheet).*

GDL	ν	Fibers	MPL
Roll 22BB	ν_{xy}	$0.19^{+0.09}_{-0.03}$	≤ 0.05
	ν_{yx}	$0.35^{+0.08}_{-0.06}$	≤ 0.05
Sheet H090	ν_{xy}	≤ 0.05	N/A
	ν_{yx}	≤ 0.05	N/A

3. Compression test

The GDL's behavior under out-of-plane compression is non-linear (***Figure 8***). This non-linearity is related to the increase of contact between the fibers during the compression, as shown by different authors [20,37,48–50]. The modulus is then dependent on the strain, or stress, applied during the compression. A tangent modulus, E_z, can be evaluated via the derivative of the stress-strain curves, and is depicted in ***Figure 9*** in function of the compressive stress applied. A zoom on the compression pressure lower than 5 MPa show a curve shoulder that appears for all references, with the exception of the references 39AA and 39BC. As observed is a recent study [51], this peak reveals the effect of the pressure applied during the manufacturing process, named thereafter σ_P. The value of σ_P can be then evaluated for each reference via the inflection point after the mentioned peak and is reported in Table 3 for the different references studied. The higher σ_P, the higher the modulus is at the beginning of the compression, and hence the whole stress-strain curve shift to the left (higher global stiffness). Once σ_P is reached, E_z follows a linear evolution with the compressive stress, as observed by Meng *et al.* [52], linked to the native behavior of the GDLs. It is then essential to take into account this parameter when comparisons are

made between the different GDLs. Rolls references with the lowest σ_P (39AA, EP40, 29AA) are thus found to be the least rigid GDLs.

The three references of sheets are stiffer than most of rolls (without PTFE and MPL). This can be expected since the graphitized carbon fibers of sheet GDLs exhibit higher modulus. The difference of stiffness is however limited and could be emphasized by the high σ_P values found on Toray's sheets.

The analysis of the references 28AA with and without PTFE allows a direct comparison for the influence of the hydrophobic treatment on the non-linear behavior of the GDL. The behaviors are similar whatever the PTFE content.

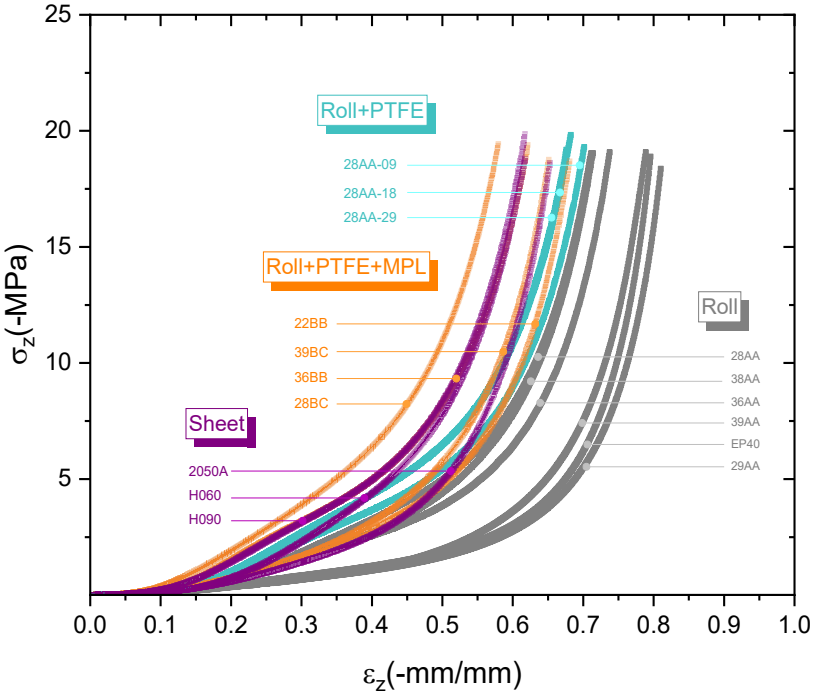

Figure 8: *Stress-strain curve of the compression test for the different types of GDL.*

In contrast to other mechanical properties studied, the addition of a MPL seems to affect the compression behavior by increasing its stiffness. Direct comparison can be made between GDLs with the same fibers' substrate (28AA and 28BC, 39AA and 39BC, 36AA and 36 BB): for all couple of references, a stiffer stress-strain curves is obtained in compression for the reference with MPL, and this for a similar σ_P. As cited above, the MPL is composed mainly of carbon and graphite particles, that cannot provide a mechanical response to tensile or shear solicitation; its presence, however, affects the out-of-plane nonlinear behavior of the GDL by densifying the material and increasing the number of contacts between fibers, a mechanism assumed to be responsible for the nonlinearity of GDL.

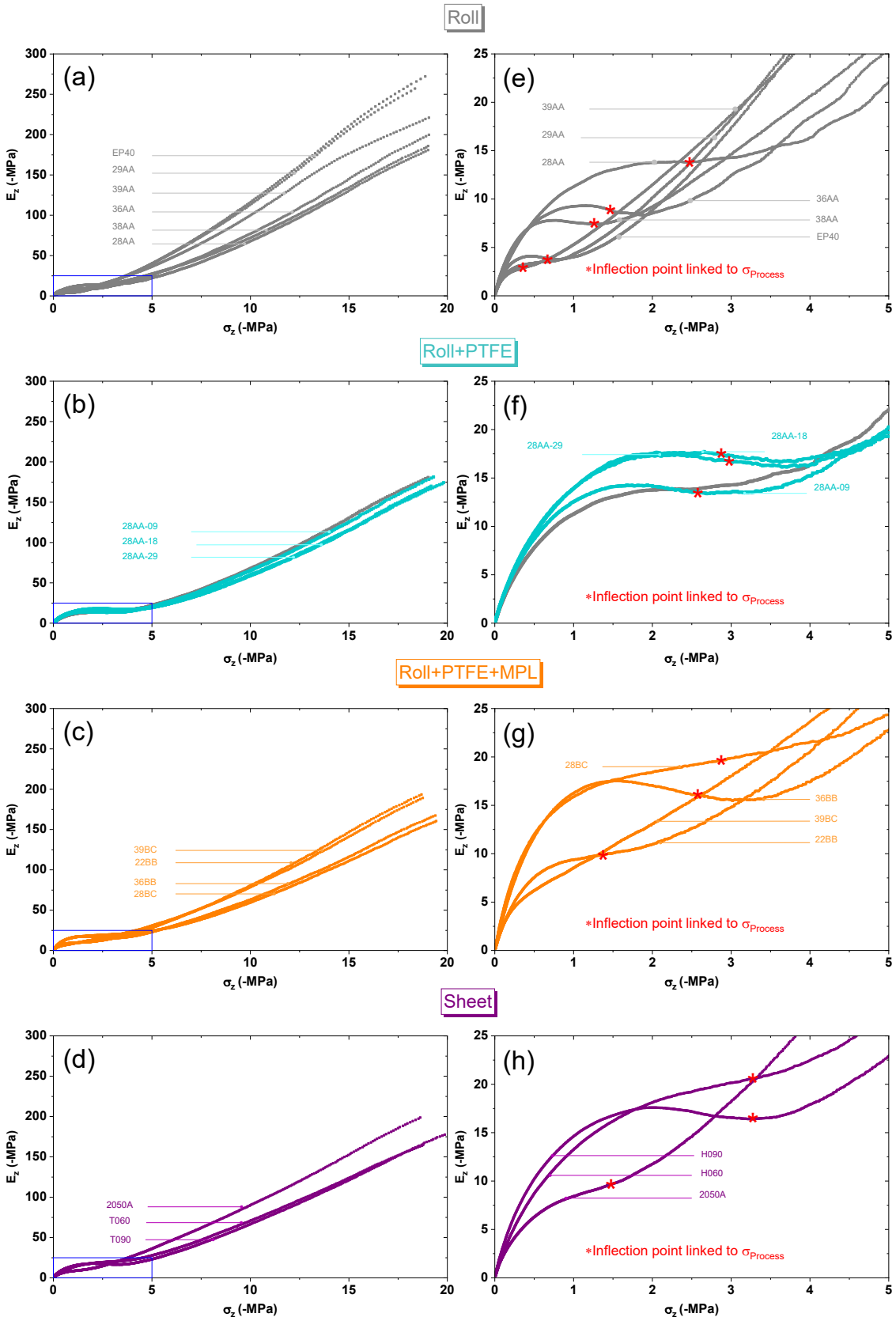

Figure 9: *Evolution of the compressive tangent modulus Ez as a function of the compressive stress σ_z for the different GDL references. (a-d) The entire experimental curves and (e-h) A zoom view from 0MPa to 5MPa.*

Table 3: *Assumed values of the pressure applied during the manufacturing process (σ_P) of the different GDL references.*

Reference	σ_P(MPa)
EP40	0.4
28AA	2.6
29AA	0.7
36AA	1.5
39AA	N.A.
38AA	1.3
28AA-09	2.8
28AA-18	2.9
28AA-29	2.9
22BB	1.3
36BB	2.5
28BC	2.8
39BC	N.A.
2050A	1.4
T060	3.2
T090	3.2

V. Conclusion

The complex structure of GDLs, made of dispersed carbon or graphite fibers, requires a meticulous mechanical characterization to better understand its influence on the general behavior of the PEM during its operation. The study of its mechanical behavior required the development of a series of in-plane and out-of-plane mechanical tests, due to this complex structure inducing an orthotropic behavior. The new experimental methods were then applied on different types of GDLs, including GDLs in sheet and roll form, with different PTFE contents and with or without MPL layer. These tests were also carried out in the machine and cross direction to evaluate the 2D anisotropy of GDLs. The main results of this study are:

(i) GDLs in sheet form have a higher in-plane and out-of-plane stiffness than GDLs in roll form.

(ii) No significant influence of the hydrophobic treatment was observed, i.e. addition of PTFE to the GDL.

(iii) The presence of MPL did not affect the in-plane properties, but increased the stiffness of the material during out-of-plane compression.

(iv) The 2D anisotropy of GDL is not significant compared to its 3D anisotropy, i.e. between in-plane and out-of-plane directions, with mechanical moduli ranging from several GPa to few MPa respectively. This indicates that the mechanical behavior of GDLs tends to an isotropic transverse behavior.

(v) In-plane Poisson's ratio values of GDLs were measured and presented for the first time in this article. For sheet GDLs, and the MPL side of roll GDLs, no transverse displacements were detected, indicating that the in-plane Poisson's ratios for these materials tend towards zero. Values of 0.2 and 0.35 were estimated for the in-plane Poisson's ratios on the fibrous part of roll GDLs.

This study finally brings a deeper understanding of the origins of the mechanical behavior of GDLs and allows the creation of a database of the orthotropic mechanical properties of the most commercially available GDL references. It will allow to refine the predictions of the behavior of PEMFCs during their operation and to contribute in fine to the improvement of their performances.

Acknowledgement

This work was financed by the French ministry of research, and supported by the CNRS Energy unit (Cellule Energie) through the project DEVOPEM, and by the CARNOT project OPTIPEM. The authors are grateful to SGL Carbon Company, especially Susanne Bacher and Nico Haak, for providing 36AA-36BB-22BB samples. The authors would like to thank Gilles de Moor for the PTFE content measurements, and Stephane Coindeau and Pierre Lhuissier for the help on the tomographic images.

References

[1] Ozden A, Shahgaldi S, Li X, Hamdullahpur F. A review of gas diffusion layers for proton exchange membrane fuel cells—With a focus on characteristics, characterization techniques, materials and designs. Progress in Energy and Combustion Science 2019;74:50–102. https://doi.org/10.1016/j.pecs.2019.05.002.

[2] Zhang Z, He P, Dai Y-J, Jin P-H, Tao W-Q. Study of the mechanical behavior of paper-type GDL in PEMFC based on microstructure morphology. International Journal of Hydrogen Energy 2020;45:29379–94. https://doi.org/10.1016/j.ijhydene.2020.07.240.

[3] Uzundurukan A, Bilgili M, Devrim Y. Examination of compression effects on PEMFC performance by numerical and experimental analyses. International Journal of Hydrogen Energy 2020;45:35085–96. https://doi.org/10.1016/j.ijhydene.2020.04.275.

[4] Bouziane K, Khetabi EM, Lachat R, Zamel N, Meyer Y, Candusso D. Impact of cyclic mechanical compression on the electrical contact resistance between the gas diffusion layer and the bipolar plate of a polymer electrolyte membrane fuel cell. Renewable Energy 2020;153:349–61. https://doi.org/10.1016/j.renene.2020.02.033.

[5] Ihonen J, Mikkola M, Lindbergh G. Flooding of gas diffusion backing in PEFCs: physical and electrochemical characterization. Journal of the Electrochemical Society 2004;151:A1152.

[6] Mishra V, Yang F, Pitchumani R. Measurement and prediction of electrical contact resistance between gas diffusion layers and bipolar plate for applications to PEM fuel cells 2004.

[7] Ge J, Higier A, Liu H. Effect of gas diffusion layer compression on PEM fuel cell performance. Journal of Power Sources 2006;159:922–7. https://doi.org/10.1016/j.jpowsour.2005.11.069.

[8] Escribano S, Blachot J-F, Ethève J, Morin A, Mosdale R. Characterization of PEMFCs gas diffusion layers properties. Journal of Power Sources 2006;156:8–13. https://doi.org/10.1016/j.jpowsour.2005.08.013.

[9] Chang WR, Hwang JJ, Weng FB, Chan SH. Effect of clamping pressure on the performance of a PEM fuel cell. Journal of Power Sources 2007;166:149–54. https://doi.org/10.1016/j.jpowsour.2007.01.015.

[10] Park J, Oh H, Ha T, Lee YI, Min K. A review of the gas diffusion layer in proton exchange membrane fuel cells: durability and degradation. Applied Energy 2015;155:866–80.

[11] Karvonen S, Hottinen T, Ihonen J, Uusalo H. Modeling of Polymer Electrolyte Membrane Fuel Cell Stack End Plates. Journal of Fuel Cell Science and Technology 2008;5:041009. https://doi.org/10.1115/1.2930775.

[12] Zhang L, Liu Y, Song H, Wang S, Zhou Y, Hu SJ. Estimation of contact resistance in proton exchange membrane fuel cells. Journal of Power Sources 2006;162:1165–71. https://doi.org/10.1016/j.jpowsour.2006.07.070.

[13] García-Salaberri PA, Vera M, Zaera R. Nonlinear orthotropic model of the inhomogeneous assembly compression of PEM fuel cell gas diffusion layers. International Journal of Hydrogen Energy 2011;36:11856–70. https://doi.org/10.1016/j.ijhydene.2011.05.152.

[14] Bates A, Mukherjee S, Hwang S, Lee SC, Kwon O, Choi GH, et al. Simulation and experimental analysis of the clamping pressure distribution in a PEM fuel cell stack.

International Journal of Hydrogen Energy 2013;38:6481–93. https://doi.org/10.1016/j.ijhydene.2013.03.049.
[15] Chi PH, Chan SH, Weng FB, Su A, Sui PC, Djilali N. On the effects of non-uniform property distribution due to compression in the gas diffusion layer of a PEMFC. International Journal of Hydrogen Energy 2010;35:2936–48. https://doi.org/10.1016/j.ijhydene.2009.05.066.
[16] Carral C, Mélé P. A numerical analysis of PEMFC stack assembly through a 3D finite element model. International Journal of Hydrogen Energy 2014;39:4516–30. https://doi.org/10.1016/j.ijhydene.2014.01.036.
[17] Carral C, Charvin N, Trouvé H, Mélé P. An experimental analysis of PEMFC stack assembly using strain gage sensors. International Journal of Hydrogen Energy 2014;39:4493–501. https://doi.org/10.1016/j.ijhydene.2014.01.033.
[18] Al-Baghdadi MAS. A CFD study of hygro–thermal stresses distribution in PEM fuel cell during regular cell operation. Renewable Energy 2009;34:674–82.
[19] Yim S-D, Kim B-J, Sohn Y-J, Yoon Y-G, Park G-G, Lee W-Y, et al. The influence of stack clamping pressure on the performance of PEM fuel cell stack. Current Applied Physics 2010;10:S59–61. https://doi.org/10.1016/j.cap.2009.11.042.
[20] Carral C, Mélé P. A constitutive law to predict the compression of gas diffusion layers. International Journal of Hydrogen Energy 2018;43:19721–9. https://doi.org/10.1016/j.ijhydene.2018.08.210.
[21] Dafalla AM, Jiang F. Stresses and their impacts on proton exchange membrane fuel cells: A review. International Journal of Hydrogen Energy 2018;43:2327–48. https://doi.org/10.1016/j.ijhydene.2017.12.033.
[22] Radhakrishnan V, Haridoss P. Effect of cyclic compression on structure and properties of a Gas Diffusion Layer used in PEM fuel cells. International Journal of Hydrogen Energy 2010;35:11107–18. https://doi.org/10.1016/j.ijhydene.2010.07.009.
[23] Khetabi EM, Bouziane K, Zamel N, François X, Meyer Y, Candusso D. Effects of mechanical compression on the performance of polymer electrolyte fuel cells and analysis through in-situ characterisation techniques - A review. Journal of Power Sources 2019;424:8–26. https://doi.org/10.1016/j.jpowsour.2019.03.071.
[24] Toghyani S, Moradi Nafchi F, Afshari E, Hasanpour K, Baniasadi E, Atyabi SA. Thermal and electrochemical performance analysis of a proton exchange membrane fuel cell under assembly pressure on gas diffusion layer. International Journal of Hydrogen Energy 2018;43:4534–45. https://doi.org/10.1016/j.ijhydene.2018.01.068.
[25] Zhou P, Wu CW, Ma GJ. Influence of clamping force on the performance of PEMFCs. Journal of Power Sources 2007;163:874–81. https://doi.org/10.1016/j.jpowsour.2006.09.068.
[26] Wilde PM, Mändle M, Murata M, Berg N. Structural and Physical Properties of GDL and GDL/BPP Combinations and their Influence on PEMFC Performance. Fuel Cells 2004;4:180–4. https://doi.org/10.1002/fuce.200400022.
[27] Taymaz I, Benli M. Numerical study of assembly pressure effect on the performance of proton exchange membrane fuel cell. Energy 2010;35:2134–40. https://doi.org/10.1016/j.energy.2010.01.032.
[28] Mathias M, Roth J, Fleming J, Lehnert W. Diffusion media materials and characterisation. Handbook of Fuel Cells—Fundamentals, Technology and Applications 2003;3:517–37.

[29] Omrani R, Shabani B. Review of gas diffusion layer for proton exchange membrane-based technologies with a focus on unitised regenerative fuel cells. International Journal of Hydrogen Energy 2019;44:3834–60. https://doi.org/10.1016/j.ijhydene.2018.12.120.
[30] Li H, Tang Y, Wang Z, Shi Z, Wu S, Song D, et al. A review of water flooding issues in the proton exchange membrane fuel cell. Journal of Power Sources 2008;178:103–17.
[31] Park G-G, Sohn Y-J, Yang T-H, Yoon Y-G, Lee W-Y, Kim C-S. Effect of PTFE contents in the gas diffusion media on the performance of PEMFC. Journal of Power Sources 2004;131:182–7.
[32] Lin G, Van Nguyen T. Effect of thickness and hydrophobic polymer content of the gas diffusion layer on electrode flooding level in a PEMFC. Journal of the Electrochemical Society 2005;152:A1942.
[33] Kumar RJF, Radhakrishnan V, Haridoss P. Enhanced mechanical and electrochemical durability of multistage PTFE treated gas diffusion layers for proton exchange membrane fuel cells. International Journal of Hydrogen Energy 2012;37:10830–5.
[34] Velayutham G, Kaushik J, Rajalakshmi N, Dhathathreyan K. Effect of PTFE content in gas diffusion media and microlayer on the performance of PEMFC tested under ambient pressure. Fuel Cells 2007;7:314–8.
[35] Morgan JM, Datta R. Understanding the gas diffusion layer in proton exchange membrane fuel cells. I. How its structural characteristics affect diffusion and performance. Journal of Power Sources 2014;251:269–78.
[36] Zhang J, Wang B, Jin J, Yang S, Li G. A review of the microporous layer in proton exchange membrane fuel cells: Materials and structural designs based on water transport mechanism. Renewable and Sustainable Energy Reviews 2022;156:111998.
[37] Kleemann J, Finsterwalder F, Tillmetz W. Characterisation of mechanical behaviour and coupled electrical properties of polymer electrolyte membrane fuel cell gas diffusion layers. Journal of Power Sources 2009;190:92–102. https://doi.org/10.1016/j.jpowsour.2008.09.026.
[38] Poornesh K, Cho C, Rego A. Anisotropic distribution of elastic constants in fuel cell gas diffusion layers: Experimental validation. Energy and Power 2015;5:40–5.
[39] Chen Y, Jiang C, Cho C. An experimental investigation of three-dimensional mechanical characteristics of gas diffusion layers in proton electrolyte membrane fuel cells. J Solid State Electrochem 2019;23:2021–30. https://doi.org/10.1007/s10008-019-04273-x.
[40] DIN 53121, Prüfung von Papier, Karton und Pappe - Bestimmung der Biegesteifigkeit nach der Balkenmethode, Deutsches Institut für Normung, Berlin, 1987. n.d.
[41] EN 13706-2, Reinforced plastics composites – Specification for Pultruded Profiles – Part 2:Methods of Test and General Requirements, European Committee for Standardization, Bruxels, 2002. n.d.
[42] Poornesh K, Vaz N, Rego A. Anisotropic Distribution of Elastic Constants in Fuel Cell Gas Diffusion Layers: Theoretical Assessment 2015;5:34–9. https://doi.org/10.5923/c.ep.201501.07.
[43] ASTM D638 (2010) Standard test method for tensile properties of plastics. ASTM International, West Conshohocken. https://doi.org/ 10.1520/D0638-10 n.d.
[44] Lai Y-H, Rapaport PA, Ji C, Kumar V. Channel intrusion of gas diffusion media and the effect on fuel cell performance. Journal of Power Sources 2008;184:120–8. https://doi.org/10.1016/j.jpowsour.2007.12.065.

[45] Chen Y, Jiang C, Cho C. An investigation of the compressive behavior of polymer electrode membrane fuel cell's gas diffusion layers under different temperatures. Polymers 2018;10:971.
[46] ISO 1924-2:2008 Papier et carton — Détermination des propriétés de traction — Partie 2: Méthode à gradient d'allongement constant (20 mm/min) n.d.
[47] Christensen RM. Mechanics of composite materials. Courier Corporation; 2012.
[48] Norouzifard V, Bahrami M. Deformation of PEM fuel cell gas diffusion layers under compressive loading: An analytical approach. Journal of Power Sources 2014;264:92–9.
[49] El Oualid S, Lachat R, Candusso D, Meyer Y. Characterization process to measure the electrical contact resistance of Gas Diffusion Layers under mechanical static compressive loads. International Journal of Hydrogen Energy 2017;42:23920–31.
[50] Gigos PA, Faydi Y, Meyer Y. Mechanical characterization and analytical modeling of gas diffusion layers under cyclic compression. International Journal of Hydrogen Energy 2015;40:5958–65.
[51] Carral C, Mele P. Modeling the original and cyclic compression behavior of non-woven gas diffusion layers for fuel cells. Submitted to the International Journal of Hydrogen Energy. n.d.
[52] Meng L, Zhou P, Yan Y, Guo D. Compression properties of gas diffusion layers and its constitutive model under cyclic loading. International Journal of Hydrogen Energy 2021;46:15965–75. https://doi.org/10.1016/j.ijhydene.2021.02.083.

Chapter III: Determination of the static and kinetic friction coefficients between the catalyst layer and the microporous layer; influence of the MEA components and its assembly conditions.

To complete the previous experimental study focused on the mechanical behavior of the GDL, this next chapter will deal about the overall mechanical behavior of the MEA. In this section, a new insight is brought to provide further understanding of the MEA interfacial mechanical properties. The continuation of this work will thus consist in evaluating the friction coefficient between MEA layers, for several configurations. Different MEA samples were used by, first, varying the nature of the layers forming it, and second, the process used for its assembly.

First, a new experimental setup was developed to determine the static and kinetic friction coefficients between the different components of the MEA. Second, a morphological analysis was conducted to evaluate the microstructural properties of the different layers.

This part of the study brings a new insight to the MEA interfacial characterization from a tribological perspective in order to predict the potential wear that might take place between the core's layers.

Determination of the static and kinetic friction coefficients between the catalyst layer and the microporous layer; influence of the MEA components and its assembly conditions

Marwa Ouerghemmi[a], *Christophe* Carral[a], Jean François Blachot[b] and Clémence Marty[b], *Antoine Dumain[a], Patrice* Mele[a]

Univ. Grenoble Alpes, Univ. Savoie Mont Blanc, CNRS, Grenoble INP, LEPMI, Grenoble, 38000, France
CEA, LITEN, 38000 Grenoble Cedex 9, France

I. Abstract:

Membrane electrode assembly (MEA) is composed of mainly five principal layers: two gas diffusion layers on top of two catalyst layers surrounding the membrane. It is crucial to maintain a strong cohesion between these layers to ensure good fuel cell performance and increase durability. The understanding of the mechanical behavior at the different interfaces is therefore essential and will be the subject of this study through the development of a new methodology to evaluate the friction coefficients between the different layers and then to analyze the impact of the nature of the MEA components and its assembly process. A morphological analysis based on confocal microscopy observations of the catalyst layer / macro porous layer (MPL) interface has been conducted for a qualitative and quantitative study of the surface through roughness measurements. The static friction increased with the presence of macro porous layers and catalyst layers but remained stable for the different membranes. A higher value of friction coefficient is observed for the hot pressed MEAs compared to the non-assembled ones. Finally, it was found that roughness decreases with the assembly process under the combined action of heat and pressure, as well as, and under friction test.

II. Introduction:

As proton exchange membrane fuel cells (PEMFC) are taking the lead in green energy, multiple researches have been focused, in recent years, on improving its performances and durability [1–16]. For this purpose, the degradation phenomena have been the focal point of multiple studies in order to better understand the degradation mechanisms and thus prevent them.

The primary cause of PEMFC failure is the aging of its core [1,17–24], the membrane electrode assembly (MEA), which is a crucial place where the electrochemical reactions take place. It is commonly composed of 5 layers: a membrane, surrounded by the catalyst layers and the gas diffusion layers (GDL). Sublayers can also be considered, as for example the macro porous layer (MPL) of the GDL, and the different layers of reinforced membranes. This architecture implies a large number of interfaces that can be the seat of damage or failure and alter the performance and durability of the fuel cell.

Among the different causes behind the reduction of PEMFC performance, stresses induced by the MEA assembly process or during operation could lead to the delamination of the different layers of the MEA related to the generation and then propagation of cracks [25–28], which leads to ohmic losses and contact resistance increase. It is therefore essential to observe and analyze in detail the behavior of the MEA components and the properties at interfaces during its operation or assembly, and to identify the failure mechanisms propagating either within the materials or at the level of the different interfaces.

In this context, different studies were conducted in order to investigate the microstructural change at the MEA layers interfaces under the cycling of start-up and shut-down of PEMFC during operation [25,29–32]. Most of the studies have shown that due to ionomer degradation, the interface between the CL and the membrane could be altered, this could be at the origin of flooded areas causing the loss of apparent catalytic activity and increasing the risk of the CL peeling off the electrolyte. Consequently, the active surface is reduced and the degradation of the fuel cell is expected [4,25,33]. Cracks and delamination in the CLs are the potential candidate for initiating and accelerating the local membrane degradation phenomena due to the loss of local reinforcement [22–25,34].

Therefore, numerous studies were oriented towards finding a solution to limit the degradation mechanisms. For example, pressure uniformity was determined to be a key parameter to mitigate MEA physical damage [35]. Consequently, a high GDL stiffness was found to be helpful for applying a more uniform pressure as it helps mitigate the freeze-induced physical damage of the membrane such as surface cracks [29].

It is clear that the microstructural change at interfaces is one of the main causes of the cell's damage but understanding the origin behind the creation of these degradation mechanisms is still object of research.

Some pioneering studies have conducted experimental tests in order to investigate the mechanical properties at the MEA interfaces.

Jia *et al.* [36] performed fracture test using Double Cantilever Beam (DCB) testing method to study the internal separation of a catalyst coated membrane (CCM) under ambient conditions. They observed a cohesive fracture in the CL during all the tests which proves that there is a stronger cohesion between the CL/membrane interface compared to the CL breaking strength, for a CCM process.

The same result was reported on a recent research by Byun *et al*. [37], via the optimized SAICAS method (Surface And Interfacial Cutting Analysis System) performed on CCM. The adhesive strength at the interface between the cathode and the membrane was approximately eight-fold higher than the average cohesive strength within the bulk regions of the cathode, due to the high degree of intermolecular diffusion of ionomer binders.

De Moor *et al.* [38] have conducted tensile tests on 5 layers MEA, with a CCB (Catalyst Coated Backing) process, *i.e.* the CL was deposited on the GDLs prior to the assembly of

the 5 layers forming the MEA. The mechanical responses of whole MEAs were compared to the one of the membranes, allowing the extraction of damage criteria by measuring the decohesion energy at the membrane/electrodes interface. The same tests have been conducted on aged samples revealed a decrease in the decohesion energy with the hydro-thermal ageing time. It was found that the force required to shear the membrane/electrode interface becomes lower with the ageing time, one of the causes being the accumulated plastic strain at the membrane/electrode interface resulting in fatigue solicitation due to the hygrothermal cycles.

Uchiyama *et al*. [39] measured the static friction coefficient between a CCM and a GDL (25BC) having a macro porous layer (MPL) and investigated its impact on the deformation of the MEA under several moisture cycles. The static friction coefficient between the MEA and the MPL was measured by the flat ball method. The study shows that the static friction coefficient increases from 0.25 to 0.85 when the contact pressure increases from 0.15 to 0.60 MPa.

In conclusion, only a few studies are available on the topic of MEA interfacial mechanical characterization, showing that the interface between the CL and its substrate of deposition (membrane for CCM, GDL for CCB) seems to be cohesive and is not at the origin of the interface degradation initiation. However, the interface created during the assembly process of the MEA (CCM/GDL or CCB/membrane) seems to be the weakest, with almost no cohesive strength. There is still a lack of information when it comes to studying this latter interface, where the first damages occur due to a possible relative sliding of the components during the fuel cell operation.

The aim of this work is thus to provide a further understanding of the MEA interfacial mechanical properties, and in particular on the interface created during the whole MEA assembly (CL/MPL).

The friction measurement turns out to be a convenient test to characterize interfaces with no cohesive strength. A measurement method was then developed to determine the static and kinetic friction coefficients between the different components of the MEA. It allows to obtain quantified values of the mechanical strength of the interfaces. A complementary morphological analysis was, afterwards, conducted to examine the change in the surface microstructure before and after friction, and was useful to quantify the real contact surface between the layers in order to evaluate the real normal pressure.

By selecting the appropriate components composing the MEA, we were able to analyze the influence of each components of the MEA and its assembly process on the global interfacial mechanical strength.

This study brings a new insight to the MEA interfacial characterization from a tribological perspective in order to predict the potential wear that might take place between the core's layers.

III. Experimental details

1. Materials

i. MEA components

Figure 1 shows the different layers of a MEA and the interface MPL/CL which will be the subject of this study.

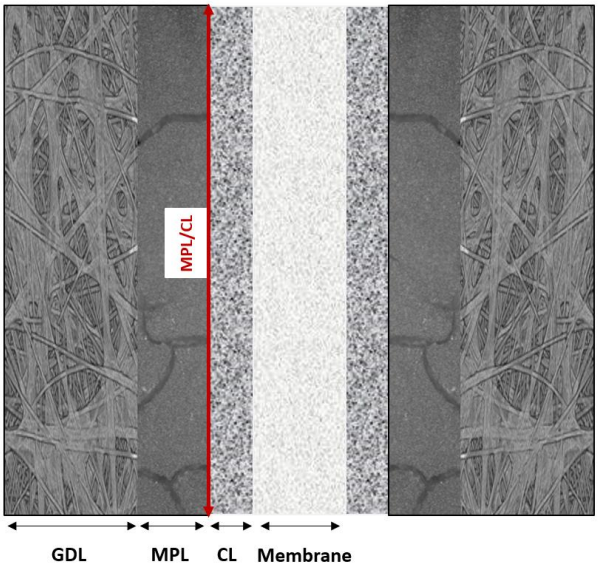

Figure 1: *MEA layers and the studied interface.*

The coefficient of friction was measured between several references of GDL and membranes following 4 main configurations (***Table 1***) in order to analyze the MEA components impact on the properties of interfaces. Configurations without CL were studied to perform a thorough analysis of the friction coefficients between all layers of the MEA.

For GDLs, two roll types references have been selected: the 22BB, and 29AA from SGL Carbon, respectively with and without MPL. Tests were conducted in both machine (MD) and cross machine (CD) directions but the impact of the fiber and the MPL orientation was found to be insignificant.

For MEA without CL, simple (Nafion 211) and reinforced (Nafion XL) membrane samples were used. Gore membrane was used for membrane with CL.

A CL was deposited on the membrane to form a CCM, it should be noted that, with this process, good contact between the catalyst layer and the electrolyte membrane is ensured, which can effectively reduce the catalyst loading without compromising the cell performance, ensures higher active area and thus better performances [40,41]. The same catalyst provided by Tanaka, with the reference TEC 10V50E was used for both electrodes, with a load of 0.1mg/cm^2 for the anode, 0.2mg/cm^2 for the cathode. The 2 layers being linked by the ionomer D2020 from Chemours with a ratio I/C of 0.7.

Table 1: *List of studied MEA configurations.*

Configuration	MPL	CL
(a)	No	No
(b)	Yes	No
(c)	Yes	Yes

ii. Five layers MEA process assembly conditions

The hot-pressing process of the five layers of the MEA (***Figure 2***) is important to conform the surfaces to obtain a good contact between the layers. Different parameters are to control and to optimize the assembly procedure. For that matter, a couple of combination between the parameters were used (***Table 2***) following soft (Process 1) and extreme (Process 2) conditions. Friction tests were then carried out on the different MEAs.

To ease the analysis of the effect of the assembly process and its parameter, the same components as configuration (c) as indicated in ***Table 1*** were employed.

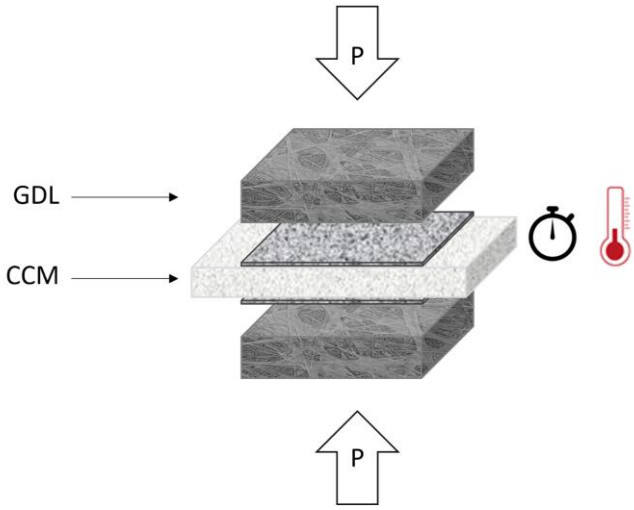

Figure 2: *schematic representation of the hot-pressing process of the 5 layers MEA.*

Table 2: *List of MEA assembly processes and main parameters studied.*

Process	Pressure (MPa)	Temperature (°C)	Duration (s)
No process	0	0	0
1	0.08	145	180
2	1	145	180

2. Friction measurement experimental set up

The coefficient of friction is defined as the ratio between the tangential force (FT) and the normal force (FN) between two surfaces in contact (ISO 8295):

$$\mu = \frac{FT}{FN} \qquad (1)$$

The friction coefficient between the different components of the MEA was measured using the test described in Figure 3; it is performed on a Shimadzu ASG machine with a 5kN load cell and a displacement speed of 5 mm/min.

To perform the tests, two MEAs of dimensions 15x15 mm^2 were glued on both sides of a rigid support (0.8 mm thick steel plate) and on the two jaws using a double-sided adhesive tape (Figure 3 (a)). The adhesive reference is PT931 from Adezif company, composed of acrylic and silicone and its thickness is equal to 70µm. A specific value of normal force is applied on the samples, controlled via the manometer of the pneumatic jaws. The force measured during the test via the load cell corresponds to the tangential force, i.e. the force that is transmitted by the different interfaces of the MEA. The evolution of this parameter is illustrated in ***Figure 3b***, where the tangential force increases up to a certain limit value, then decreases and follows a plateau. The first part of the curve, *i.e.* before reaching the maximum value of the tangential force, corresponds to a quasi-static state, where no relative displacement occurs between the different layers. From this peak onwards, slippage occurs at the interface with the lowest interlayer adhesion, which will be referred to as the kinetic phase in the following. Two specific values of the tangential force could then be extracted from the curve: (i) FT_S which is the maximum value, linked to the static coefficient of friction μ_s, and (ii) FT_K which is the tangential force of the plateau. To accurately estimate FT_K and then μ_k, a method based on plotting the tangents upstream and downstream of the plateau is employed (see ***Figure 3b***).

The determination of these two coefficients of friction is then carried out from tests on pristine samples with different levels of normal force, ranging from 10 to 110N with a step of 20N, corresponding to an apparent normal pressure ranging from 0.04 to 0.5 MPa. A linear increase of FT_S and FT_K with FN can be observed in ***Figure 3c***, demonstrating that that the friction coefficients are independent of the applied normal force, in agreement with friction theory [42]. Values of the static μ_s and kinematic μ_k friction coefficients are then determined from the slopes of the linear regressions of the curves FT_S=f(FN) and FT_K=f(FN), respectively.

A preliminary study showed that the measurement of the friction coefficients was independent of the apparent contact surface (***Figure 4***), confirming the principle that the real contact pressure is independent of the apparent contact pressure and the normal force applied on the samples [42].

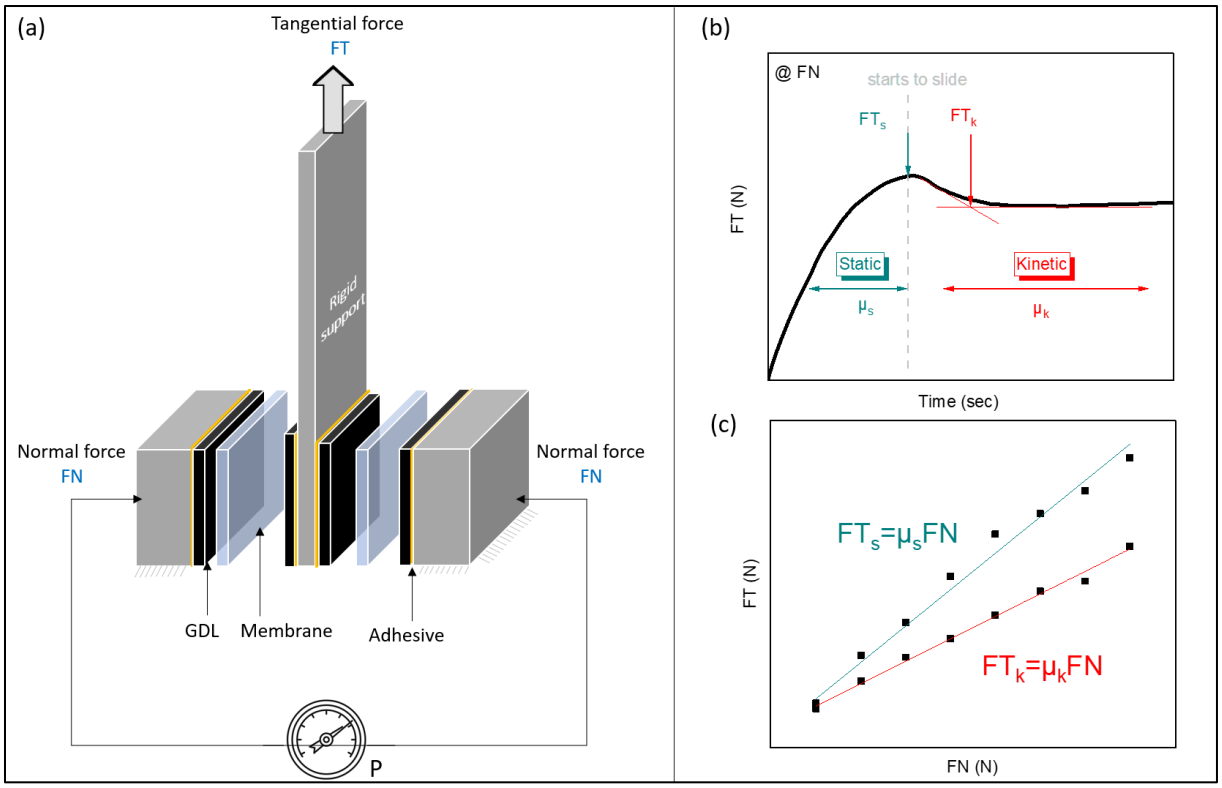

Figure 3: *Schematic representation of (a) the friction measurement, (b) the tangential force (FT) measurement during the test and (c) the determination method of the friction coefficients.*

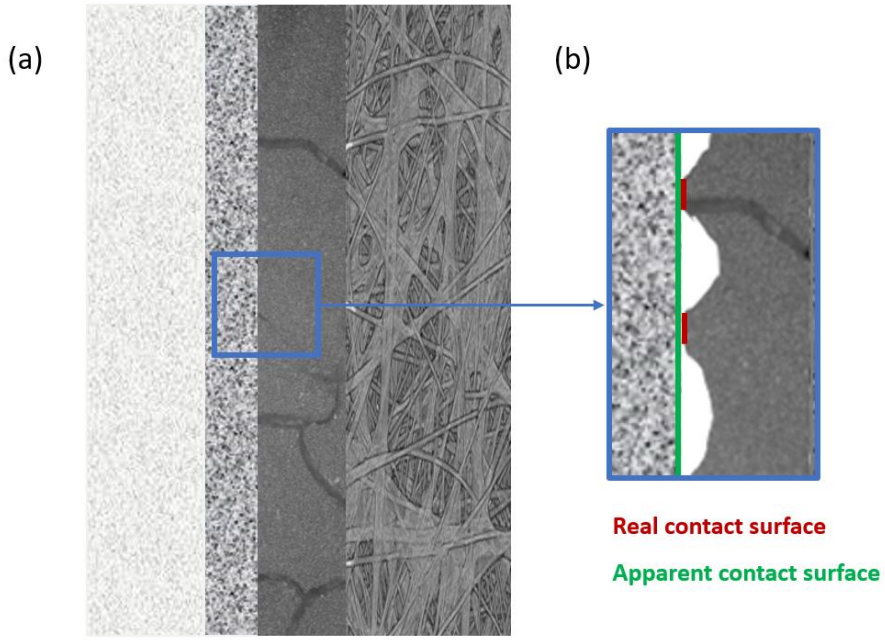

Figure 4: *(a) ½ MEA layers and (b) difference between apparent and real contact surfaces.*

IV. Results

1. Friction coefficients measurements

i. Influence of the MEA components

To study the impact of each material, the effect of each component is separately investigated, starting by studying the effect of the GDL (fiber part) on the membrane, then the MPL and finally the active layer.

Figure 5 presents the friction measurements curves between the MEA layers (GDL, MPL, CL and membrane) following the method described above and for the 3 mentioned configurations.

For all configurations the normal force applied goes from 10N to 110N, and it should be noted that the sliding occurs between the GDL (fiber part) and the membrane for configuration (a); between MPL and membrane for configuration (b); and between MPL and CL for configuration (c). From these configurations the maximum tangential force is extracted for every level of FN applied as well as the value corresponding to the plateau at the end of the curve according to the method described in Figure3 (b). The static and kinetic friction coefficients between the previous layers are afterwards calculated via a linear regression between the extracted values of forces (***Figure 6***).

It was observed that the maximum tangential force increases with the normal force applied, the average FT_s goes from 7N to almost 170N when the normal force FN increases from 10N to 110N all configurations included. The same applies to the kinetic force FT_k, the latter going from 5N to 114N for the same normal force levels (***Figure 5***).

Higher levels of tangential forces are obtained after adding the MPL and CL. The highest level of tangential force is observed for configuration (c) corresponding to the addition of CL. Under FN=110N, Ft_s reaches almost 170N. Moreover, higher displacement is observed through the shift in the curves peaks starting from configuration (b) corresponding to the addition of MPL at first.

The linear correlation coefficient (***Figure 6***) is sufficiently high (equals to 0.99 for all configurations) to prove the high linear dependency between the tangential and normal forces.

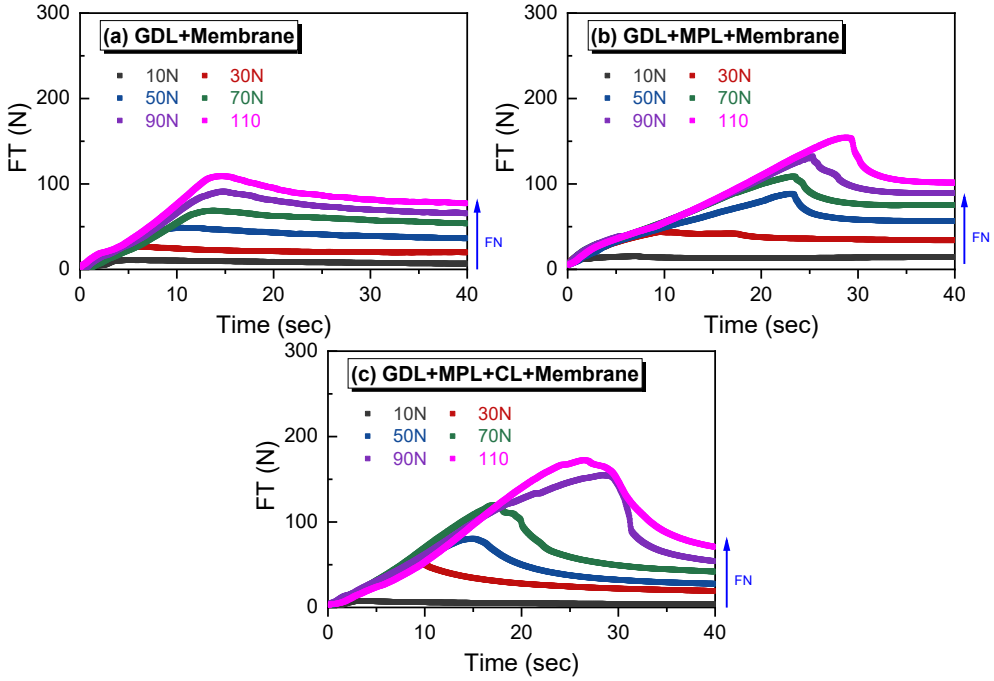

Figure 5: *Friction curves for the MEA different configurations (a) GDL+Membrane, (b) GDL+MPL+Membrane, and (c) GDL+MPL+CL+Membrane.*

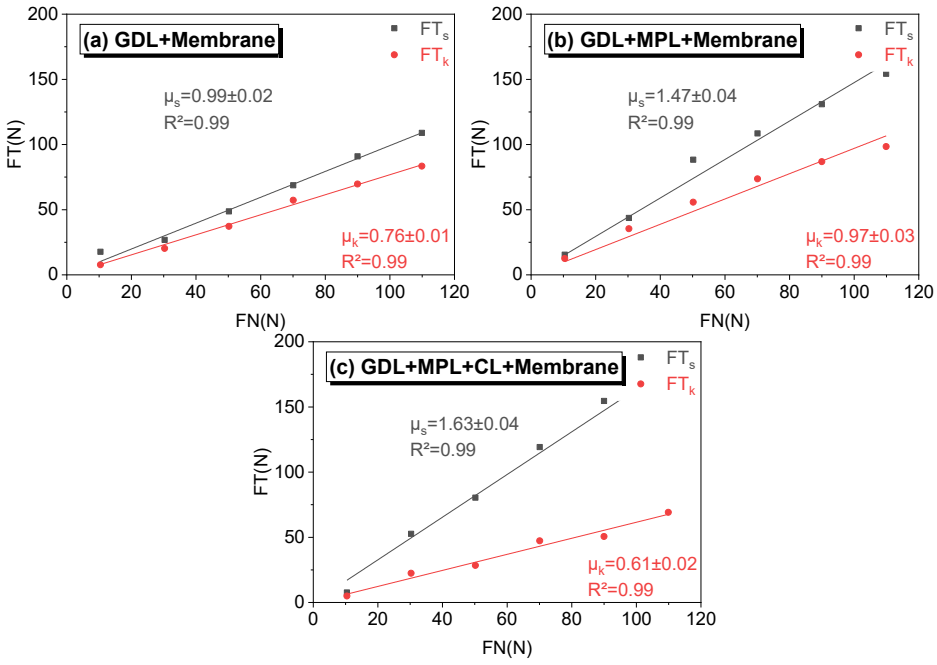

Figure 6: *Static and kinetic friction coefficients determination via the linear regression for the MEA different configurations (a) GDL+Membrane, (b) GDL+MPL+Membrane, and (c) GDL+MPL+CL+Membrane.*

Figure 7 presents the friction coefficients evolution for all configurations, the detailed values are summarized in ***Table 3***.

The first main change occurs after adding the MPL which increase both coefficients, μ_s goes from 1 to 1.4 and μ_k from 0.7 to 0.9, this is also approved by the higher tangential

forces obtained after adding the MPL first and the CL afterwards. This implies that there is a stronger adhesion between MPL surface compared to the fiber part of the gas diffusion layer with the membrane. The same observation can be made with the addition of CL, where μ_s increases from 1.4 to 1.6, however the kinetic coefficient decreases from 0.9 to 0.6, a morphological analysis, at this scale, is necessary to explain this variation (see the following section).

Given that the tests were performed on non-assembled samples and after finding the impact of MPL and the CL that add a higher cohesive strength to the membrane and gas diffusion layer interface, the assembly process impact will be discussed in the next part.

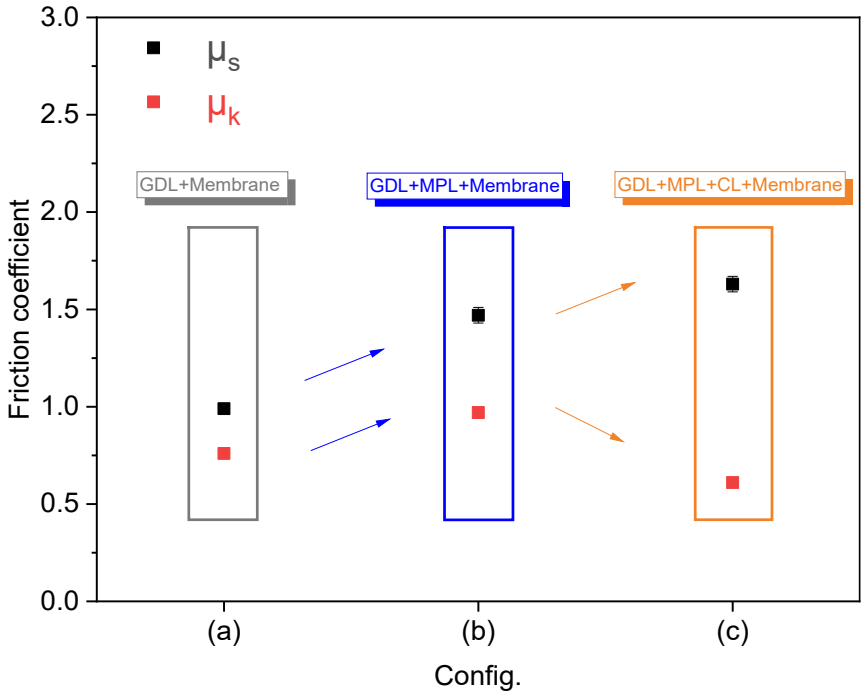

Figure 7: *Impact of the MEA components on the static and kinetic friction coefficients.*

Table 3: *Static and kinetic friction coefficients for the different MEA configurations (with no assembly process).*

Configuration	MPL	CL	μ_s	μ_k
(a)	No	No	0.99±0.02	0.76±0.01
(b)	Yes	No	1.47±0.04	0.97±0.03
(c)	Yes	Yes	1.63±0.04	0.61±0.02

ii. Influence of the assembly process

The objective of this part is to investigate the impact of the MEA assembly process on the friction coefficients and thus provide information on the quality of the interfaces between the layers. The variation of FT versus time for are presented in ***Figure 8***. It should be

noted that tests are performed on the heat-bonded surfaces following the five layers MEA process assembly conditions without proceeding to any separation of the layers before the friction test.

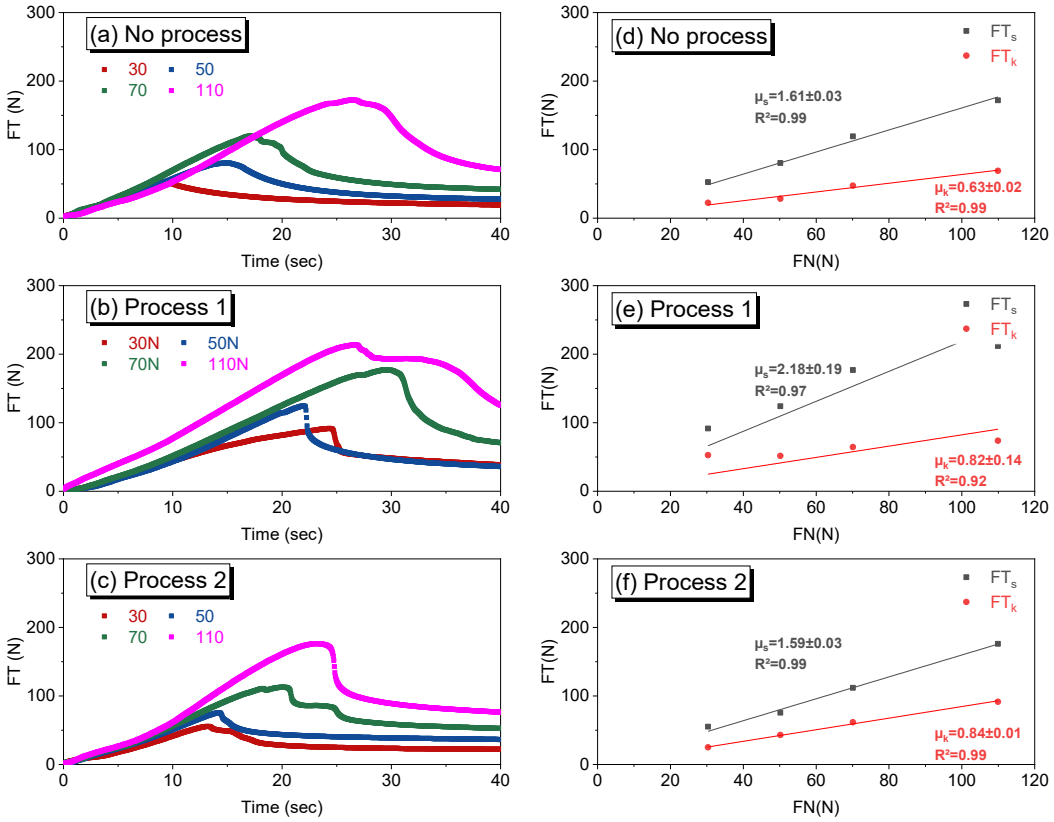

Figure 8: *Friction curves for MEA 22BB-CCM (a) No process (b) Process 1(P=0.08 MPa) and (c) Process 2 (P=1MPa).*

The friction coefficients for the assembled MEA is higher compared to the non-assembled one, μ_s increases from to 1.6 to 2 and μ_k goes from 0.6 to 0.8 (***Figure 9***).

In fact, the assembly process helps promote good contact between MEA layers, the objective is to have a real contact surface as closer as possible to the nearly perfect apparent surface (***Figure 4***), which can explain the higher friction coefficients due to the higher FT values induced by the increased inter-layer contact area by the assembly process.

A more detailed analysis of the observed values of the friction coefficients will be made in the following section.

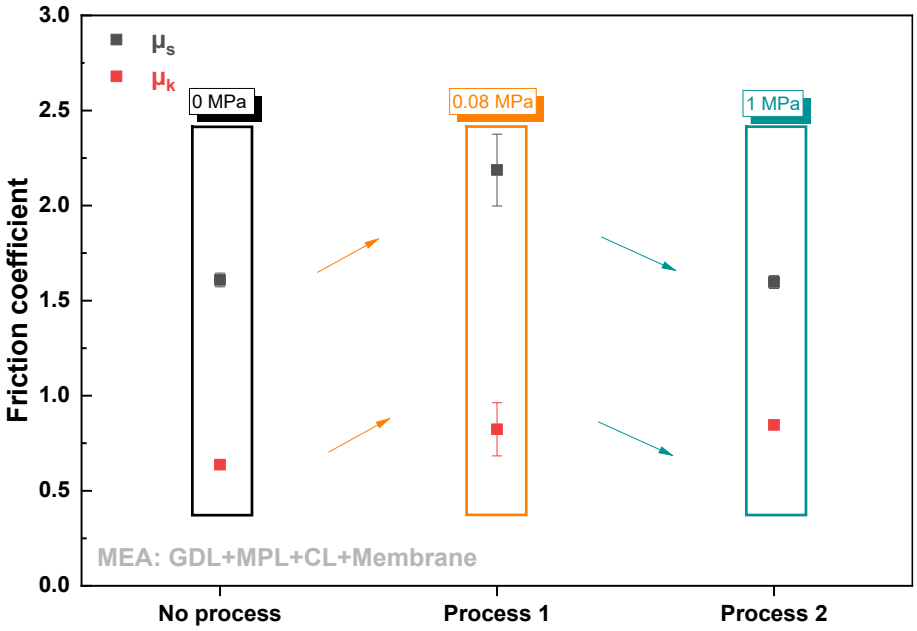

***Figure 9**: Impact of assembly process on the static and kinetic friction coefficients.*

***Table 4:** Static and kinetic friction coefficients for the different process configurations.*

Process	Pressure (MPa)	Temperature	Duration	μ_s	μ_k
No process	0	0	0	1.61±0.03	0.638±0.02
1	0.08	145	180	2.18±0.19	0.82±0.14
2	1	145	180	1.59±0.03	0.84±0.01

2. Morphological analysis

i. MEA with no assembly process

Figure 10 presents optical observations to illustrate the variation of the MPL surface throughout the friction tests. The combined action of compression and tangential force, polishes the surface of the MPL, making it reflective, in fact roughness is generally associated with dullness, as the normal force increases, the carbon black particles are scraped and asperities are crushed which makes the surface shinier as it is seen in the microscopic observations.

The surface is more reflective as the normal force applied is more important, it is clearly shown on the optical microscope observation, comparing the blanc sample that didn't undergo a friction test, to the one under FN=50N, after this value, almost the entire surface is scraped, which proves that the contact surfaces are perfectly overlapped.

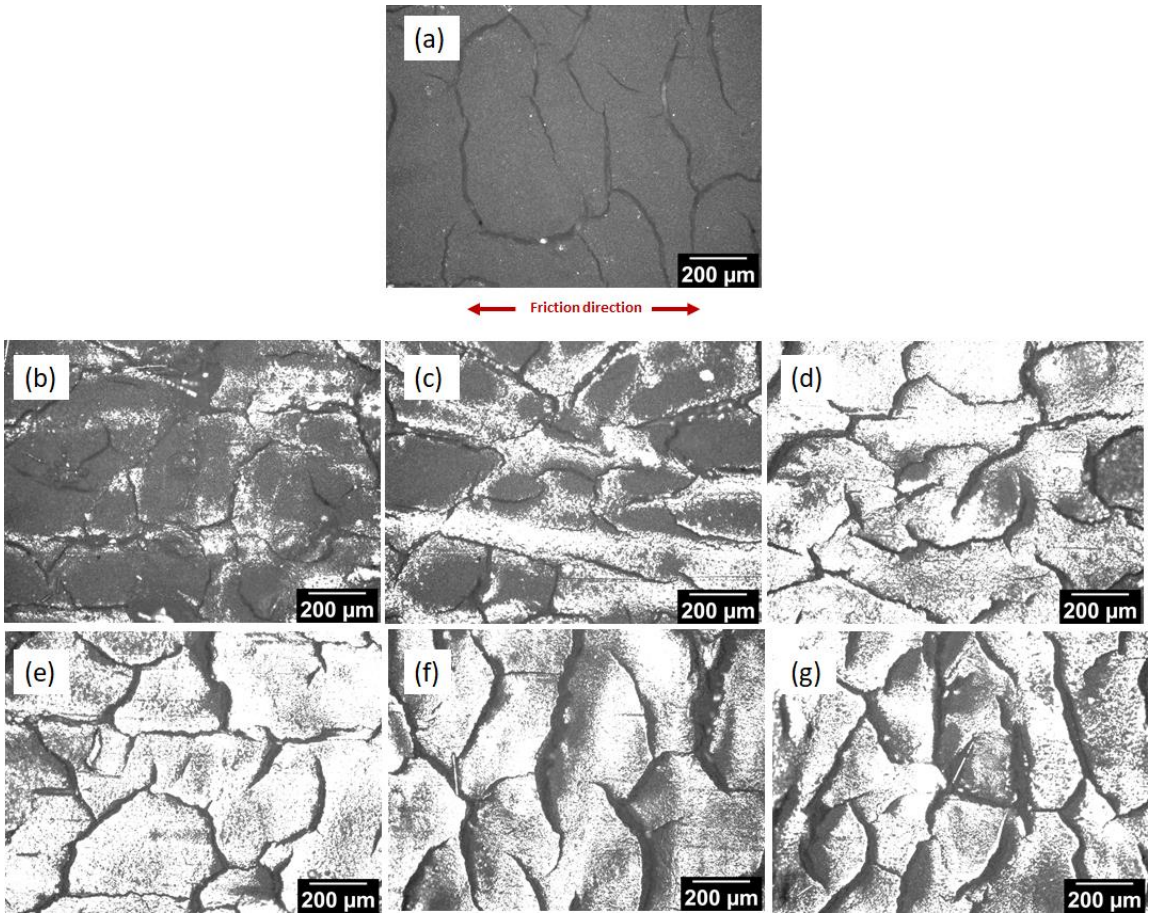

***Figure 10**: Optical microscope observations of (a) blank MPL surface; and morphological change in the MPL surface after friction test under a normal force of (b) 10N, (c) 30N, (d) 50N, (e) 70N, (f) 90N, (g) 110N.*

ii. MEA with assembly process

In the case of the hot pressed MEA, the cohesion between the interfaces is more important, the surface is reflective under the weaker normal force applied (***Figure 11)***, compared to the non-assembled MEA (***Figure 10***), and wrinkles appeared on the surface of the MPL throughout the test. Under high levels of compression (>110N) portions of the MPL peel off from the GDL surface leading to a cohesive breakage of The GDL (***Figure 11***) and above 150N the cohesion is so important that no sliding between the interfaces is possible. This can be confirmed with the membrane surface morphology for the hot-pressed MEA, it is shown that the membrane conforms to the shape of the MPL under the assembly process which leads to higher adherence (***Figure 12***).

The same applies to the membrane/CL interface, the surface of the membrane is smooth, the 3-layer membrane is composed of a PTFE layer as a reinforcement matrix sandwiched between two layers of PFSA ionomer. When subjected to a hot-pressing process, the membrane surface conforms to the shape of the CL surface under the dual action of heat and pressure. ***Figure 13*** presents cross sectional view of a neat membrane with a smooth surface (***Figure 13a***), the figure shows that this same surface presents some micro-roughnesses when assembled with a catalyst layer (***Figure 13b***).

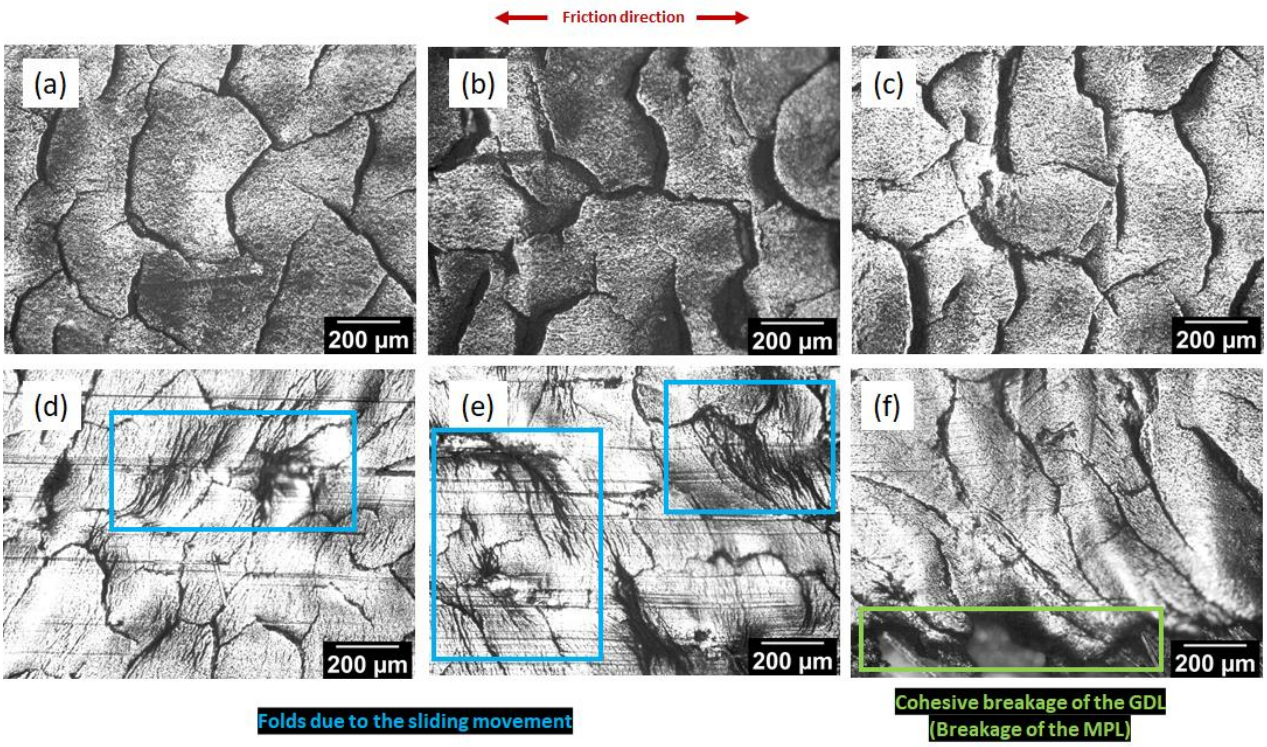

Figure 11 : *Optical microscope observations of the morphological change in the MPL surface after friction test under a normal force of (a) 10N, (b) 30N, (c) 50N, (d) 70N, (e) 90N, (f) 110N.*

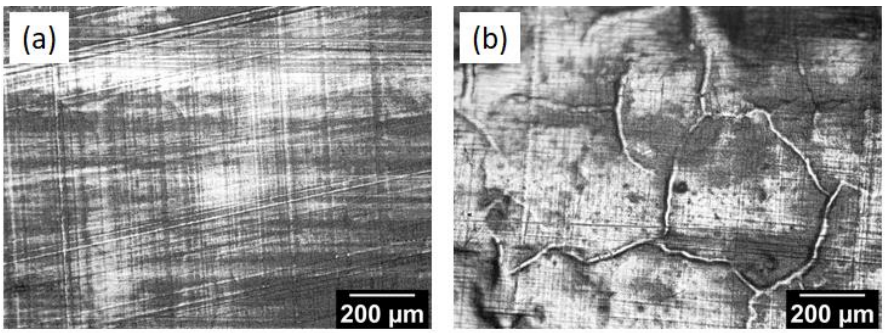

Figure 12: *Optical microscope observations of (a) CCM with no assembly process, and (b) hot pressed CCM after friction test under a normal force of 10N.*

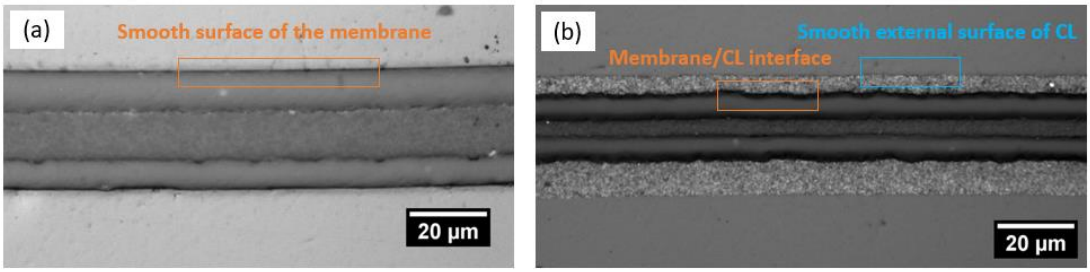

Figure 13: *Optical observations of (a) a membrane without catalyst layer and (b) a membrane with a catalyst layer assembled following the CCM process.*

The roughness of MPL can decrease under both an assembly process or the friction test, as seen in the confocal microscope observations in ***Figure 14*** . The assembly process leads

to the crushing of the asperities under the combined action of pressure and heat. The friction test induces a scraping of the surface leading to the asperities trimming.

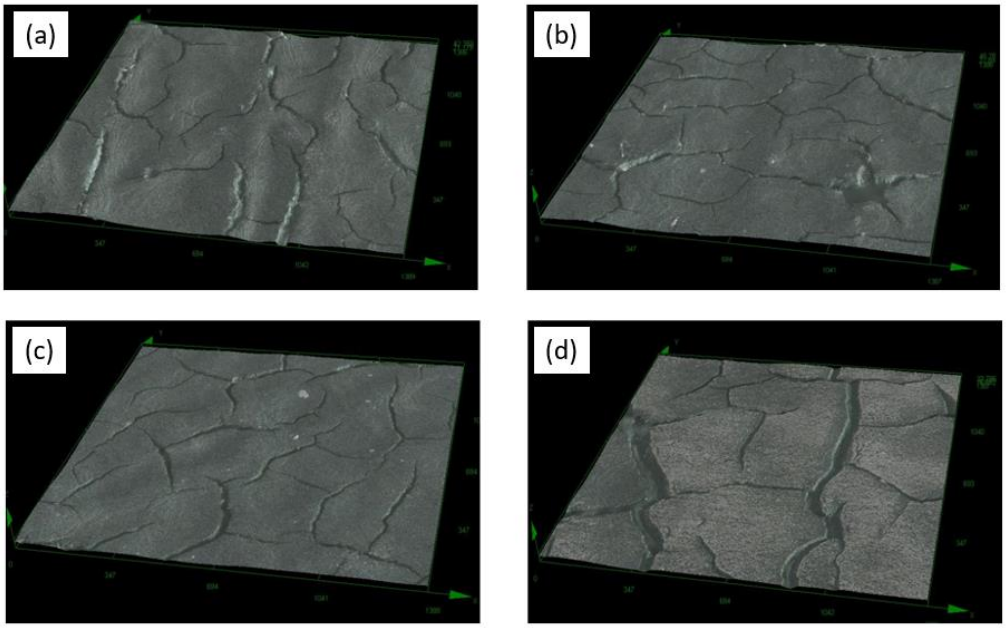

Figure 14: *Confocal microscope observations of (a) blank MPL sample; (b) MPL subjected to Process1 before friction test; (c) MPL subjected to Process 2 before friction test and (d) MPL subjected to Process 1 after friction test.*

These results are confirmed with roughness measurements via confocal microscope. The values are presented in pixel in ***Table 5***.

Without undergoing any friction test, the surface roughness Ra of MPL is first equal to 4.5, it decreases to 3.8 and 2.7 when subjected to MEA assembly process under pressure values of 0.08 MPa and 1 MPa respectively. Asperities on the MPL surface would crush under pressure leading to a smoother surface.

Table 5*: Roughness measurements with confocal microscope of (a) blank MPL sample; (b) MPL subjected to Process1 before friction test; (c) MPL subjected to Process 2 before friction test and (d) MPL subjected to Process 1 after friction test.*

Configuration	**(a)**		**(b)**		**(c)**		**(d)**	
	Ra_x	**Ra_y**	**Ra_x**	**Ra_y**	**Ra_x**	**Ra_y**	**Ra_x**	**Ra_y**
	5,2	3,7	4,4	3,3	2,7	2,6	3,7	3,5
	Ra_{moy}		**Ra_{moy}**		**Ra_{moy}**		**Ra_{moy}**	
	4,5		3,8		2,7		3,6	

To better understand the link between the friction coefficients and the roughness values, the phenomenon is illustrated in the following ***Figure 15***.

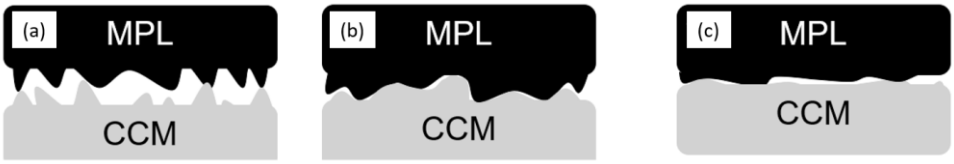

Figure 15*: Illustration of the MPL/CCM interface for (a) blank sample; (b) sample subjected to soft process (Process 1) and (c) sample subjected to extreme process (Process 2)*

In fact, if no assembly process is applied, both MPL and the membrane surface have asperities, after undergoing soft process (Process1), more contact points are created without crushing the asperities, which explains the higher friction coefficient. If the layers are subjected to more extreme process (Process2), asperities are crushed, and the surface becomes smoother, hence, the lower friction coefficient values.

V. Conclusion

This study allowed the development of a method for measuring the friction coefficient between the different layers of a fuel cell core, i.e. between the MPL, the CL and the membrane. Different types of material assemblies were tested to validate the methodology and obtain first results.

It was shown the static friction coefficient does not vary with the contact pressure, contrary to studies found in the literature, it was determined from a linear regression between the different tangential force points plotted against the different applied normal forces.

First, the impact of the MEA components were studied, it was found that adding the MPL and the CL leads to higher adhesion between the layers, as the friction coefficient depends on the nature of the surfaces in contact, higher friction coefficient is, thus, obtained.

The second part of the studies investigates the assembly process of the MEA on the frictional properties between its layers. The study is conducted through the same friction measurements followed by a morphological analysis of the different samples before and after friction. It was shown that a soft process (0.08MPa pressure) leads to higher friction coefficient (adhesion) between the layers, however, extreme conditions (1MPa pressure) has to the opposite effect.

In fact with pressure applied during assembly process better contact between layers is obtained, when using a low pressure (0.08MPa) asperities are not totally crushed which explains the increase in the friction coefficient for the first configuration, furthermore, when the pressure used is much higher, (1MPa), not only higher contact is obtained but also roughness is reduced due to the crushing of more asperities on the surface, the latter becomes smoother which explains the lower friction coefficient under extreme assembly process.

References

[1] Borup R, Meyers J, Pivovar B, Kim YS, Mukundan R, Garland N, et al. Scientific Aspects of Polymer Electrolyte Fuel Cell Durability and Degradation. Chem Rev 2007;107:3904–51. https://doi.org/10.1021/cr050182l.

[2] Chang WR, Hwang JJ, Weng FB, Chan SH. Effect of clamping pressure on the performance of a PEM fuel cell. Journal of Power Sources 2007;166:149–54. https://doi.org/10.1016/j.jpowsour.2007.01.015.

[3] Zhou Y, Lin G, Shih AJ, Hu SJ. A micro-scale model for predicting contact resistance between bipolar plate and gas diffusion layer in PEM fuel cells. Journal of Power Sources 2007;163:777–83. https://doi.org/10.1016/j.jpowsour.2006.09.019.

[4] de Bruijn FA, Dam VAT, Janssen GJM. Review: Durability and Degradation Issues of PEM Fuel Cell Components. Fuel Cells 2008;8:3–22. https://doi.org/10.1002/fuce.200700053.

[5] Zhang S, Yuan X, Wang H, Merida W, Zhu H, Shen J, et al. A review of accelerated stress tests of MEA durability in PEM fuel cells. International Journal of Hydrogen Energy 2009;34:388–404. https://doi.org/10.1016/j.ijhydene.2008.10.012.

[6] Yim S-D, Kim B-J, Sohn Y-J, Yoon Y-G, Park G-G, Lee W-Y, et al. The influence of stack clamping pressure on the performance of PEM fuel cell stack. Current Applied Physics 2010;10:S59–61. https://doi.org/10.1016/j.cap.2009.11.042.

[7] Taymaz I, Benli M. Numerical study of assembly pressure effect on the performance of proton exchange membrane fuel cell. Energy 2010;35:2134–40. https://doi.org/10.1016/j.energy.2010.01.032.

[8] Park J, Oh H, Ha T, Lee YI, Min K. A review of the gas diffusion layer in proton exchange membrane fuel cells: durability and degradation. Applied Energy 2015;155:866–80.

[9] Wang J. System integration, durability and reliability of fuel cells: Challenges and solutions. Applied Energy 2017;189:460–79. https://doi.org/10.1016/j.apenergy.2016.12.083.

[10] Dafalla AM, Jiang F. Stresses and their impacts on proton exchange membrane fuel cells: A review. International Journal of Hydrogen Energy 2018;43:2327–48. https://doi.org/10.1016/j.ijhydene.2017.12.033.

[11] Toghyani S, Moradi Nafchi F, Afshari E, Hasanpour K, Baniasadi E, Atyabi SA. Thermal and electrochemical performance analysis of a proton exchange membrane fuel cell under assembly pressure on gas diffusion layer. International Journal of Hydrogen Energy 2018;43:4534–45. https://doi.org/10.1016/j.ijhydene.2018.01.068.

[12] Khetabi EM, Bouziane K, Zamel N, François X, Meyer Y, Candusso D. Effects of mechanical compression on the performance of polymer electrolyte fuel cells and analysis through in-situ characterisation techniques - A review. Journal of Power Sources 2019;424:8–26. https://doi.org/10.1016/j.jpowsour.2019.03.071.

[13] Ozden A, Shahgaldi S, Li X, Hamdullahpur F. A review of gas diffusion layers for proton exchange membrane fuel cells—With a focus on characteristics, characterization techniques, materials and designs. Progress in Energy and Combustion Science 2019;74:50–102. https://doi.org/10.1016/j.pecs.2019.05.002.

[14] Bouziane K, Khetabi EM, Lachat R, Zamel N, Meyer Y, Candusso D. Impact of cyclic mechanical compression on the electrical contact resistance between the gas diffusion layer and the bipolar plate of a polymer electrolyte membrane fuel cell.

Renewable Energy 2020;153:349–61.
https://doi.org/10.1016/j.renene.2020.02.033.
[15] Shahgaldi S, Ozden A, Li X, Hamdullahpur F. A scaled-up proton exchange membrane fuel cell with enhanced performance and durability. Applied Energy 2020;268:114956. https://doi.org/10.1016/j.apenergy.2020.114956.
[16] Li B, Wan K, Xie M, Chu T, Wang X, Li X, et al. Durability degradation mechanism and consistency analysis for proton exchange membrane fuel cell stack. Applied Energy 2022;314:119020. https://doi.org/10.1016/j.apenergy.2022.119020.
[17] Stanic V. Mechanism of Pinhole Formation in Membrane Electrode Assemblies for PEM Fuel Cells. Proc Vol 2004;2004–21:391–401.
https://doi.org/10.1149/200421.0391PV.
[18] Husar A, Serra M, Kunusch C. Description of gasket failure in a 7 cell PEMFC stack. Journal of Power Sources 2007;169:85–91.
https://doi.org/10.1016/j.jpowsour.2007.01.078.
[19] Chatenet M, Guilminot E, Iojoiu C, Sanchez J-Y, Rossinot E, Maillard F. Pt Redistribution within PEMFC MEAs and its Consequence on their Performances. ECS Trans 2007;11:1203–14. https://doi.org/10.1149/1.2781034.
[20] De Moor G, Bas C, Charvin N, Moukheiber E, Niepceron F, Breilly N, et al. Understanding Membrane Failure in PEMFC: Comparison of Diagnostic Tools at Different Observation Scales. Fuel Cells 2012;12:356–64.
https://doi.org/10.1002/fuce.201100161.
[21] Uchiyama T, Kato M, Yoshida T. Buckling deformation of polymer electrolyte membrane and membrane electrode assembly under humidity cycles. Journal of Power Sources 2012;206:37–46. https://doi.org/10.1016/j.jpowsour.2012.01.073.
[22] Kai Y, Kitayama Y, Omiya M, Uchiyama T, Kato M. Crack Formation in Membrane Electrode Assembly Under Static and Cyclic Loadings. Journal of Fuel Cell Science and Technology 2013;10:021007. https://doi.org/10.1115/1.4023878.
[23] Singh Y, Khorasany RMH, Sadeghi Alavijeh A, Kjeang E, Wang GG, Rajapakse RKND. Ex situ measurement and modelling of crack propagation in fuel cell membranes under mechanical fatigue loading. International Journal of Hydrogen Energy 2017;42:19257–71. https://doi.org/10.1016/j.ijhydene.2017.06.151.
[24] Singh Y, Khorasany RMH, Kim WHJ, Alavijeh AS, Kjeang E, Rajapakse RKND, et al. Ex situ characterization and modelling of fatigue crack propagation in catalyst coated membrane composites for fuel cell applications. International Journal of Hydrogen Energy 2019;44:12057–72.
https://doi.org/10.1016/j.ijhydene.2019.03.108.
[25] Kundu S, Fowler MW, Simon LC, Grot S. Morphological features (defects) in fuel cell membrane electrode assemblies. Journal of Power Sources 2006;157:650–6.
https://doi.org/10.1016/j.jpowsour.2005.12.027.
[26] Tsushima S, Hirai S. An overview of cracks and interfacial voids in membrane electrode assemblies in polymer electrolyte fuel cells. JTST 2015;10:JTST0002–JTST0002. https://doi.org/10.1299/jtst.2015jtst0002.
[27] Uzundurukan A, Bilgili M, Devrim Y. Examination of compression effects on PEMFC performance by numerical and experimental analyses. International Journal of Hydrogen Energy 2020;45:35085–96.
https://doi.org/10.1016/j.ijhydene.2020.04.275.
[28] Ramani D, Khattra NS, Singh Y, Orfino FP, Dutta M, Kjeang E. Mitigation of mechanical membrane degradation in fuel cells – Part 2: Bonded membrane

electrode assembly. Journal of Power Sources 2021;512:230431. https://doi.org/10.1016/j.jpowsour.2021.230431.
[29] Kim S, Ahn BK, Mench MM. Physical degradation of membrane electrode assemblies undergoing freeze/thaw cycling: Diffusion media effects. Journal of Power Sources 2008;179:140–6. https://doi.org/10.1016/j.jpowsour.2007.12.114.
[30] Hiramitsu Y, Mitsuzawa N, Okada K, Hori M. Effects of ionomer content and oxygen permeation of the catalyst layer on proton exchange membrane fuel cell cold start-up. Journal of Power Sources 2010;195:1038–45. https://doi.org/10.1016/j.jpowsour.2009.08.016.
[31] Alavijeh AS, Khorasany RMH, Nunn Z, Habisch A, Lauritzen M, Rogers E, et al. Microstructural and Mechanical Characterization of Catalyst Coated Membranes Subjected to In Situ Hygrothermal Fatigue. J Electrochem Soc 2015;162:F1461–9. https://doi.org/10.1149/2.0471514jes.
[32] Li L, Wang S, Yue L, Wang G. Cold-start icing characteristics of proton-exchange membrane fuel cells. International Journal of Hydrogen Energy 2019;44:12033–42. https://doi.org/10.1016/j.ijhydene.2019.03.115.
[33] Huang X, Solasi R, Zou Y, Feshler M, Reifsnider K, Condit D, et al. Mechanical endurance of polymer electrolyte membrane and PEM fuel cell durability. J Polym Sci B Polym Phys 2006;44:2346–57. https://doi.org/10.1002/polb.20863.
[34] Tavassoli A, Lim C, Kolodziej J, Lauritzen M, Knights S, Wang G, et al. An experimental study on local thinning and pinhole formation phenomena in PEM fuel cell membranes. ECS Meeting Abstracts, IOP Publishing; 2014, p. 1091.
[35] Lim S-J, Park G-G, Park J-S, Sohn Y-J, Yim S-D, Yang T-H, et al. Investigation of freeze/thaw durability in polymer electrolyte fuel cells. International Journal of Hydrogen Energy 2010;35:13111–7. https://doi.org/10.1016/j.ijhydene.2010.04.079.
[36] Jia R, Dong S, Hasegawa T, Ye J, Dauskardt RH. Contamination and moisture absorption effects on the mechanical properties of catalyst coated membranes in PEM fuel cells. International Journal of Hydrogen Energy 2012;37:6790–7. https://doi.org/10.1016/j.ijhydene.2012.01.063.
[37] Byun S, Yu J-H, Choi J, Yun S, Roh Y, Dzakpasu CB, et al. Unraveling the cohesive and interfacial adhesive strengths of electrodes for automotive fuel cells. Journal of Power Sources 2020;455:227928. https://doi.org/10.1016/j.jpowsour.2020.227928.
[38] De Moor G, Bas C, Lesage F, Danérol AS, Claude E, Rossinot E, et al. Understanding the degradation of MEA in PEMFC: Definition of structural markers and comparison between laboratory and on-site ageing. J Appl Polym Sci 2011;120:3501–10. https://doi.org/10.1002/app.33506.
[39] Uchiyama T, Kumei H, Yoshida T, Ishihara K. Static friction force between catalyst layer and micro porous layer and its effect on deformations of membrane electrode assemblies under swelling. Journal of Power Sources 2014;272:522–30.
[40] Cheng X, Yi B, Han M, Zhang J, Qiao Y, Yu J. Investigation of platinum utilization and morphology in catalyst layer of polymer electrolyte fuel cells 1999:7.
[41] Passos RR, Paganin VA, Ticianelli EA. Studies of the performance of PEM fuel cell cathodes with the catalyst layer directly applied on Nafion membranes. Electrochimica Acta 2006;51:5239–45. https://doi.org/10.1016/j.electacta.2006.01.044.
[42] Hutchings I, Shipway P. Tribology: friction and wear of engineering materials. Butterworth-Heinemann; 2017.

Chapter IV: Impact of material and interfaces properties on the mechanical response of PEM under hygro-thermal loading: Numerical study

This last chapter aims to synthesize all the experimental work previously carried out, via a numerical analysis.

A numerical 1D model was developed on MATLAB to simulate the mechanical state of the MEA under the compression of the gas channel rib. The real orthotropic properties and non-linear behavior of GDL ware implemented. The membrane elastoplastic behavior with its hygrothermal dependency, and the interfaces properties of the MEA were also integrated.

First the impact of the material properties was investigated, and second, the interfacial nature between the MEA layers. All with the goal to investigate the mechanical response of the membrane under assembly load and hygrothermal operating condition.

Impact of material and interfaces properties on the mechanical response of PEM under hygro-thermal loading: Numerical study

Marwa Ouerghemmi, *Christophe* Carral, and *Patrice* Mele

Univ. Grenoble Alpes, Univ. Savoie Mont Blanc, CNRS, Grenoble INP, LEPMI, Grenoble, 38000, France

I. Abstract:

The deformation of the membrane electrode assembly (MEA) layers has a huge impact on the performances of the fuel cell (PEMFC) as it affects the transport properties, but it is also a crucial indicator for the cell lifetime, if damage occurs to any of the components. The goal of this study is to provide an understanding of the impact of the hygrothermal loading, mechanical stresses due to assembly process, the GDL properties and the properties of the interfaces on the mechanical degradation of the membrane. This study suggests that it may be possible to control the plastic strain of the membrane by controlling the clamping method and the properties at interfaces. Hence, better mechanical endurance is obtained, potentially enhancing the durability of fuel cell membranes.

II. Introduction:

PEMFC is a promising device for clean energy transition, among multiple assets, it helps reduce pollution and has high efficiency. The assembly process of a PEMFC is at the origin of mechanical constraints, which have an impact on the performance and the durability of the cell. Therefore, in order to optimize the performance of PEMFCs, the first problem of assembly technique research is to determine a reasonable assembly load range [1,2].

Poor assembly load leads to incomplete contact between components, resulting in high interface contact resistance. On the contrary, excessive assembly compression would seriously damage the GDL leading to lower porosity and permeability [3–5] inducing reactant diffusion inhibition as well as water management disruption [6]. In fact, even if the assembly load were reduced, there would be some residual stresses in the membrane, which would lead to a serious deterioration in the durability of the cell [7], because even when controlling the initial pressure, the interface contact pressure could surge significantly, owing to the swelling of the membrane under operating condition [8,9].

In the literature, several research on PEMFC assembly techniques turned to numerical studies on the stack in order to analyze the effect of the assembly compression on each component in addition to the properties at interfaces [8,10,11]. Different modelling approaches were thus conducted.

Finite element model has been used by Tang *et al*. [12] to investigate the hygro-thermal stresses in a cell assembly caused by temperature and relative humidity change assuming a linear elastic behavior for the membrane.

Later on, Kusoglu *et al.* [13,14] brought added value to simulate the mechanical behavior of the membrane under several hygrothermal loading and unloading cycles representative of the cell operation. The stress evolution during a simplified operating cycle is determined using a 2D finite element model according to two clamping methods. In particular, they showed that compressive plastic deformation occurs in the plane of the membrane during hygrothermal loading, resulting in residual tensile stresses in the membrane after unloading. These stresses are considered a contributing factor to the mechanical failures observed in the membranes.

Solasi *et al.* [15] found that water absorption/dehydration of the membrane would lead to PEM further expansion/contraction under the original assembly load. They discussed PEM failure modes by establishing a durability model of the PEM, this result confirms with other research [16–18] that the mechanical behavior of the membrane is highly dependent on the hygrothermal conditions.

Other studies focused on the pressure distribution [19,20] it was shown that the stresses distribution in the membrane is not uniform; this could mainly be caused by the difference in stiffness between the surrounding layers of the membrane, creating localized stress areas would further constraint the membrane and leads to its breakage.

Moreover, the GDL is also affected during assembly process of a PEMFC, due to its porous structure and weak stiffness. Several studies focused on investigating the GDL behavior using different numerical models.

In numerical studies, its behavior is investigated using different models, it can be considered either isotropic [1,8,14,19,21–23], isotropic transverse [24] or orthotropic [25–28].

In general, linear isotropic models are not accurate and cannot describe the inhomogeneous behavior of GDL under compression. In fact, the GDL's behavior is confirmed to be not linear in compression and the orthotropic character of the GDL is likely the closest to the microstructure of the porous material [29–31,28,32–36].

For simplifications purposes several researches assumed a linear isotropic model for GDL, to study the GDL properties such as the elastic modulus, as well as the impact of the GDL properties on the other components, the objective being to optimize the structures and control the level of stresses and strains that might appear. For example, this linear isotropic model was used to analyze GDL intrusion [22], to predict the contact resistance at the interface between BPP and GDL [21,8], to study the contact pressure distribution [19,23,1] and to investigate the membrane deformation [13,14,19].

Only few studies used the orthotropic model to characterize the GDL [25–28], although it is the closest model to the real physical state of GDL, due to the complexity of measuring its properties.

The mechanical behavior of GDL was characterized in flexural, shear and compression tests to determine the in plane elastic modulus, in plane shear modulus, and through-plane behavior. Data were then used in a finite element-based numerical model to calculate the channel intrusion of the GDL [37].

A study by Kleemann *et al.* [28] employed the orthotropic material model with plane strain assumption to analyze both the mechanical and electrical behaviors of GDL, its properties were experimentally determined and were used in another research to study the combined action of assembly and hygrothermal loading on GDL intrusion and stress distribution via a nonlinear orthotropic material [38].

Firat et *al.* [27] used the nonlinear orthotropic material to model the GDL's behavior, but they only employed the through-plane elastic modulus and not the through-plane shear modulus of GDL.

Polynomial fitting method was also used to describe the nonlinear mechanical behavior of GDL, in order to investigate the GDL properties and the contact pressure distribution under different compression levels [25,39].

To encompass all the work previously mentioned, a recent study by Leng *et al.* [40] compares the impact of using an isotropic or orthotropic model on the GDL properties and thus on the transport functions in the PEMFC.

The influences of different GDL material models on the accuracy of numerical simulation results were investigated, it was found that the orthotropic model and the parameters utilized are more effective in analyzing the deformation of GDL compared to the isotropic one.

Another aspect considered in few numerical studies is the interfacial properties. For example, non-uniform stress distribution, was found to induce localized bending stresses, which may contribute to delamination between the membrane and the GDL [12,41]. Hence, water management could be affected due to interfacial gaps between the MEA layers which would lead to the transport functions disruption. In the study of Bajpai *et al.* [42], a two-dimensional, thermal, anisotropic numerical model was developed to investigate the effect of true interfacial morphology between the MPL and CL on fuel cell performance. The model shows a decrease in the performances if an interface layer is considered. The inclusion of interface layer causes water infiltration between layers and a decrease in the conductivity. Zenyuk *et al.* [43] also confirmed the same statement via an elastic deterministic contact mechanics model that is applied to the compressed micro-porous and catalyst layer interfaces in polymer electrolyte fuel cells (PEFCs).

In conclusion, modelling the mechanical behavior of the whole MEA during fuel cell operation is challenging. It includes anisotropy, non-linearity (material mechanical

response, plasticity, etc.), interfaces and contacts, thermal expansion and swelling. Furthermore, the material properties of the membrane is strongly affected by the temperature and humidity induced by the fuel cell operation. Developing numerical models integrating all these parameters is still a remaining issue. 2D Tooth/channel finite elements models are commonly used, however the complexity of integrating specific material and contact properties in finite element analysis leads to strong hypothesis such as isotropic linear behaviors for all the components or not considering the interfacial changes.

Based thereon, a numerical model was developed on MATLAB able to simulate the mechanical state of the MEA under the compression of the gas channel rib. This numerical model is based on an analytical approach completed with routines to integrate the non-linearities of the MEA mechanical response. This equivalent 1D model allows then to integrate the anisotropic behavior of GDL, the membrane elastoplastic behavior with its hygrothermal dependency, and the interfaces properties of the MEA. Comparisons with existing numerical analysis [14] shows that this equivalent model provides nearly identical results as a finite element model. This model is then employed to investigate the impact of the material properties as well as the interfacial nature between the MEA layers on the mechanical response of the membrane under assembly load and hygrothermal operating condition. First the impact of the GDL material properties is analyzed by considering the different GDL types (rolls, sheet, felt). The nature of the interfaces (bonded or free) is then investigated. For all configurations, the two main assembly mode (fixed force or fixed displacement) is taken into consideration. The results allow to define the most influent parameters on the membrane mechanical damages and thus the mitigation strategies.

III. Model parameters:

1. Geometry

The equivalent analytical model was developed in MATLAB based on the literature [12–14]. ***Figure 1*** shows the schematics of the numerical model studied. The model consists of a BPP, one GDL and a membrane.

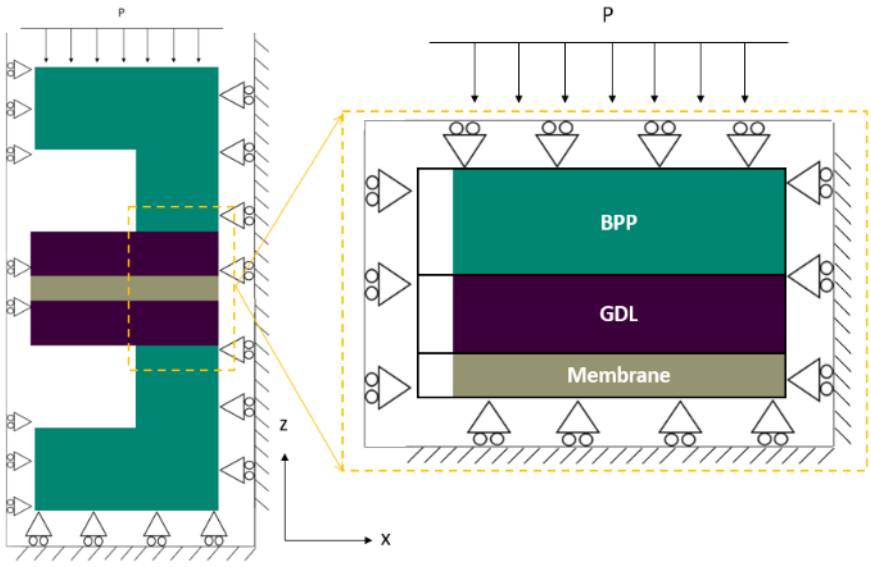

Figure 1: *Schematics of a 2D tooth/channel model (left) and the 1D equivalent model of this study (right).*

2. Boundary conditions

Out-of-plane boundary conditions (z direction)

Two clamping methods are used to investigate the assembly conditions of the stack.

1- Fixed force: a constant pressure of 2 MPa is applied on the BPP (***Figure 2***), this value corresponds to the assembly pressure often used to ensure good performances [44,45].

2- Fixed displacement: a constant displacement of -0.005 mm resulting of a 2MPa pressure load is applied

In-plane boundary conditions (x-y directions)

Two in plane conditions are investigated in this study, linked to the interfaces properties; (i) the first one assumes a bonded contact between the layers and is obtained by applying a fixed in-plane displacement of 6.10^{-5} mm, following the one of the bipolar plates (***Figure 2a***).
(ii) The second one assumes a free in-plane displacement which would allow the sliding between the layers (***Figure 2b***).

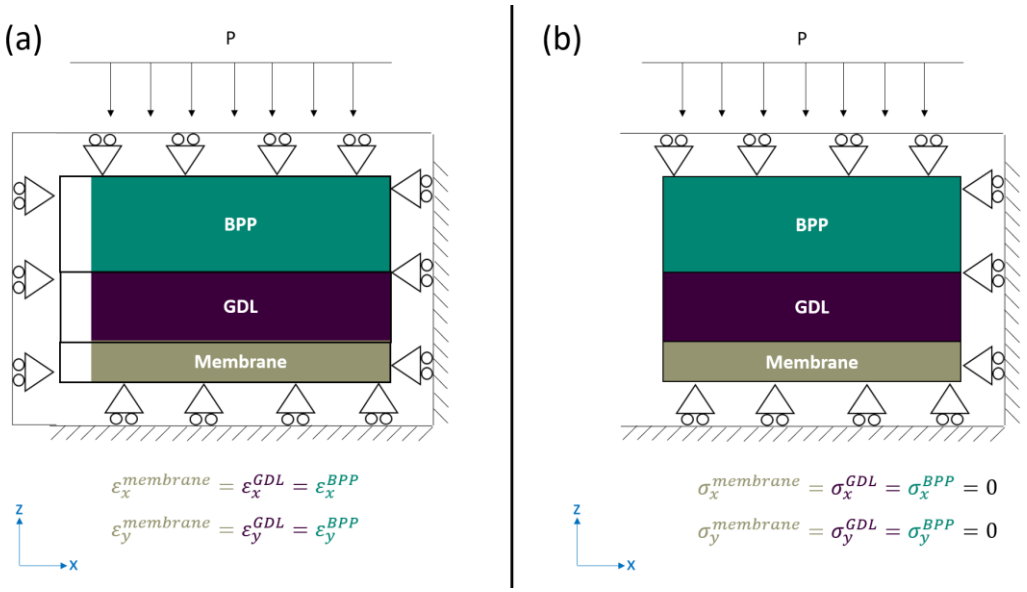

Figure 2: *In-plane boundary conditions: (a) bonded interfaces (GDL and membrane displacements following the one of the BPP) (b) sliding interfaces.*

Hygrothermal loading

Figure 3 describes the profile of the hygrothermal loading for 5 cycles as described in the study of Kusoglu et al [14], the loading phase consists in increasing linearly and simultaneously, the humidity rate from 30% to 95% and the temperature from 20°C to 85°C, and unloading is obtained by getting back to the initial hygrothermal values (RH=30% and T=85°C). For multiple cycles, the temperature remains fixed at 85°C all along the hygrothermal cycling and only decreases to 20°C at the final unloading phase of the last cycle.

It should be noted that the clamping conditions are fixed all along the loading/unloading phases of the hygrothermal cycles and that the membrane is assumed to be the only component to swell under hygrothermal loading.

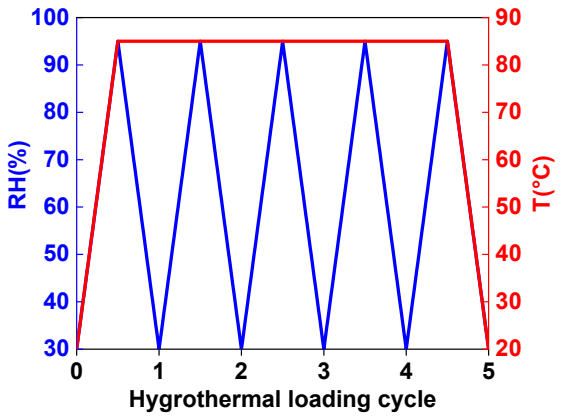

Figure 3*: Hygrothermal loading cycles.*

3. Materials model behavior

The material models describe the mechanical behavior of the different materials, considering elasticity, plasticity, thermal expansion and swelling. The total strain tensor is then considered as follow:

$$\varepsilon_{ij} = \varepsilon_{ij}^{e} + \varepsilon_{ij}^{pl} + \varepsilon_{ij}^{Th} + \varepsilon_{ij}^{S} \quad (1)$$

where ε_{ij}^{e} is the elastic strain component, ε_{ij}^{pl} is the plastic strain component and ε_{ij}^{Th} and ε_{ij}^{S} are the temperature and swelling induced strains, respectively.

Isotropic Linear elasticity:

Hooke's law is used to link the elastic strain and stress tensors in the elastic domain:

$$\sigma_{ij} = \frac{E}{(1+v)(1-2v)}[v\delta_{ij}\varepsilon_{kk}^{e} + (1-2v)\varepsilon_{ij}^{e}] \quad (2)$$

where, $\varepsilon_{kk} = \varepsilon_{xx} + \varepsilon_{yy} + \varepsilon_{zz}$, E is the Young's modulus, v is the Poisson's ratio, δ_{ij} the Kronecker symbol.

Isotropic transverse linear elasticity:

A linear transversely isotropic material is a special class of orthotropic materials. It has the same properties in one plane (e.g. the x-y plane) and different properties in the direction normal to this plane (e.g. the z-axis), the latter is the thickness direction in our case. It is fully defined by five independent non-zero elastic constants, components of the stiffness or compliance tensor. The relationship between the deformation tensor and the stress tensor using the matrix of compliance coefficients [46]:

$$\begin{bmatrix} \varepsilon_{xx} \\ \varepsilon_{yy} \\ \varepsilon_{zz} \\ \gamma_{yz} \\ \gamma_{zx} \\ \gamma_{xy} \end{bmatrix} = \begin{bmatrix} \frac{1}{E_x} & -\frac{v_{xy}}{E_x} & -\frac{v_{xz}}{E_x} & 0 & 0 & 0 \\ -\frac{v_{xy}}{E_x} & \frac{1}{E_x} & -\frac{v_{xz}}{E_x} & 0 & 0 & 0 \\ -\frac{v_{xz}}{E_x} & -\frac{v_{xz}}{E_x} & \frac{1}{E_z} & 0 & 0 & 0 \\ 0 & 0 & 0 & \frac{2(1+v_{xy})}{E_x} & 0 & 0 \\ 0 & 0 & 0 & 0 & \frac{1}{2G_{xz}} & 0 \\ 0 & 0 & 0 & 0 & 0 & \frac{1}{2G_{xz}} \end{bmatrix} \begin{bmatrix} \sigma_{xx} \\ \sigma_{yy} \\ \sigma_{zz} \\ \sigma_{yz} \\ \sigma_{zx} \\ \sigma_{xy} \end{bmatrix} \quad (3)$$

where E_x and E_z are the elasticity moduli of the material respectively in and out of plane; v_{xy} is the in-plane Poisson's ratio and G_{xz} is the out-of-plane shear modulus.

Linear Elastoplasticity:

Incompressible plastic deformation is assumed for the plastic response, with the rate-independent plastic flow according to the Von Mises yield criterion (J2-flow theory) [14,47]:

$$f(\sigma_{ij}) = \sqrt{\frac{3}{2} S_{ij} S_{ij}} - \sigma_0 \tag{4}$$

Where σ_{ij} are the components of the true stress tensor, σ_0 the yield strength and S_{ij} are the components of the stress tensor deviator defined as follows:

$$S_{ij} = \sigma_{ij} - \frac{1}{3}\sigma_{kk}\delta_{ij} \tag{5}$$

The incremental theory of plasticity, well detailed in the literature [47] is employed in the simulations to determine the plastic strain. The material is assumed to exhibit isotropic hardening; thus, the yield strength depends on the plastic strain and the hygrothermal conditions (***Table 3***). The magnitude of the plastic strain of the membrane $\bar{\varepsilon}^{pl}$ is obtained as follows:

$$\bar{\varepsilon}^{pl} = \int \sqrt{\frac{2}{3} d\varepsilon_{ij}^{pl} d\varepsilon_{ij}^{pl}} \tag{6}$$

The elastic domain is defined for $f(\sigma_{ij}) < 0$ The plastic strain increment tensor is proportional to the deviatoric stress tensor:

$$d\varepsilon_{ij}^{pl} = d\bar{\varepsilon}^{pl} \frac{\partial f(\sigma_{ij}, \bar{\varepsilon}^{pl})}{\partial \sigma_{ij}} = d\bar{\varepsilon}^{pl} \frac{3}{2} \frac{S_{ij}}{\sigma_0} \tag{7}$$

Two new parameters, on top of the one needed for elasticity (E, ν) are added to constitute the elastoplastic model: the initial yield strength (σ_y), defining the elastic stress limit, and the elastoplastic tangent modulus (E_{ep}), defining the material stiffness in the elastoplastic domain.

Thermal expansion

The thermal strains resulting from a change in temperature are given by:

$$\varepsilon_{ij}^{Th} = \alpha(T - T_0)\delta_{ij} \tag{8}$$

with α the linear coefficient of thermal expansion, T_0 the reference temperature and T the actual one.

Swelling

The swelling strains are directly obtained from the experimental measurements (see next section Material Properties)

4. Material properties

- **BPP:**

The BPP is considered as a purely isotropic elastic material with thermal expansion. The corresponding material properties are described in ***Table 1***.

- **Membrane:**

The membrane is considered as an isotropic elastoplastic material with thermal expansion and swelling.

The properties established by Kusoglu *et al*. [14] from the experimental work of Tang *et al*. [48] are used in this study and described thereafter.

The material properties needed for the thermoelastic behavior of the membrane are described in ***Table 1***.

Table 1: *Thermoelastic properties of the BPP and the membrane [14,48].*

Material	Reference	Thickness	E	ν	α
		µm	MPa		10^{-6} K^{-1}
BPP	Graphite	2200	10 000	0.25	5
Membrane	Nafion112®	50	E= f (T, RH)	0.25	123

The Young's modulus is considered as dependent of the temperature and humidity via linear interpolation of experimental measurements described in ***Table 2***.

Table 2: Experimental data of Young's modulus of the membrane (*Nafion112™*) at different temperatures and humidity *[48].*

	Young's modulus (MPa)			
	RH=30%	*RH=50%*	*RH=70%*	*RH=90%*
T=25°C	197	192	132	121
T=45°C	161	137	103	70
T=65°C	148	117	92	63
T=85°C	121	85	59	46

For the elastoplastic domain, the yield strength values are presented in ***Table 3***.

Table 3: Experimental data of yield stress at plastic strains of 0%, 5% and 25% of the membrane (*Nafion112™*) at different temperatures and humidity rate *[48].*

Yield strength σ_y (MPa)

$\varepsilon^{pl} = 0$	*RH=30%*	*RH=50%*	*RH=70%*	*RH=90%*
T=25°C	6.76	6.51	5.66	4.20
T=45°C	5.67	5.1	5.01	3.32
T=65°C	5.14	4.58	4.16	2.98
T=85°C	3.61	3.44	3.08	2.20
ε^{pl}	*RH=30%*	*RH=50%*	*RH=70%*	*RH=90%*
T=25°C	7.16	6.61	6.22	5.11
T=45°C	5.70	5.72	5.43	3.69
T=65°C	5.30	4.77	4.36	3.33
T=85°C	4.16	3.62	3.16	2.26
ε^{pl}	*RH=30%*	*RH=50%*	*RH=70%*	*RH=90%*
T=25°C	9.71	9.26	8.65	8.88
T=45°C	7.31	7.34	7.48	6.18
T=65°C	6.55	5.92	5.73	5.78
T=85°C	5.04	4.28	4.22	4.31

The swelling of the membrane is directly obtained with a third-degree polynomial

$$\varepsilon^s(T, RH) = \sum_{i,j=1}^{4} C_{ij} T^{4-j} H^{4-i} \tag{9}$$

where C_{ij} are the constants of the polynomial and given in ***Table 4***.

Table 4*: Constants for the swelling strain polynomial defined in equation (4).*

C_{ij}	***i=1***	***i=2***	***i=3***	***i=4***
j=1	2.994×10^{-12}	-5.221×10^{-10}	3.574×10^{-8}	-6.832×10^{-7}
j=2	-4.303×10^{-10}	7.361×10^{-8}	-5.166×10^{-6}	1.003×10^{-4}
j=3	2.163×10^{-8}	-3.566×10^{-6}	2.564×10^{-4}	-5.067×10^{-3}
j=4	-5.402×10^{-8}	2.012×10^{-5}	2.007×10^{-3}	4.355×10^{-2}

Table 5 presents the breaking stress of the membrane, calculated from the average values in the machine (MD) and cross machine (CD) directions from experimental work of Tang *et al.* [48]. The breaking stress is almost independent of the humidity rate, therefore, only the temperature variation is considered. These values will be used to establish a damage parameter of the membrane (see section results).

Table 5: *Experimental data of breaking stress of the membrane (Nafion112™) at different temperatures [48].*

	T=25°C	T=45°C	T=65°C	T=85°C
Breaking stress σ_b (MPa)	18.4	16.6	13.6	10.6

- **GDL:**

The GDL is considered as an elastic isotropic transverse material. The thermal expansion of this layer is not considered as the thermal coefficient in each plane was experimentally measured as close to 0 in our laboratory.

Three different types of GDL were used in this study. The properties of the different GDL are described in ***Table 6***. They were determined through a large campaign of experimental in- and out-of-plane characterizations [49].

The modulus in the transverse direction E_z is varying with the pressure applied, as detailed by Carral et Mele [35]. Two roll GDLs with an identical thickness of 250µm were chosen. As observed in ***Figure 4***, a non-linear behavior is observed, with an increase of the stiffness with the compression strain. A difference of behavior can however be observed between the two GDLs; the GDL-A shows a higher stiffness than the GDL-B. An inflection point can be observed graphically at a compression value of 3 MPa, which, as mentioned by the authors, could indicate the pressure value applied during its manufacturing process.

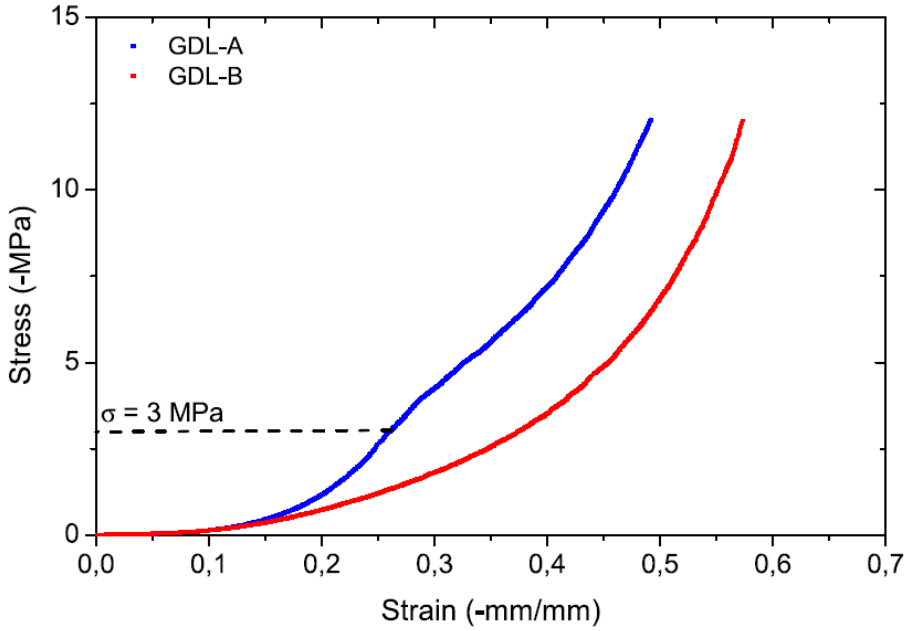

Figure 4: *GDLs stress-strain curves. Pristine samples [35].*

***Table 6**: The physical properties of the materials used in the isotropic transverse model*

GDL type	Reference	Thickness	$E_x=E_y$	E_z Secant modulus @2MPa	ν_{xy}	ν_{xz}
		µm	MPa	MPa		
Roll	*SGL 22BB*	220	2 550	6	0.05	0
Sheet	*TorayH060*	210	8 250	7	0.05	0
Felt	*Fr-H23C7*	270	1 250	29	0.05	0

IV. Model validation

1. Results and discussion :

To validate the equivalent model, comparisons are made with the results obtained by Kusoglu *et al.* [14]. To ease the comparison, all of the boundary conditions and materials properties were used as mentioned in the reference [14] as follows:

- **out-of-plane conditions:** fixed displacement: a constant displacement of -0.005mm resulting under a 2MPa applied load is fixed in this case.
- **In-plane conditions:** fixed displacement for the membrane and the GDL, following the one of the bipolar plates (6.10^{-5}mm) (***Figure 2a***).
- **Material properties**: the properties of the used BPP and the membrane are the same as mentioned in ***Table 1***. The GDL is considered with an isotropic behavior and with the following properties:
    - $E=10\ 000\ MPa$
    - $\alpha= -0.8\times10^{-6}\ K^{-1}$
    - $\nu= 0.25$

Figure 5 shows the different membrane strains (elastic, plastic, thermal and swelling) for both numerical analyses, during the first hygrothermal cycle. The plastic strain magnitude for both models for the 5 cycles can be observed on Figure 5. Results from both models exhibit equivalent trend for all strains with similar quantitative values (***Table 7***). Thermal and swelling strains are identical since they are defined in the same manner. The appearance of plastic strains occurs at almost identical hygrothermal conditions. As for Kusoglu's simulation [14], reverse yielding can be observed in the equivalent model, i.e. the plastic strain reaching a maximum at the highest hygrothermal loading (95%RH-85°C) and decreasing at the end of the hygrothermal unloading. The plastic strain magnitude values (considering all direction x, y, z) are very similar for both models, with maximum relative differences of 10% during the first cycle, the values getting closer with the following cycles (***Figure 6***).

These results show that even if the equivalent model considers only the rib of the flow field, and not the part of the MEA under the gas channel, very similar results than the one proposed by Kusoglu *et al.* [14] are obtained, thus validating this approach.

The equivalent model is validated and will be used later in this study to analyze the impact of the types of GDL, assembly conditions, and the in-plane boundary conditions. For in-plane conditions, two configurations are considered, the first one with bonded layers and the second one with free displacement at each interface of the layers.

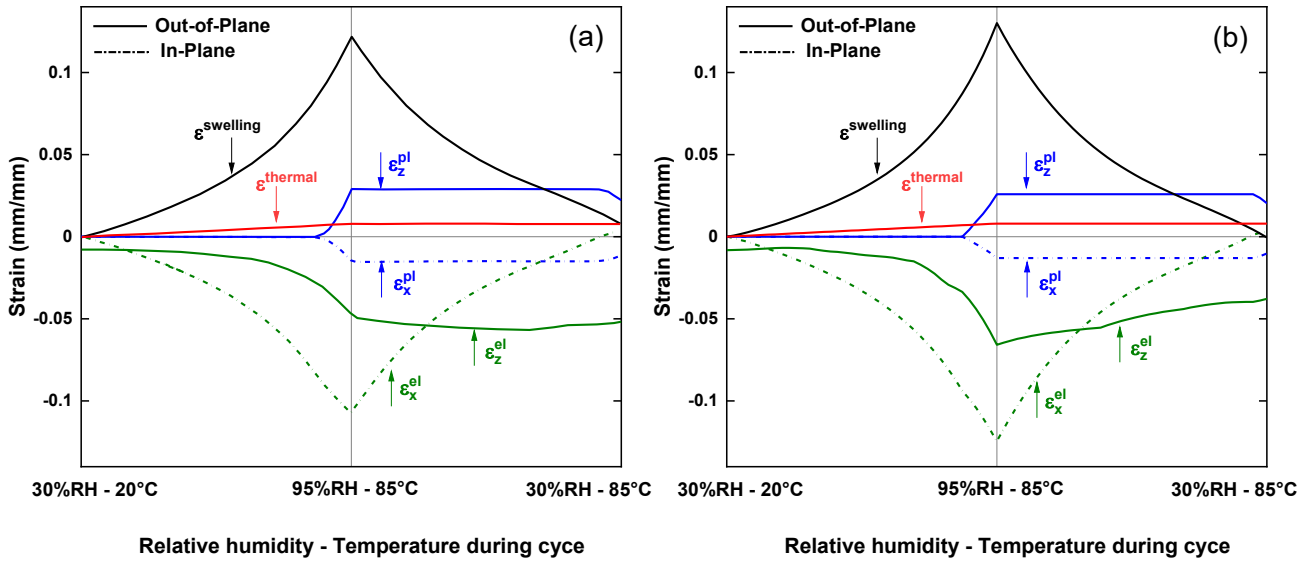

Figure 5: Membrane strains (elastic, plastic, thermal and swelling) during the first hygrothermal cycle (a) obtained by Kusoglu *et al. [14]* and (b) results from the equivalent model.

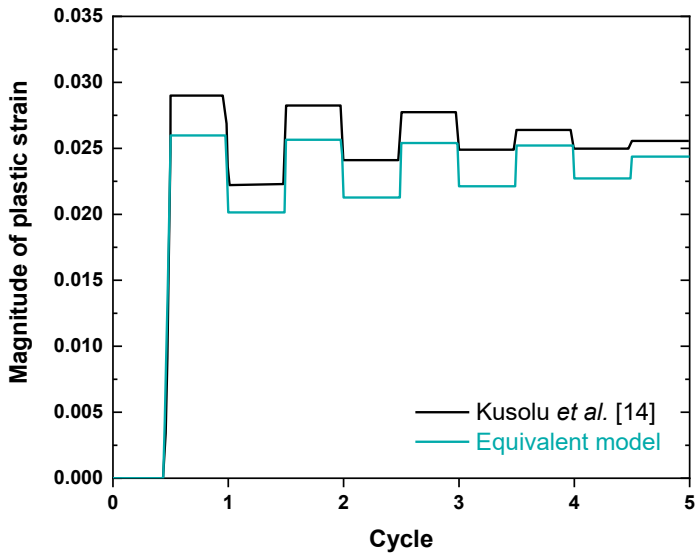

Figure 6: Magnitude of plastic strain of the membrane during the 5 hygrothermal cycles (a) obtained by Kusoglu *et al. [14]* and (b) results from the equivalent model.

***Table 7**: Comparisons of quantitative values of membrane plastic strains for both models.*

	Kusoglu *et al.* [14]	**Equivalent model**	**Relative difference**
Appearance of plastic strains	86%RH-76°C	88%RH-78°C	
Plastic strain magnitude: maximum on all 5 cycles	0.029 mm/mm	0.026 mm/mm	10%
Plastic strain magnitude: at the end of 5 cycles	0.026 mm/mm	0.024 mm/mm	8%

2. Equivalent model

As a first step, the results of an arbitrary configuration are described in this part, including the following parameters:

- GDL = SGL 22BB
- Assembly mode = fixed displacement
- Interfaces = bonded

The plastic strains and stresses obtained with this configuration are depicted in ***Figure 7***. The magnitude of the plastic strain is strictly identical to the plastic strain in z direction, due to the fact that the strains and stresses are defined as equal in x and y direction. The implementation of the anisotropic behavior of the GDL does not modify the trend that were observed in the isotropic model of Kusoglu *et al.* [14], *i.e.* a maximum value of plastic strain obtained during the first hygrothermal loading followed by a reverse yielding at the end of the hygrothermal unloading. The plastic strain is virtually stabilized after 5 hygrothermal cycles. Integrating the real GDL out-of-plane properties bring however a significant change in the plastic strain value, reaching a maximum of 0.1 mm/mm and stabilizing toward a value of 0.06 mm/mm at the end of the 5 cycles, roughly three times the plastic strains values observed in the isotropic case. This is mainly due to the fact that the lowest stiffness of the GDL in the out of plane direction brought by the implementation of the GDL anisotropy allows the membrane to deform more freely in z direction. Consequently, as observed in ***Figure 7b***, σ_z is more constant, between -2 and -3 MPa, despite the assembly mode set as fixed displacement. On the other hand, the membrane cannot deform freely in x (and y) direction, being bonded to the other layers. σ_x varies then significantly between extreme values of -6 MPa at maximum (compressive state), to 2 MPa (tensile state), during the humidity cycles and the induced swelling. At the end of the 5 cycles, when the hygrothermal conditions go back to the initial ones (30%RH-25°C), a tensile stress σ_x of 7 MPa is observed, results from the plastic deformation in compression during the previous cycles. σ_{VM} is then reaching higher values during the hygrothermal cycles, being dependent on the differences of stresses in x, y, z directions, hence the higher plastic strains values as discussed above.

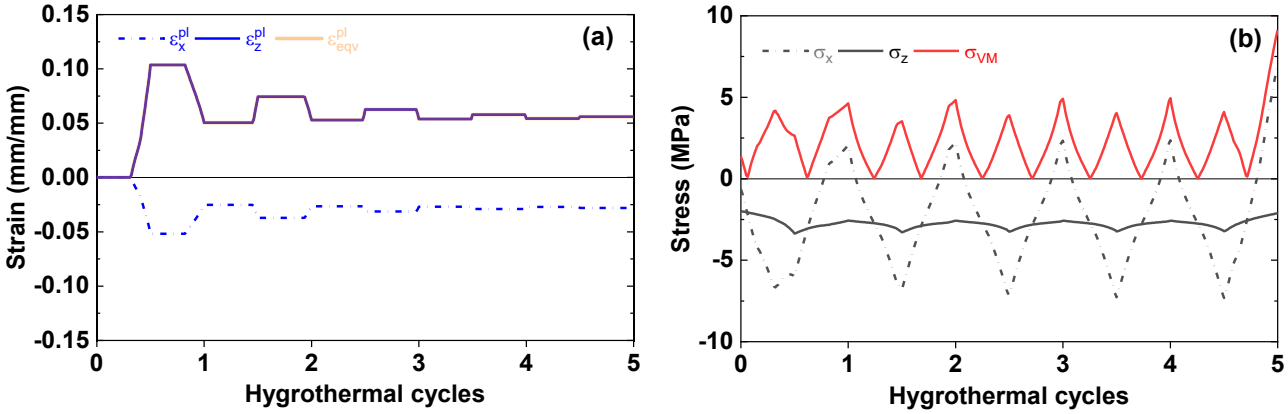

Figure 7: *Results obtained with the equivalent model for the configuration GDL=22BB, assembly mode=fixed displacement, interfaces=bonded. (a) Plastic strains (in x and z directions and equivalent plastic strain) and (b) stresses (in x and z direction and Von Mises).*

V. Influence of the GDL type

The chosen configuration is fixed displacement for assembly mode and in-plane boundary conditions (no sliding is allowed) for three types of GDL (***Table 6***).

Figure 8 presents the magnitude of the plastic strain for three different types of GDLs. A weak decrease is observed by going from a roll to felt type but the variation is not significant. Using a more rigid GDL (sheet) or a spaghetti type (felt) helps barely reduce the plastic strain magnitudes but is not a criterion to be based on choosing the GDL type to amortize plastic deformation. The same tendency has been observed for other boundary conditions (sliding allowed, fixed force for assembly mode) (not shown here).

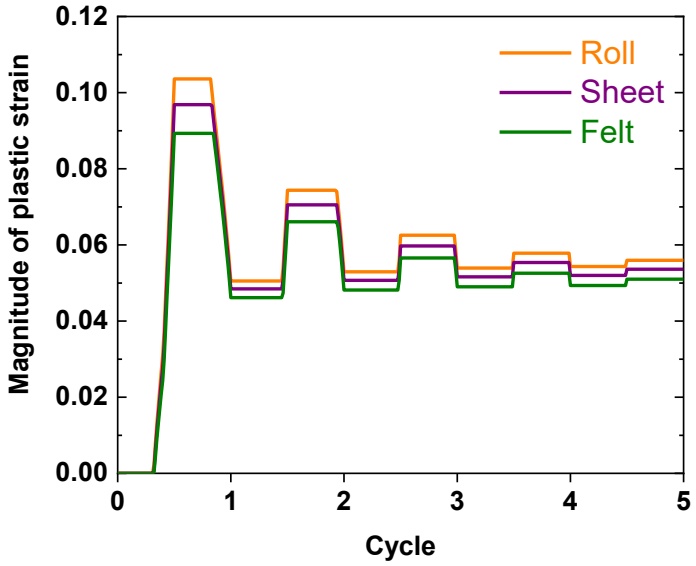

Figure 8*: Plastic strains for the three types of GDL (roll, sheet, felt). The layers of the MEA are considered as bonded (no sliding is allowed, and fixed displacement is considered for the assembly mode.*

VI. Influence of the properties at interfaces

For the following, the chosen GDL reference is SGL22BB. The aim of this section is to study the impact of the properties at interfaces between the membrane and the surrounding layers by changing the boundary conditions. Fixed force and displacement are used for both cases where the sliding in the plane is allowed or not.

Case1: Bonded layers

For the plastic strain variation, as depicted in ***Figure 9***, when no sliding is allowed, the amplitude of the plastic strain is almost the same for both assembly modes. The maximum difference is observed at the first hygrothermal loading and is only equal to 16% and 23% respectively for the plastic strains on x and z. Afterwards the difference fades away due to reverse yielding, and at the end of the hygrothermal cycles the values are basically identical for both cases (fixed displacement and fixed force). The plastic strains variation can be explained by the stresses variation. As seen in ***Figure 10***, the magnitude of σ_z is always smaller compared to σ_x. In addition, repeated fluctuation between tensile and compressive stresses are observed on x, as opposed to an alternating between two compressive stresses on z. The latter case is less likely to cause mechanical fatigue failure of the membrane.

For the fixed force case, the clamping mode implies a constant value of σ_z during the entire hygrothermal cycling (***Figure 10***).

Case2: Free displacement

When the membrane is no longer retained, no reverse yielding is occurred. Higher values of plastic strains are observed in the case of a fixed displacement. The amplitudes of the plastic strain in both directions is 77% higher for the latter. However, the fatigue cycles described by the switching between compressive and tensile values are no longer observed (***Figure 10***).

The stress value on x being equal to zero, the Von Mises stress automatically follows the absolute value of σ_z.

To sum up, the major differences could only be seen when changing the in-plane boundary conditions by preventing or not the sliding.

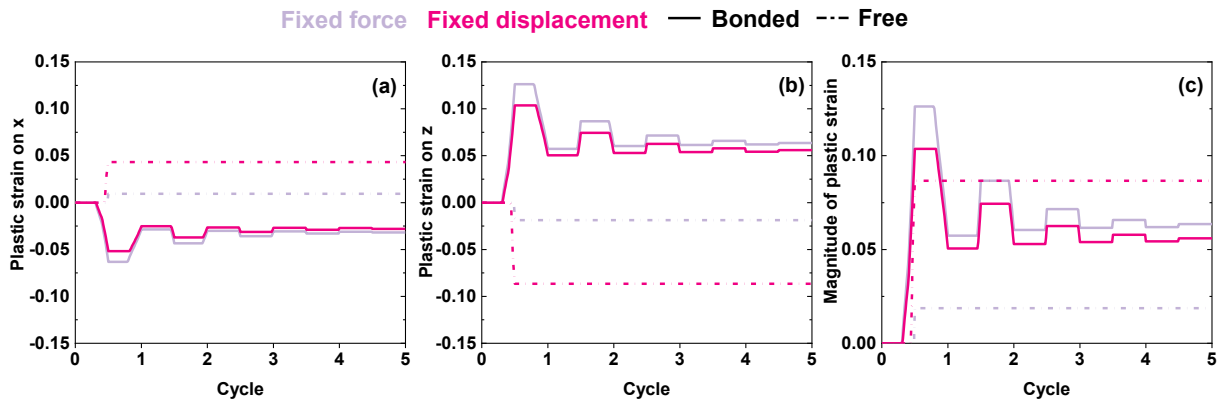

Figure 9: *Plastic strains on (a) x, (b) z and (c) magnitude) obtained for bonded and sliding interfaces, for both assembly modes (fixed displacement and fixed force). GDL reference is 22BB.*

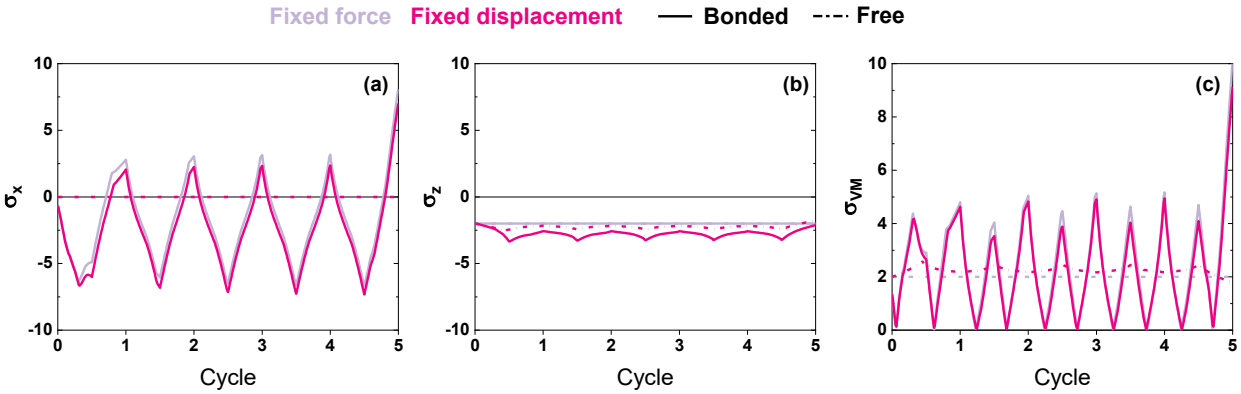

Figure 10: *Mechanical stress on (a) x, (b) z and (c) Von Mises) obtained for bonded and sliding interfaces, for both assembly modes (fixed displacement and fixed force). GDL reference is 22BB.*

VII. Conclusion

Hygrothermal cycles at constant temperature are simulated in this numerical study to investigate the mechanical response of fuel cell proton exchange membranes at various boundary conditions and for different GDL behaviors (isotropic and isotropic transverse) and types (roll, sheet and felt). Both fixed force and fixed displacement cases were used for the clamping mode.

The mechanical model of the membrane assumes linear-elasticity with isotropic-hardening plasticity, and temperature–humidity dependent material properties based on experimental studies and numerical studies [14,48]. Mechanical properties of the different used GDLs are based on our previous experimental work [49].

The results confirm that no significant impact of the GDL type was observed, however, the anisotropic behavior of the GDL has an impact on the mechanical response membrane in the thickness direction (on z), the in-plane behavior (on x) depends on the boundary

conditions. In fact, the isotropic transverse GDL is less rigid on z which allows the swelling of the membrane under the effect of the hydrothermal loading. In contrast, the isotropic GDL is as rigid in the plane as in the thickness direction, therefore, it transmits the applied stress directly to the membrane leading to a similar case of an isostatic compressive state which consequently lead to reduce the plastic strain magnitude. The same applies to the clamping mode, free in-plane displacement causes higher plastic strain compared to the case where the layers are assumed to be bonded. A stress gradient is generated, between the two s directions leading to large stress amplitudes and thus strain values.

To sum up:

- GDL type has no impact on the membrane's mechanical response
- The lowest plastic strain magnitude is obtained under fixed force clamping method and with free displacement in the plane direction. Therefore, by controlling the plastic strain of the membrane, better fatigue resistance could be obtained eventually leading to better performance of the cell during its operating cycles. The durability of the cell could also be improved by delaying the probability of the membrane's failure.

References

[1] Qiu D, Yi P, Peng L, Lai X. Assembly design of proton exchange membrane fuel cell stack with stamped metallic bipolar plates. International Journal of Hydrogen Energy 2015;40:11559–68. https://doi.org/10.1016/j.ijhydene.2015.03.064.

[2] Giacoppo G, Hovland S, Barbera O. 2 kW Modular PEM fuel cell stack for space applications: Development and test for operation under relevant conditions. Applied Energy 2019;242:1683–96. https://doi.org/10.1016/j.apenergy.2019.03.188.

[3] Wu Z, Zhou Y, Lin G, Wang S, Hu SJ. An improved model for predicting electrical contact resistance between bipolar plate and gas diffusion layer in proton exchange membrane fuel cells. Journal of Power Sources 2008;182:265–9. https://doi.org/10.1016/j.jpowsour.2008.03.044.

[4] Ge J, Higier A, Liu H. Effect of gas diffusion layer compression on PEM fuel cell performance. Journal of Power Sources 2006;159:922–7. https://doi.org/10.1016/j.jpowsour.2005.11.069.

[5] Lin J-H, Chen W-H, Su Y-J, Ko T-H. Effect of gas diffusion layer compression on the performance in a proton exchange membrane fuel cell. Fuel 2008;87:2420–4. https://doi.org/10.1016/j.fuel.2008.03.001.

[6] Radhakrishnan V, Haridoss P. Effect of cyclic compression on structure and properties of a Gas Diffusion Layer used in PEM fuel cells. International Journal of Hydrogen Energy 2010;35:11107–18. https://doi.org/10.1016/j.ijhydene.2010.07.009.

[7] Lee S-J, Hsu C-D, Huang C-H. Analyses of the fuel cell stack assembly pressure. Journal of Power Sources 2005;145:353–61. https://doi.org/10.1016/j.jpowsour.2005.02.057.

[8] Lai X, Liu D, Peng L, Ni J. A mechanical–electrical finite element method model for predicting contact resistance between bipolar plate and gas diffusion layer in PEM fuel cells. Journal of Power Sources 2008;182:153–9. https://doi.org/10.1016/j.jpowsour.2008.03.069.

[9] Huang X, Solasi R, Zou Y, Feshler M, Reifsnider K, Condit D, et al. Mechanical endurance of polymer electrolyte membrane and PEM fuel cell durability. J Polym Sci B Polym Phys 2006;44:2346–57. https://doi.org/10.1002/polb.20863.

[10] Su ZY, Liu CT, Chang HP, Li CH, Huang KJ, Sui PC. A numerical investigation of the effects of compression force on PEM fuel cell performance. Journal of Power Sources 2008;183:182–92. https://doi.org/10.1016/j.jpowsour.2008.04.060.

[11] Carral C, Charvin N, Trouvé H, Mélé P. An experimental analysis of PEMFC stack assembly using strain gage sensors. International Journal of Hydrogen Energy 2014;39:4493–501. https://doi.org/10.1016/j.ijhydene.2014.01.033.

[12] Tang Y, Santare MH, Karlsson AM, Cleghorn S, Johnson WB. Stresses in proton exchange membranes due to hygro-thermal loading 2006. https://doi.org/10.1115/1.2173666.

[13] Kusoglu A, Karlsson AM, Santare MH, Cleghorn S, Johnson WB. Mechanical response of fuel cell membranes subjected to a hygro-thermal cycle. Journal of Power Sources 2006;161:987–96. https://doi.org/10.1016/j.jpowsour.2006.05.020.
[14] Kusoglu A, Karlsson AM, Santare MH, Cleghorn S, Johnson WB. Mechanical behavior of fuel cell membranes under humidity cycles and effect of swelling anisotropy on the fatigue stresses. Journal of Power Sources 2007;170:345–58. https://doi.org/10.1016/j.jpowsour.2007.03.063.
[15] Solasi R, Zou Y, Huang X, Reifsnider K, Condit D. On mechanical behavior and in-plane modeling of constrained PEM fuel cell membranes subjected to hydration and temperature cycles. Journal of Power Sources 2007;167:366–77. https://doi.org/10.1016/j.jpowsour.2007.02.025.
[16] Silberstein MN, Boyce MC. Constitutive modeling of the rate, temperature, and hydration dependent deformation response of Nafion to monotonic and cyclic loading. Journal of Power Sources 2010;195:5692–706. https://doi.org/10.1016/j.jpowsour.2010.03.047.
[17] Silberstein MN, Boyce MC. Hygro-thermal mechanical behavior of Nafion during constrained swelling. Journal of Power Sources 2011;196:3452–60. https://doi.org/10.1016/j.jpowsour.2010.11.116.
[18] Feng C, Li Y, Qu K, Zhang Z, He P. Mechanical behavior of a hydrated perfluorosulfonic acid membrane at meso and nano scales. RSC Adv 2019;9:9594–603. https://doi.org/10.1039/C9RA00745H.
[19] Bograchev D, Gueguen M, Grandidier J-C, Martemianov S. Stress and plastic deformation of MEA in fuel cells. Journal of Power Sources 2008;180:393–401. https://doi.org/10.1016/j.jpowsour.2008.02.048.
[20] de la Cruz J, Cano U, Romero T. Simulation and in situ measurement of stress distribution in a polymer electrolyte membrane fuel cell stack. Journal of Power Sources 2016;329:273–80. https://doi.org/10.1016/j.jpowsour.2016.08.073.
[21] Zhou P, Wu CW, Ma GJ. Contact resistance prediction and structure optimization of bipolar plates. Journal of Power Sources 2006;159:1115–22. https://doi.org/10.1016/j.jpowsour.2005.12.080.
[22] Kandlikar SG, Lu Z, Lin TY, Cooke D, Daino M. Uneven gas diffusion layer intrusion in gas channel arrays of proton exchange membrane fuel cell and its effects on flow distribution. Journal of Power Sources 2009;194:328–37. https://doi.org/10.1016/j.jpowsour.2009.05.019.
[23] Liu D, Peng L, Lai X. Effect of dimensional error of metallic bipolar plate on the GDL pressure distribution in the PEM fuel cell. International Journal of Hydrogen Energy 2009;34:990–7. https://doi.org/10.1016/j.ijhydene.2008.10.081.
[24] Yi P, Peng L, Lai X, Ni J. A Numerical Model for Predicting Gas Diffusion Layer Failure in Proton Exchange Membrane Fuel Cells. Journal of Fuel Cell Science and Technology 2011;8:011011. https://doi.org/10.1115/1.4002312.
[25] García-Salaberri PA, Vera M, Zaera R. Nonlinear orthotropic model of the inhomogeneous assembly compression of PEM fuel cell gas diffusion layers.

International Journal of Hydrogen Energy 2011;36:11856–70. https://doi.org/10.1016/j.ijhydene.2011.05.152.
[26] Holzer L, Pecho O, Schumacher J, Marmet Ph, Stenzel O, Büchi FN, et al. Microstructure-property relationships in a gas diffusion layer (GDL) for Polymer Electrolyte Fuel Cells, Part I: effect of compression and anisotropy of dry GDL. Electrochimica Acta 2017;227:419–34. https://doi.org/10.1016/j.electacta.2017.01.030.
[27] Firat E, Beckhaus P, Heinzel A. Finite Element Approach for the Analysis of the Fuel Cell Internal Stress Distribution n.d.:7.
[28] Kleemann J, Finsterwalder F, Tillmetz W. Characterisation of mechanical behaviour and coupled electrical properties of polymer electrolyte membrane fuel cell gas diffusion layers. Journal of Power Sources 2009;190:92–102. https://doi.org/10.1016/j.jpowsour.2008.09.026.
[29] Nitta I, Karvonen S, Himanen O, Mikkola M. Modelling the Effect of Inhomogeneous Compression of GDL on Local Transport Phenomena in a PEM Fuel Cell. Fuel Cells 2008;8:410–21. https://doi.org/10.1002/fuce.200700058.
[30] Zhou Y, Lin G, Shih AJ, Hu SJ. Assembly pressure and membrane swelling in PEM fuel cells. Journal of Power Sources 2009;192:544–51. https://doi.org/10.1016/j.jpowsour.2009.01.085.
[31] Zhou Y, Lin G, Shih AJ, Hu SJ. Multiphysics Modeling of Assembly Pressure Effects on Proton Exchange Membrane Fuel Cell Performance. Journal of Fuel Cell Science and Technology 2009;6:041005. https://doi.org/10.1115/1.3081426.
[32] Norouzifard V, Bahrami M. Deformation of PEM fuel cell gas diffusion layers under compressive loading: An analytical approach. Journal of Power Sources 2014;264:92–9.
[33] Gigos PA, Faydi Y, Meyer Y. Mechanical characterization and analytical modeling of gas diffusion layers under cyclic compression. International Journal of Hydrogen Energy 2015;40:5958–65.
[34] El Oualid S, Lachat R, Candusso D, Meyer Y. Characterization process to measure the electrical contact resistance of Gas Diffusion Layers under mechanical static compressive loads. International Journal of Hydrogen Energy 2017;42:23920–31.
[35] Carral C, Mélé P. A constitutive law to predict the compression of gas diffusion layers. International Journal of Hydrogen Energy 2018;43:19721–9. https://doi.org/10.1016/j.ijhydene.2018.08.210.
[36] Meng L, Zhou P, Yan Y, Guo D. Compression properties of gas diffusion layers and its constitutive model under cyclic loading. International Journal of Hydrogen Energy 2021;46:15965–75. https://doi.org/10.1016/j.ijhydene.2021.02.083.
[37] Lai Y-H, Rapaport PA, Ji C, Kumar V. Channel intrusion of gas diffusion media and the effect on fuel cell performance. Journal of Power Sources 2008;184:120–8. https://doi.org/10.1016/j.jpowsour.2007.12.065.
[38] Serincan MF, Pasaogullari U. Effect of gas diffusion layer anisotropy on mechanical stresses in a polymer electrolyte membrane. Journal of Power Sources 2011;196:1314–20. https://doi.org/10.1016/j.jpowsour.2010.06.026.

[39] Lee T, Yang C. A parametric study on the deformation of gas diffusion layer in PEM fuel cell. J Mech Sci Technol 2020;34:259–68. https://doi.org/10.1007/s12206-019-1227-8.
[40] Leng Y, Yao H, Yang D, Li B, Ming P, Zhang C. The influences of gas diffusion layer material models and parameters on mechanical analysis of proton exchange membrane fuel cell. Fuel Cells 2021;21:373–89. https://doi.org/10.1002/fuce.202100068.
[41] Al-Baghdadi MAS. A CFD study of hygro–thermal stresses distribution in PEM fuel cell during regular cell operation. Renewable Energy 2009;34:674–82.
[42] Bajpai H, Khandelwal M, Kumbur EC, Mench MM. A computational model for assessing impact of interfacial morphology on polymer electrolyte fuel cell performance. Journal of Power Sources 2010;195:4196–205. https://doi.org/10.1016/j.jpowsour.2009.12.121.
[43] Zenyuk IV. Deterministic contact mechanics model applied to electrode interfaces in polymer electrolyte fuel cells and interfacial water accumulation. Journal of Power Sources 2013:9.
[44] Ous T, Arcoumanis C. Effect of compressive force on the performance of a proton exchange membrane fuel cell. Proceedings of the Institution of Mechanical Engineers, Part C: Journal of Mechanical Engineering Science 2007;221:1067–74. https://doi.org/10.1243/09544062JMES654.
[45] Uzundurukan A, Bilgili M, Devrim Y. Examination of compression effects on PEMFC performance by numerical and experimental analyses. International Journal of Hydrogen Energy 2020;45:35085–96. https://doi.org/10.1016/j.ijhydene.2020.04.275.
[46] Turner JR. Contact on a transversely isotropic half-space, or between two transversely isotropic bodies. International Journal of Solids and Structures 1980;16:409–19. https://doi.org/10.1016/0020-7683(80)90039-6.
[47] Oliver X, de Saracibar CA. Continuum Mechanics for Engineers n.d.:550.
[48] Tang Y, Karlsson AM, Santare MH, Gilbert M, Cleghorn S, Johnson WB. An experimental investigation of humidity and temperature effects on the mechanical properties of perfluorosulfonic acid membrane. Materials Science and Engineering: A 2006;425:297–304. https://doi.org/10.1016/j.msea.2006.03.055.
[49] Ouerghemmi M, Carral C, Mele P. Experimental study of gas diffusion layers nonlinear orthotropic behavior. E3S Web of Conferences, vol. 334, EDP Sciences; 2022, p. 04020.

Conclusions and prospects

The mechanical properties of the different components of the PEMFC have been studied using a dual mechanical approach via an experimental and numerical analyses. Specific experimental setups, as well as a 1D numerical model, have been developed for this purpose.

First the mechanical properties of GDL was investigated through a series of in-plane and out-of-plane mechanical tests, in both, machine and transverse directions. The goal is to evaluate the anisotropy of its properties. The tests were conducted on different types of GDLs in sheet and roll forms and with different hydrophobic treatment. It was found that the mechanical behavior of GDL is rather isotropic transverse. The 2D anisotropy is not significant and the properties in the same plane are very similar. The magnitude of the in-plane properties is higher to the ones in the thickness direction as depicted in ***Figure 1***.

No significant impact of the hydrophobic treatment was observed, however the type of the GDL was found to be influential. GDL in sheet form was found stiffer than the ones in roll form.

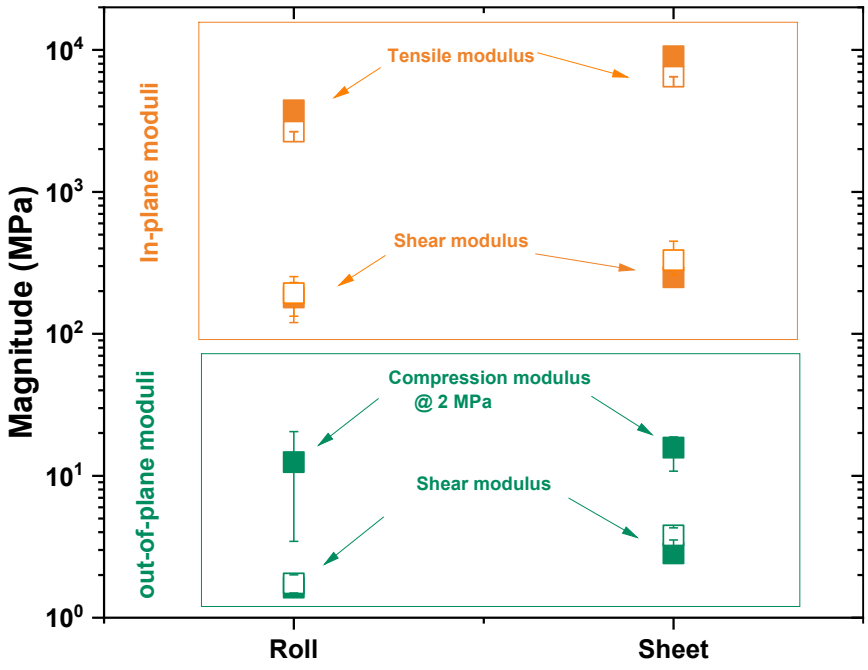

Figure 1*: Mechanical properties of GDL*

In the second part of this study, the properties at interfaces between the MEA layers were investigated. An experimental set up was developed (***Figure 2***) to measure static and kinetic friction coefficients. Measurements were conducted between the MPL, the CL and the membrane. Different types of material assemblies were tested with different assembly

process parameters. It was found that adding the MPL and the CL leads to higher adhesion between the layers, illustrated with higher friction coefficient between these two layers.

It was also shown that contact is further enhanced between the layers of a MEA subjected to assembly process. With the combined action of heat and pressure applied during assembly process, the roughness of the surfaces is reduced, hence, a decrease in the friction coefficient was observed (***Figure 3***).

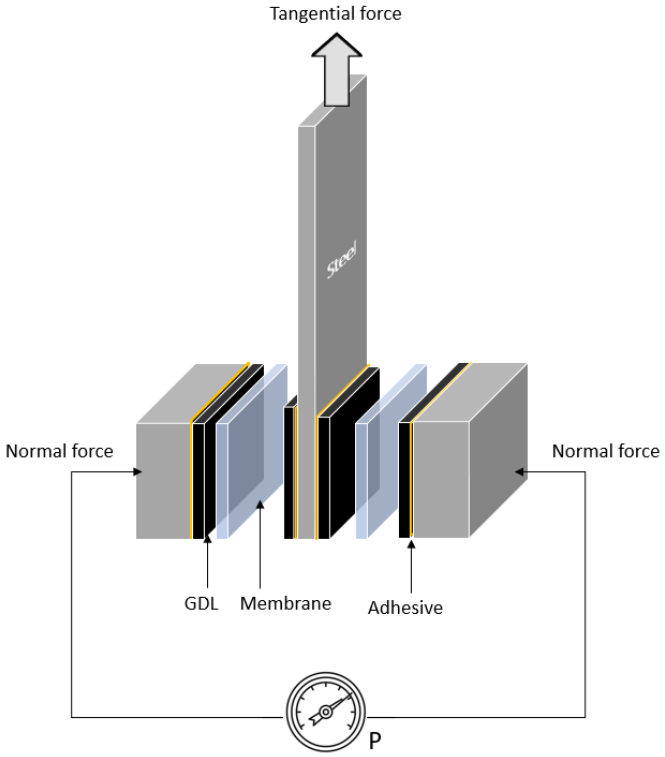

Figure 2*: Experimental set up of the friction test*

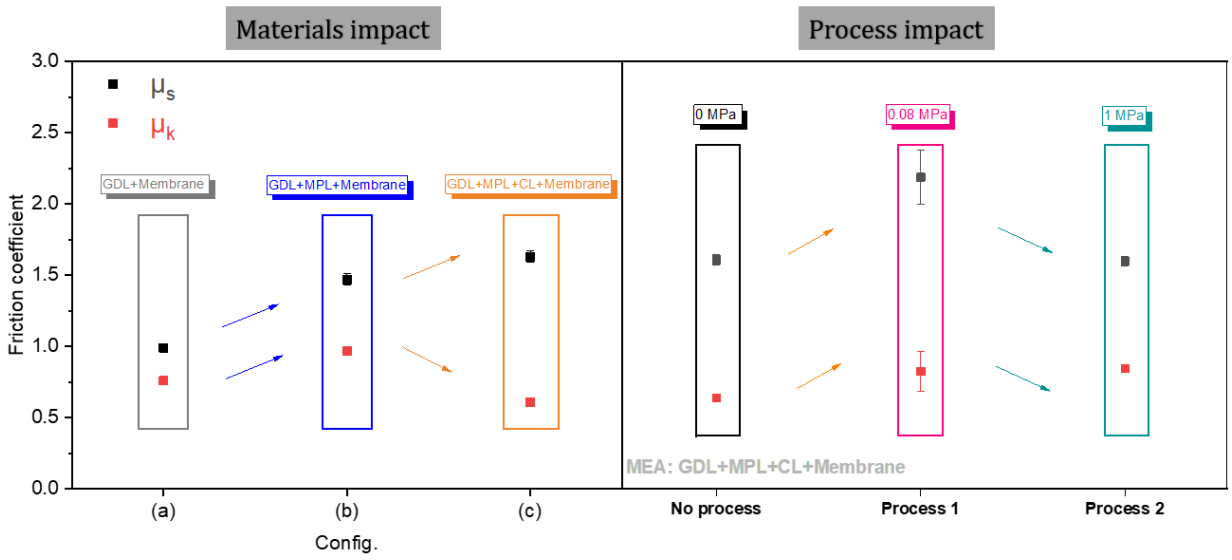

Figure 3: *Impact of materials properties and assembly processes on friction coefficients*

Finally, this study is completed with a numerical analysis based on the experimental data previously determined. A numerical model was developed on MATLAB to simulate the mechanical state of the MEA under the compression of the gas channel rib. In particular, the mechanical response of the membrane under different assembly modes and hygrothermal cycling was investigated. The 1D model (***Figure 4***) allowed the integration of the anisotropic behavior of GDL, the membrane elastoplastic behavior with its hygrothermal dependency, and the interfaces properties of the MEA. First the GDL type was studied, no significant impact was observed. Afterwards, the nature of interfaces was analyzed by considering or not the sliding in the plane between the piled layers. The clamping method was then studied following fixed force or fixed displacement.

The results confirmed that the lowest plastic strain was obtained under fixed force and free in-plane displacement. In fact, this result is important to guarantee better performance and durability of the cell since controlling the plastic strain means increasing the fatigue resistance of the membrane.

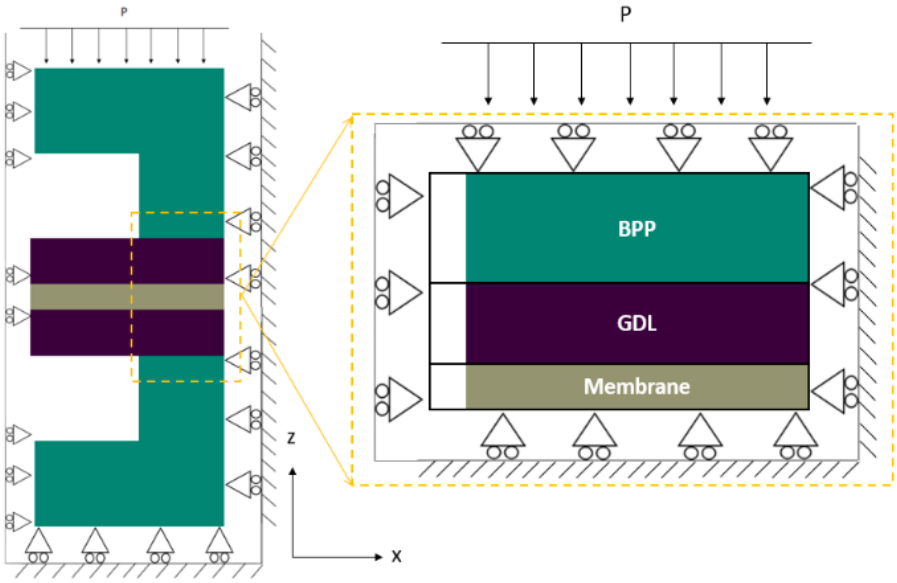

Figure 4: *The geometry of the unit cell used for the developed model*

This work finally allowed to understand the mechanical state of the MEA with different material properties components and under several operating and assembly conditions. Through the various studied configurations, it turned out that it is crucial to control the assembly mode and the properties at interfaces to guarantee good performance and durability of the cell. Materials properties when it comes to GDL did not have a significant impact on the mechanical response of the membrane.

In perspective of this work, it would be relevant to carry out the experimental study under operating conditions to simulate the real state of an operating fuel cell. First, the mechanical properties of GDL could be determined under temperature and humidity similar to those of the operating conditions of the fuel cell (85°C – 95 RH%).

Second, it should be noted that the frictional properties are sensitive to any type of impurity or intruding material that might be present at interfaces, for that purpose, the friction measurements could also be carried out in a hygrothermal chamber, to follow the properties evolution. A preliminary part of this experimental test has already been started to evaluate the impact of the temperature separately. It was found that the frictional properties are almost stable in the range of the operating temperature used (85°C). This is consistent with the literature, where the friction coefficient could probably change at much higher ranges of temperature. However, humidity would probably have a more significant impact since layers of water might be created between the layers and absorbed on the surface of materials. A similar case of lubrification process could occur, reducing, thus, friction between the moving parts.

Finally, all of the experimental work might be re-implemented in the developed model to evaluate the strain and stress levels under real operating conditions. The model could also be upgraded to evaluate the shear phenomena induced by the geometry of the BPP, and integrate the frictional properties experimentally determined.